DRAFT COPY

Printed August 25, 2003

MOVING OBJECTS IMAGING AND TRAJECTORY ESTIMATION USING A SINGLE SYNTHETIC APERTURE RADAR SENSOR

By

Paulo A. C. Marques

SUBMITTED IN PARTIAL FULFILLMENT OF THE
REQUIREMENTS FOR THE DEGREE OF
DOCTOR OF PHILOSOPHY
AT
INSTITUTO SUPERIOR TÉCNICO
UNIVERSIDADE TÉCNICA DE LISBOA
LISBOA, PORTUGAL
MAY 2003

INSTITUTO SUPERIOR TÉCNICO
UNIVERSIDADE TÉCNICA DE LISBOA
DEPARTMENT OF
ENGENHARIA ELECTROTÉCNICA

The undersigned hereby certify that they have read and recommend to the Faculty of Graduate Studies for acceptance a thesis entitled "**Moving Objects Imaging and Trajectory Estimation Using a Single Synthetic Aperture Radar Sensor**" by **Paulo A. C. Marques** in partial fulfillment of the requirements for the degree of **Doctor of Philosophy**.

Dated: May 2003

External Examiner: _____
Xiang Xia

Research Supervisor: _____
José M. B. Dias

Examing Committee: _____
first reader name

_____
second reader name

INSTITUTO SUPERIOR TÉCNICO

UNIVERSIDADE TÉCNICA DE LISBOA

Date: **May 2003**

Author: **Paulo A. C. Marques**

Title: **Moving Objects Imaging and Trajectory Estimation Using a Single Synthetic Aperture Radar Sensor**

Department: **Engenharia Electrotécnica**

Degree: **Ph.D.** Convocation: **July** Year: **2003**

Signature of Author

Table of Contents

List of Tables

List of Figures

Acronyms

Acronym	Definition
ATR	Automatic target recognition
CRLB	Cramer-rao lower bound
DPCA	Displaced phase center array
ISAR	Inverse synthetic aperture radar
LFM	Linear Frequency Modulation
MF-VSAR	Multi-frequency velocity synthetic aperture radar
MSTAR	Moving and stationary target acquisition and recognition
MTI	Moving target indication
PRF	Pulse repetition frequency
PRI	Pulse repetition interval
SAR	Synthetic Aperture Radar
SCNR	Signal-to-clutter-plus-noise ratio
SCR	Signal-to-clutter ratio
STAP	Space-time adaptive processing
VSAR	Velocity synthetic aperture radar

Notation

Symbol	Definition
$a(\phi, \theta, \omega)$	Two-way antenna radiation pattern at frequency $\omega + \omega_0$
$A(\omega, k_u)$	Two-way antenna radiation pattern in two-dimensional frequency domain
B	Transmitted pulse bandwidth
B_u	Antenna bandwidth in the slow-time frequency domain
c	Speed of light
$C_w(k_{u_1}, k_{u_1})$	Covariance of $w(k_u, t)$ at time t
D_y	Antenna cross-range aperture length
E_{R_p}	Energy of $R_p(t)$
E_p	Energy of $p(t)$
f	Point target refectivity
$\mathcal{F}$	Fourier transform operator
$\mathcal{F}^{-1}$	Inverse Fourier transform operator
$g(k_x, k_y)$	Fourier transform of the electric field in the antenna aperture
$h(t, u)$	Two-dimensional point spread function
k	Wavenumber: $k = (\omega + \omega_0/c$
k_c	Wavenumber at carrier frequency $k_c = \omega_c/c$
k_{DC}	Doppler centroid
k_s	Nyquist cross-range frequency
k_u	Spatial frequency or wavenumber domain for synthetic aperture u;

	slow-time frequency domain
k_x	Slant-range spatial frequency
k_y	Cross-range spatial frequency
l	Likelihood ratio
L	Target area cross-range length
$\mathcal{N}(\boldsymbol{\mu}, \boldsymbol{C})$	Normal probability density function of mean vector $\boldsymbol{\mu}$ and covariance matrix $\mathbf{C}$
$p(t)$	Transmitted radar signal
$p(\mathbf{s}\|f, \boldsymbol{\theta})$	Probability density function of vector $\mathbf{s}$ parameterized with f and $\boldsymbol{\theta}$
$P(\omega)$	Fourier transform of transmitted radar signal
P_D	Probability of detection
P_{F_A}	Probability of false alarm
r	Radial distance
$R_p(t)$	Deterministic autocorrelation of $p(t)$
$s(u,t)$	Spatial signature of a scene
$s(u,\omega)$	Fourier transform of $s(u,t)$ w.r.t. t
$S(k_u,\omega)$	Fourier transform of $s(u,t)$ w.r.t. u and t
$\overline{S}(\Omega,\omega)$	Discrete Fourier transform of $s(n\Delta u,\omega)$
$s_c(k_u,t)$	Compressed signature in the (k_u,t) domain
t	Fast-time domain
T_p	Radar pulse duration
u	Synthetic aperture domain
v_r	Speed of radar-carrying vehicle
v_x	Moving target slant-range velocity
v_y	Moving target cross-range velocity
x	Slant-range domain
x_0	Initial $(u=0)$ slant-range coordinate of a moving target
X	Motion transformed slant-range coordinate
X_c	Midrange or center point of target area

y	Cross-range domain
y_0	Initial ($u = 0$) cross-range coordinate of a moving target
Y	Motion transformed cross-range coordinate
Y_c	Mean cross-range of target area
α	Relative speed of target in SAR scene with respect to radar
$\Delta\omega$	Sample spacing of Fourier transform of echoed signal
η	Detection threshold
λ	Wavelength: $\lambda = 2\pi c/(\omega + \omega_0)$
μ	Slant-range relative velocity of a moving target with respect to the radar
ν	Quantity related to the cross-range relative velocity of a moving target with respect to the radar
θ	Aspect angle of a target

Introduction

In the recent past, several synthetic aperture radar (SAR) missions have been successfully launched, for civil and for military applications. Examples of such missions are, in the spaceborne case, ERS-1 (Europe, ESA, 1991), JERS-1 (Japan, NASDA, 1992), ERS-2 (Europe, ESA, 1995), RADARSAT-I (Canada, CSA, 1995), and ENVISAT-I (Europe, ESA, 2002) [44]. Scheduled for launch in 2004 is RADARSAT-2, the next Canadian commercial Earth observation SAR satellite [40]. Several airborne SAR systems have also been flown with success, such as the CARABAS-II (Sweden, SDRA, 2001) [42], AER-II (Germany, DLR, 1996) or the PAMIR (Germany, DLR, 2002) [1]. The SAR community is presently researching aspects of imaging and identification of moving targets, for surveillance purposes. In many applications we want to monitor the position and velocity of certain objects. The purpose may be, for example, to find traffic jams [18] or to detect ships in the sea [31]. Other civil applications include oil pollution monitoring and surface currents measurement [30]. Military applications are also concerned with detecting and recognizing moving targets [43]. The purpose may be to intercept objects that may pose threats to facilities or resources. In other situations the purpose may be to keep the moving objects safely apart from each other as they navigate. These applications require accurate detection, high resolution imaging, and precise kinematics estimation.

This thesis addresses the design of processing schemes aiming at fulfillment these requisites. It is organized as follows.

Chapter 1 establishes notation and terminology. It introduces the stripmap SAR geometry and presents an imaging scheme belonging to a class of algorithms often referred to as *wavenumber domain* or $\omega - k$ processors, (or as *wavefront reconstruction algorithm* in the Soumekh's terminology [55]) to produce focused images using the recorded echoes from an illuminated target area. Other popular SAR imaging algorithms are also described. The difficulty in processing moving targets is then addressed and the ill-posed nature of the problem (termed *blind angle ambiguity* is brought to focus. The next section makes a survey of the state of the art in moving target detection, trajectory estimation, and imaging. The described methodologies are classified into two classes: The single SAR based sensor, and the array SAR based sensor. Advantages and disadvantages of each one are referred.

Chapter 2 deals with the blind angle ambiguity problem. It is shown that this ambiguity can be solved by including information about the antenna radiation pattern. The characteristics that the antenna radiation pattern should exhibit to enhance the velocity estimation accuracy are derived. At the end of the chapter, the theoretically derived characteristics are confirmed experimentally.

Chapter 3 presents a novel procedure to detect and estimate the complete velocity vector and coordinates of moving targets using data from a single SAR sensor. The structure of the amplitude and the phase modulations of the returned echo from a moving target is exploited. A generalized likelihood ratio test is derived to detect moving targets and to estimate their trajectory parameters. The methodology uses a matched filtering operation, depending on the moving targets parameters, that

simultaneously copes with range migration and compresses two-dimensional signatures into one-dimensional ones without degrading the range resolution. Encouraging evaluation results are provided at the end of the chapter.

Chapter 4 develops a new technique to extract all the moving target parameters using data from a single SAR sensor. The methodology works in the spatial domain and, instead of trying to straighten the moving target signature, as it is done in the previous chapter, it extracts the data along the signature curvature that is dependent of the moving target trajectory parameters. This methodology is more efficient, from the computational point of view, than that presented in Chapter 3. It gives, however, less accurate velocity estimates.

Chapter 5 is devoted to estimation of Doppler-shifts induced by moving targets with range velocities exceeding the Nyquist limit imposed by the mission parameters. The methodology takes advantage of the linear dependence of the Doppler-shift on the range velocity at each fast-time frequency. It is shown that, in the two-dimensional frequency domain, a moving target echo exhibits a skew not subject to the mission pulse repetition frequency limitations. A very efficient and simple scheme is then presented and tested. The experimental results shown at the end of the chapter illustrate the usefulness of the technique.

Chapter 6 summarizes the main contributions introduced in this thesis and suggests future research directions.

Chapter 1

Background

1.1 Introduction

This chapter establishes notation and terminology. It introduces the stripmap SAR geometry and presents some of the most popular imaging algorithms. Namely, it establishes the framework for the *wavefront reconstruction* algorithm. This algorithm belongs to a class of algorithms often referred to as *wavenumber domain* or $\omega - k$ type algorithms which correspond to the matched filtering approach to SAR imaging. Then it focus attention on the problem of moving targets imaging and presents modifications to the wavefront reconstruction algorithm in order to get focused images of moving objects. The *blind angle ambiguity* is also addressed. This ambiguity refers to the fact that the value of the Doppler-shift alone is not sufficient to evaluate the azimuth position of the target with respect to the fixed ground. Finally, other state of the art algorithms to moving target detection, imaging, and trajectory parameters estimation are summarized. These algorithms are separated into two classes: single sensor based and array sensor based. Advantages and disadvantages of each class are pointed out.

1.2 Stripmap SAR imaging

Ground surveillance radar is a very useful tool for remote sensing. Airborne and spaceborne radar sensors are able to cover large areas of the ground quickly in all weather, day and night, to produce high quality radar maps [53]. Synthetic aperture radar (SAR) was introduced in the 1950s as a mean to obtain such high quality radar images.

A popular SAR configuration is the so-called *stripmap* SAR geometry which is illustrated by Fig. 1.1. This geometry intends to provide data that, if correctly processed, corresponds to a high resolution radar map of a terrain within a fixed strip in the range domain. The radar travels at constant velocity in the azimuth direction and transmits wide-band microwave pulses at regular intervals. The corresponding echoes are recorded. Many pulses are transmitted during the so called integration time, i.e. the time the platform takes to travel the footprint cross-range length.

High resolution in range is obtained using the traditional pulse compression technique and is independent of the antenna size [50, ch. 7]. Typical look angle values ranges from 20^0 to 60^0. Small look angles lead to degradation of the ground range resolution, while large look angles produces strong shadow effects. High resolution in the azimuth direction is obtained via synthesizing a long array by taking advantage of the platform movement.

The classical image reconstruction for stripmap SAR is based on the Fresnel approximation [15]. However, this approximation is very poor on many large synthetic aperture scenarios, where the non-quadratic phase terms are not negligible.

Our approach in this chapter in the formulation of stripmap SAR processing and

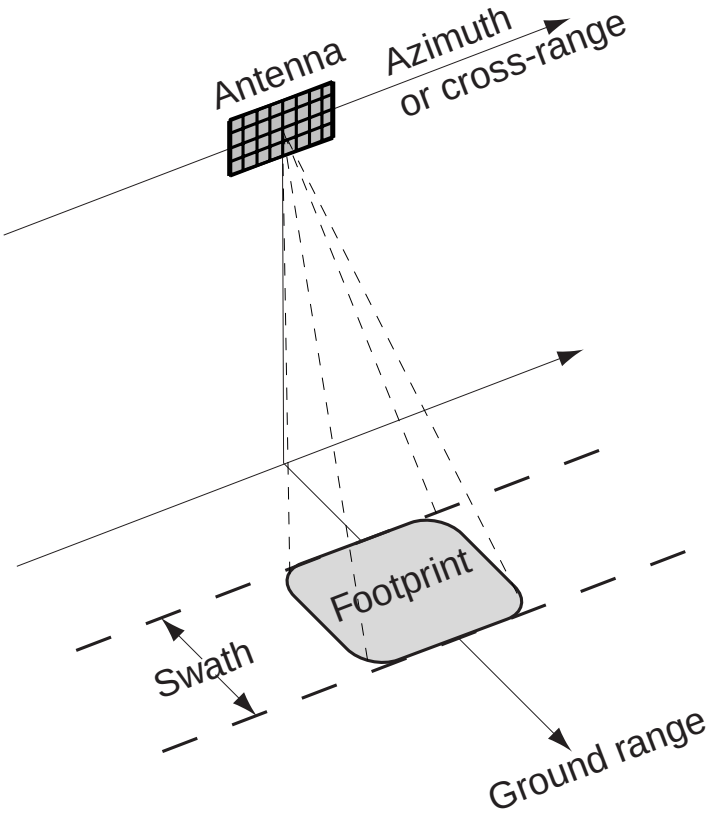

Figure 1.1: Stripmap SAR geometry.

imaging is based on the SAR wavefront reconstruction theory. The wavefront reconstruction algorithm aims at computing the output of matched filter for the problem at hand. For the sake of self-containdness, it is summarized in the next subsection. For a comprehensive treatment, see [55]. In the next subsection the wavefront reconstruction algorithm is summarized for the sake of self containment of this text.

1.2.1 Wavefront Reconstruction Algorithm

Figure 1.3 shows a stripmap synthetic aperture radar scenario in the plane formed by the cross-range axis and the slant-range axis. Let us consider that the radar moves with velocity V along a line that is known as the synthetic aperture domain or the cross-range domain[1]. For a fixed position of the platform, $y = Vt \equiv u$, the radar transmits a wide-band pulse $p(t)$, where t is the *fast-time* domain, and the echoed signal from the illuminated area is recorded.

Let us consider a target region composed of N static point-like targets with complex reflectivity f_n, where $n = 0, ..., N-1$, and coordinates (x_n, y_n) as illustrated in Fig. 1.3. The *target function* corresponding to this scenario is described by

$$f(x, y) \equiv \sum_{n=0}^{N-1} f_n \delta(x - x_n, y - y_n). \tag{1.2.1}$$

The corresponding 2-D Fourier transform is

$$F(k_x, k_y) = \sum_{n=0}^{N-1} f_n e^{-jk_x x_n} e^{-jk_y y_n}, \tag{1.2.2}$$

where k_x and k_y denote the spatial frequency with respect to coordinate x and y respectively.

[1]The cross-range domain is also designated as the *slow-time* domain, owning to the fact that the platform velocity is much smaller than the propagation speed of the electro-magnetic pulses

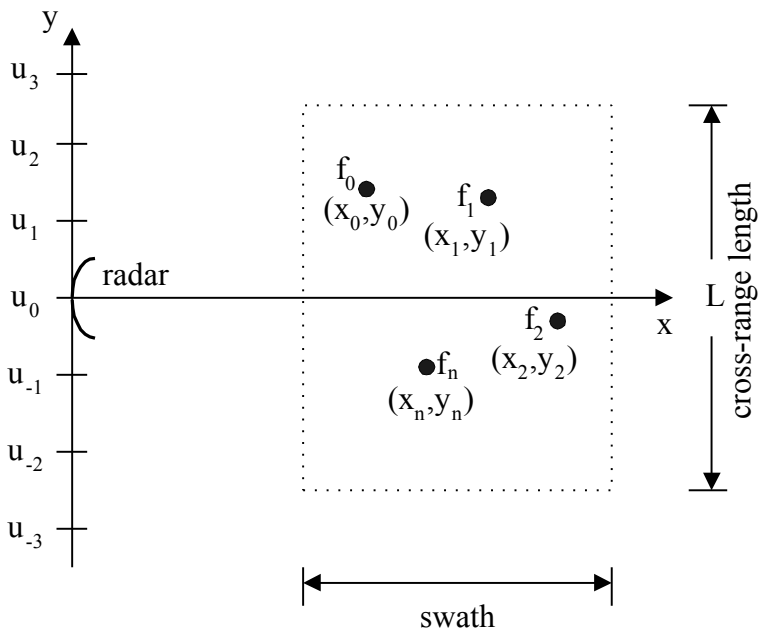

Figure 1.2: Typical stripmap SAR scenario in the plan formed by the slant-range and cross-range axis.

In radar imaging we are interested in estimate the target function. To achieve this goal we will start by looking at the signal received by the radar.

The echoed signal when the platform is at position $y = u$ is, in the fast-time frequency domain and in the slow-time spatial domain,

$$s(\omega, u) = P(\omega) \sum_{n=0}^{N-1} a(\omega, y_n - u) f_n e^{-j2kr_n}. \tag{1.2.3}$$

where $P(\omega)$ is the Fourier transform of the emitted pulse $p(t)$, a is the two-way antenna radiation pattern in the (ω, u) domain, and $k = (\omega+\omega_0)/c$ is the wavenumber. Symbol f_n absorbs the attenuation due to the wave divergence and denotes the complex reflectivity of the nth target that is taken to be independent of the aspect angle[2].

[2]Most man-made targets exhibit reflectivity depending on the aspect angle. However, this assumption greatly simplifies the formulation and yet leads to good results.

Symbol r_n denotes the distance between the radar and the nth target and is given by

$$r_n = \sqrt{x_n^2 + (y_n - u)^2}. \tag{1.2.4}$$

In appendix A we show that the Fourier transform of the $s(\omega, u)$ with respect to the slow-time domain is,

$$S(\omega, k_u) = A(\omega, k_u) P(\omega) \sum_{n=0}^{N-1} f_n e^{-j\sqrt{4k^2 - k_u^2} x_n} e^{-jk_u y_n}. \tag{1.2.5}$$

Comparing (1.2.2) with (1.2.5) we can write

$$S(\omega, k_u) = A(\omega, k_u) P(\omega) F(k_x, k_y), \tag{1.2.6}$$

where

$$k_x \equiv \sqrt{4k^2 - k_u^2} \tag{1.2.7}$$

and

$$k_y \equiv k_u \tag{1.2.8}$$

To estimate the target function we can use a matched filtering approach, which is the most frequently used in SAR applications at it is light from the computational point of view and it is robust to model mismatches. Other directions are !!!!!!!!!!!!!!!!!!!

The output of the matched filter is thus

$$\hat{F}(k_x, k_y) = A(\omega, k_u)^* P(\omega)^* S(\omega, k_u), \tag{1.2.9}$$

resulting,

$$\hat{F}(k_x, k_y) = |A(\omega, k_u)|^2 |P(\omega)|^2 \sum_{n=0}^{N-1} f_n e^{-jk_x x_n} e^{-jk_y y_n}. \tag{1.2.10}$$

In the spatial domain, we have

$$\hat{f}(x,y) = \sum_{n=0}^{N-1} f_n h(x - x_n, y - y_n), \tag{1.2.11}$$

where h denotes the SAR system transfer function

$$h(x,u) \equiv R_a(u,t) R_p \left(\frac{ct}{2} = x \right). \tag{1.2.12}$$

Functions R_a and R_p denote the auto-correlation of the antenna radiation pattern and the auto-correlation of the emitted pulse, respectively, given by the computation of the inverse Fourier transform of $|A(\omega, k_u)|^2$ and $|P(\omega)|^2$, respectively.

The wavefront reconstruction algorithm block diagram is presented in Fig. 1.2.1 and is now summarized by the following step sequence:

1. Compute the two-dimensional Fourier transform of the received signal $s(t,u)$, obtaining the signal $S(\omega, k_u)$.

2. Implement the matched filtering approach in the frequency domain. This is done via multiplying $S(\omega, k_u)$ by the complex conjugate of $S_0(\omega, k_u) = A(\omega, k_u)P(\omega)$.

3. Implement the change of variables (1.2.7) and (1.2.8). This change of variables is done via an interpolation.

4. Calculate the two-dimensional inverse Fourier transform (1.2.10), obtaining $\hat{f}(x,y)$, the estimate of the target function.

This imaging algorithm, although presented very recently in the SAR context, belongs to a class of algorithms often referred to as *wavenumber domain* or $\omega - k$ processors, whose roots are not new. This kind of processors as been used to perform seismic signal processing for imaging the substrata of Earth [27], [56]. This ideas were latter applied to imaging of SAR data (see, e.g., [9], [51], [52]).

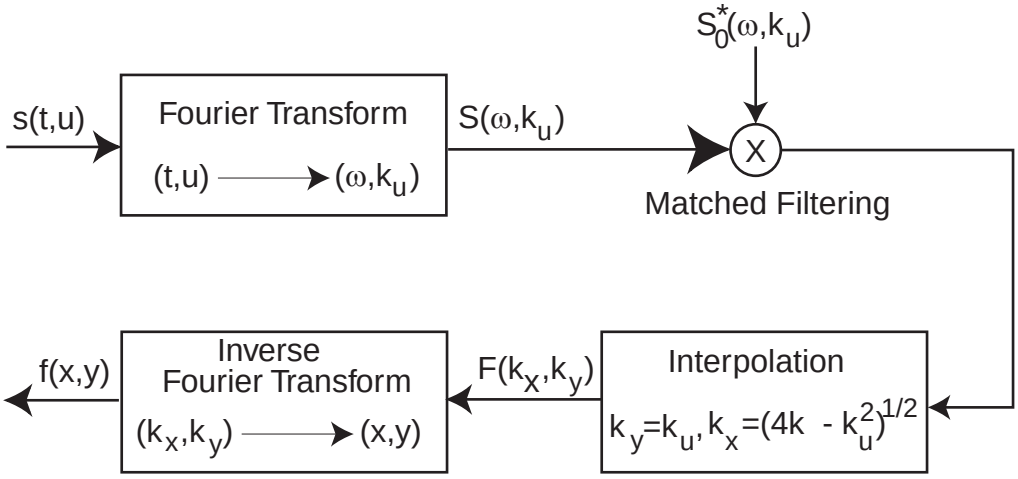

Figure 1.3: Wavefront algorithm block diagram (adapted from [55, ch. 4]).

1.2.2 Other SAR Imaging Algorithms

The wavefront reconstruction algorithm involves three major steps: i) Range compression; ii) Range cell migration compensation; iii) Azimuth compression. A large number of SAR focusing algorithms, besides the wavefront reconstruction algorithm, has been presented in the literature. To reduce the computational requirements, at expense of image quality, some of the algorithms implement approximated range migration compensation or they do not implement it at all. Herein we will just make a brief summary of the three most popular focusing algorithms, besides the wavefront reconstruction, for stripmap SAR.

Range-Doppler Algorithm

This algorithm is probably one of the most known SAR focusing schemes [2]. It starts with the 1-D transform of $s(t,u)$ to $s(t,k_u)$. The coupling between the range (time) and k_u is removed by a coordinate remapping which demands interpolation. The azimuth compression is done in the k_u domain. A single compression in the

range-Doppler domain for each range is then applied to all pixels at the same range. In systems where range cell migration is small, the Fresnel approximation can be used without degrading too much the image quality and the interpolation step can be ignored (see [28]).

Chirp-Scaling Algorithm

The Chirp-Scaling Algorithm does start with the raw-echo data (without range pulse compression) because it exploits the linear FM (LFM) signal structure in the transmitted pulse [49]. If coded or pseudorandom sequences have been used for the transmitted pulse, data must be compressed with the adequate signal and then respread by a convolution with a LFM pulse [28]. As in the range-Doppler approach, the algorithm starts with a 1-D transform in the slow-time domain of $s(t, u)$ to $s(t, k_u)$. Then $s(t, k_u)$ is multiplied by a phase-only chirp which *scales* the range chirp for each k_u and t so that the Doppler loci of all targets end up with a common range migration in phase. The scaled data is then Fourier-transformed to (ω, k_u) domain, where range compression and range cell migration compensation is performed. Azimuth compression and residual phase compensation is then done in the (t, k_u) domain.

Time Domain Correlation Algorithm

The basic principle behind the time domain correlation (TDC) imaging algorithm is simply the implementation of the matched filtering via a two-dimensional correlation [55, ch. 4.7]. To reduce the numerical errors the signal is upsampled (interpolated). The major drawback of this algorithm is the high computational cost due to the *brute force* approach.

1.3 Moving targets

Moving target detection, imaging, and trajectory estimation is a very active area of research and is needed for both civilian and military applications [7], [13], [23], [48], [21], [32]. In the following subsections we will study the effects of moving objects on the received SAR signal and present modifications of the wavefront reconstruction algorithm to get focused images of moving objects. The *blind angle ambiguity* limitation is also addressed. Finally, we present the state-of-the-art strategies to detect, image and estimate the kinematics of moving targets.

1.3.1 Focusing with the WaveFront Reconstruction Algorithm

Let us consider the radar platform traveling at speed v_r illuminating a point-like target with complex reflectivity f_m, which is moving with velocity $(v_x, v_y) = (\mu v_r, b v_r)$ in the spatial (x, y) domain. When the radar is at position $u = 0$, the moving target coordinates are (x_0, y_0). The target distance from the radar when the platform is at slow-time coordinate $y = u$ is

$$r(u) = \sqrt{(x_0 - \mu u)^2 + [y_0 - (1+b)u]^2}. \tag{1.3.1}$$

!!!! EXPLAIN THE MINUS SIGNS OF EQ R(U) !!!!

Distance r can be written in a more compact form, if we expand the square-root arguments of (1.3.1) and denote $\nu \equiv 1 + b$, i.e.,

$$r(u) = \sqrt{X^2 + (Y - \alpha u)^2}, \tag{1.3.2}$$

where

$$X^2 + Y^2 = x_0^2 + y_0^2, \tag{1.3.3}$$

$$\alpha Y = \mu x_0 + \nu y_0, \tag{1.3.4}$$

$$\alpha = \sqrt{\mu^2 + \nu^2}. \tag{1.3.5}$$

Following Soumekh's terminology (see [55, ch. 6.7]), (X, Y) are the *motion-transformed coordinates*, $\sqrt{X^2 + Y^2}$ is the *radial range*, αY is the *squint cross-range*, and α is the *relative speed*. Solving equations (1.3.3), (1.3.4), and (1.3.5) with respect to (x_0, y_0), we obtain

$$\begin{bmatrix} x_0 \\ y_0 \end{bmatrix} = \frac{1}{\alpha} \begin{bmatrix} \nu & -\mu \\ \mu & \nu \end{bmatrix} \begin{bmatrix} X \\ Y \end{bmatrix}.$$

The motion-transformed coordinates (X, Y) are thus a rotation of angle $\arctan(\mu/\nu)$ of coordinates (x_0, y_0).

The fast-time Fourier transform of the received signal from a moving target can thus be written as

$$s_m(\omega, u) = a(\omega, u) P(\omega) f_m e^{-j2k\sqrt{X^2 + (Y - \alpha u)^2}}. \tag{1.3.6}$$

To compute the slow-time Fourier transform of (1.3.6) we use the stationary phase method. By noting that $a(\omega, u)$ is a smooth function of u when compared with the phase term (details are shown in Appendix A.2), we get

$$S_m(\omega, k_u) = A(\omega, k_u) P(\omega) f_m e^{-j\sqrt{4k^2 - \left(\frac{k_u}{\alpha}\right)^2} X - j\frac{k_u}{\alpha} Y}. \tag{1.3.7}$$

If the parameter α is known, the wavefront algorithm can be applied to obtain

focused images of moving targets. Only the interpolation step modification, i.e.,

$$k_X = \sqrt{4k^2 - \left(\frac{k_u}{\alpha}\right)^2}, \tag{1.3.8}$$

and

$$k_Y = \frac{k_u}{\alpha}. \tag{1.3.9}$$

The estimation of parameter α can be accomplished as suggested by Soumekh in [55, ch. 6.7]. In Chapter 3 of this thesis we present an alternative methodology to compute α.

1.3.2 Blind angle ambiguity

The mapping from (x_0, y_0, μ, ν) to (X, Y, α) is not one to one; therefore, assuming that vector (X, Y, α) is known, we can not determine the complete moving target vector (x_0, y_0, μ, ν). The blind angle ambiguity refers to the fact that equations (1.3.3), (1.3.4), and (1.3.5) do not allow us to determine the directions of vectors (μ, ν) and (x_0, y_0), but only their norm [equations (1.3.3) and (1.3.5), respectively] and the angle between them: notice that αY given by (1.3.4) is the inner product between (μ, ν) and (x_0, y_0).

Figure 1.4 illustrates the blind angle ambiguity. It considers two moving targets with velocity vectors $v_i = (\mu_i, \nu_i)$ and radar coordinates $x_i' = x_i - \mu_i u$ and $y_i' = y_i - \nu_i u$ where $i = 1, 2$. Although the velocity vector of each of the moving targets has a different angle, their distances to the radar, $r = \sqrt{(x'^2 + y'^2)}$, are the same. Therefore, the phase term of the echoed signal from the moving targets, does not have sufficient information regarding the velocity vector direction. However, despite the fact that their distance to the radar is the same, they are illuminated from a different angle.

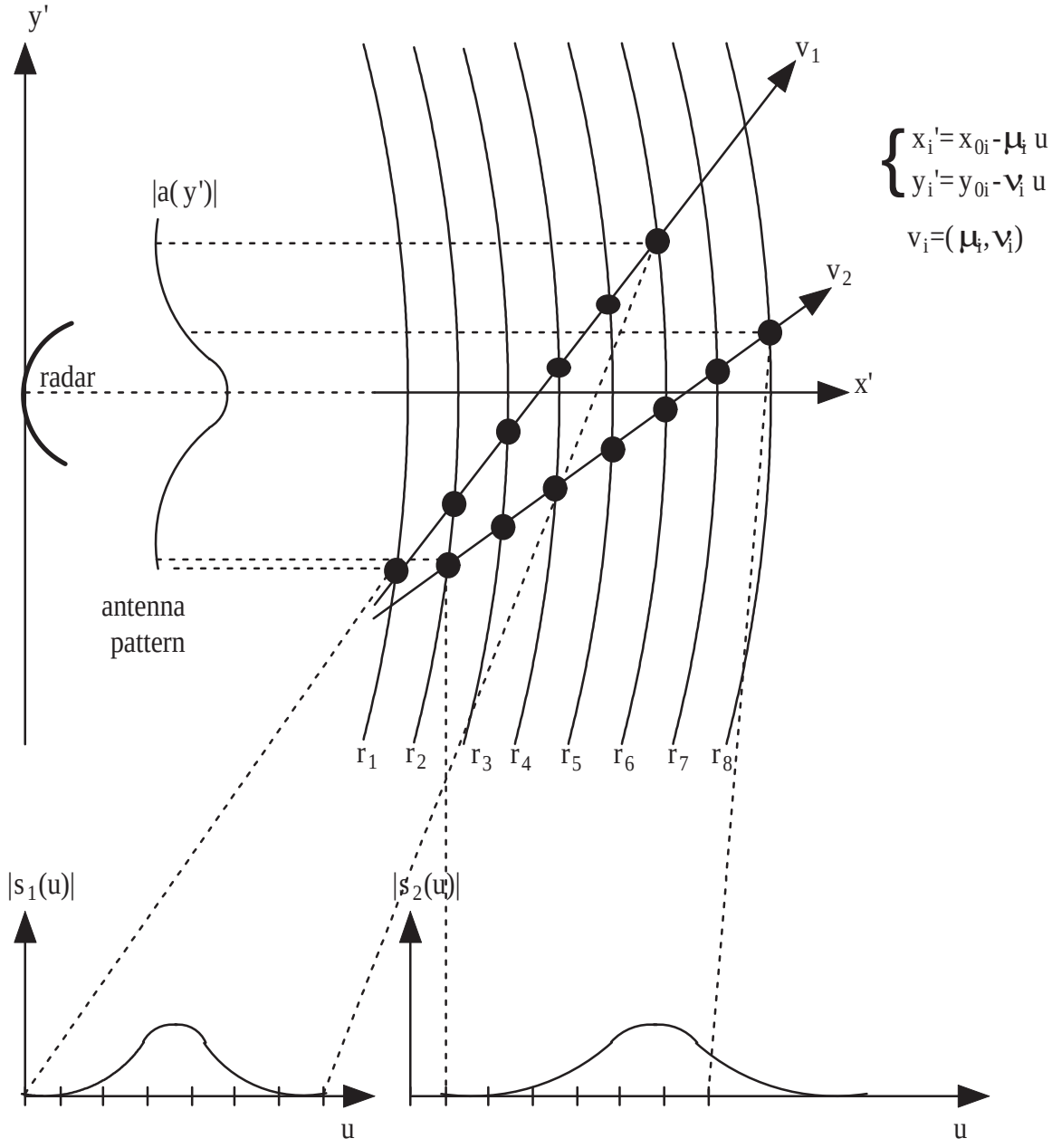

Figure 1.4: Illustration of the blind angle ambiguity.

Thus, the antenna radiation pattern magnitude induces an amplitude variation on the echoed signal that is different for each target. This effect on the amplitude of the received signal is clearly seen on the plots of $|s_1(u)|$ and $|s_2(u)|$, at the bottom of the figure. As a result, we will show in the next chapter of this thesis that this ambiguity can be solved by using the antenna radiation pattern knowledge. This result goes against the claims made by Soumekh in [54] and Barbarossa in [4] stating that the blind angle ambiguity cannot be solved unless stereo measures are available.

1.4 State-of-the-art in Moving Target Detection, Imaging, and Trajectory Estimation

In this subsection we briefly describe some recently proposed techniques to detect, to image and to estimate the kinematics of moving targets. We separate the techniques into two categories: single SAR sensor based and array of SAR sensors based. As we will see, the methodologies using more than one channel have greater ability to reduce the unwanted returns from the clutter and thus increase the detectability of slowly moving targets. Moreover, the techniques based on an array of sensors do not suffer from the so-called blind angle ambiguity [54], [55]. On the other hand, the techniques based on a single SAR sensor require lower mission costs, use smaller amounts of data, and are lighter from the computational point of view.

1.4.1 Single-Antenna SAR

Sub-aperture approach

In [37] Kirscht proposed an approach to moving target detection and velocity estimation based on a sequence of single-look SAR images obtained by splitting a single-channel SAR synthetic aperture into several smaller sub-apertures. These images are processed using different look center frequencies, therefore showing the ground at different look angles and at different times. The cross-range velocity component is obtained from the moving target displacements estimated between successive single-look SAR images. The slant-range velocity component is estimated by evaluating the variation of the signal amplitude during the sequence. This approach relies on thorough measurements of the moving target position and amplitude. This requirement is hard to fulfill, as moving targets appear defocused and/or split when focused with wrong velocity parameters.

Keystone Mapping

The goal of keystone mapping is the formation of SAR images of moving targets without using any specific knowledge of target motion. The method uses one-dimensional interpolation of the deramped phase history which is called by the authors as *keystone formatting*. The keystone interpolation is used to compensate the first-order phase which corresponds to the linear range migration. The major drawback of the method is that the applied compensation introduces coupling in the higher order phase terms. In order to have focused images of the moving objects it is necessary to combine the keystone mapping with other algorithms to compensate for the mentioned phase coupling.

Joint Time-Frequency Analysis - TF

Time-frequency analysis has been applied to imaging of moving objects in several recent publications [5], [12], [13].

In [5] Barbarossa investigated the use of the Wigner-Ville distribution (WVD) to extract the phase history of the echoes received from a moving object, necessary to produce a high-resolution image. The range migration problem is dealt with by degrading the resolution in the range direction. The technique only works well when applied to a single point-like target. It does not yield good results in the case of extended targets or targets with more than one predominant reflector due to the undesired cross-term products of the WVD. In [11] and [12], Victor Chen proposes another approach based also on joint time-frequency analysis that is adequate for extended objects with complex motion that induce Doppler-shifts changing over the time, such as rotating or maneuvering objects. This is a scenario more frequent in inverse synthetic aperture radar (ISAR). In this case a constant Doppler-shift cannot be assumed in the integration interval because each scatterer that composes the moving object has a different velocity from the others scatterers and is changing with time. A phase compensation cannot be applied to all scatterers simultaneously. The proposal consists in using time-frequency transforms at each range cell and generating a Doppler frequency versus time distribution. This results in a cube with axis Time-Doppler-Range. A sequence of 2-D complex range-Doppler images is obtained via sampling on the time axis. The principle is very simple and the results presented with simulation results are good. However, the computational cost is high.

1.4.2 Multiple-Antenna SAR

Besides the blind angle ambiguity, the detection and parameter estimation of slowly moving targets or targets with velocity parallel to the radar velocity is another difficulty for single-antenna based systems. The reason is the totally, or almost totally, overlapping between the moving target spectra and the clutter spectrum. The utilization of more than one receiving antenna exploiting multi-channel and space-time-frequency processing schemes have been proposed as a way to overcome the limitation of single-antenna based methods. Examples are the multi-channel SAR [22], [19], the linear antenna array or velocity SAR (VSAR) [26], the dual-speed SAR [59], and the multi-frequency antenna array SAR (MF-SAR) [60]. Each one of these methods yields better results than the single-channel approaches, at the expense of higher complexity in the respective hardware and software.

Displaced Phase Center Antenna - DPCA

The purpose of the displaced phase center antenna is to increase the moving target detection ability via the suppression of the clutter. It was proposed in 1953 by Dickey and Santa [17]. This technique uses two side-looking antenna apertures along the flight track. The PRF is such that if a pulse is transmitted at the first antenna position, then the second antenna will transmit a pulse when it moves to the position where the first aperture was located when the first pulse was transmitted. Thus, the echoes of static targets can be cancelled, the same not being true for the moving targets. Because this procedure is difficult to implement without significant errors, electronic DPCA was introduced. In this technique the PRF need not be matched exactly to the antenna spacing and platform velocity because phase corrections can

be applied. By canceling the echoes from the static targets, the DPCA technique improves target detectability over single channel based systems.

Space-Time Adaptive Processing - STAP

Space-time adaptive procecessing (STAP) is a generalization of the DPCA technique where multiple antennas are used. This technique was proposed in the 70's [8] and is still being the subject of many recent publications [61], [38], [39]. When the radar receives a set of returns each is stamped by its time of arrival and by the spatial position of the apertures. With STAP processing, SAR is able to detect moving targets and produce images of both stationary targets and moving targets at their correct positions. The major drawback of this processing scheme is the huge computational effort and memory requirements needed to implement it.

Space-Time-Frequency Processing

Space-time-frequency processing of SAR signals was proposed by Barbarossa in [6]. The purpose is the detection and high resolution SAR imaging of moving objects on the ground.

The space-time processing uses a linear array of antennas and applies 2-D filtering in space-time domain to improve the signal-to-clutter ratio. The recorded signal mapped onto the time-frequency domain by computing its Wigner-Ville distribution for estimation of its instantaneous frequency. The major draw-backs are the following:

i) Targets must be point-like, they have to be well isolated, and the clutter has to be highly attenuated, otherwise the cross-terms of WVD will certainly impair the instantaneous frequency estimation;

ii) Range resolution is degraded to cope with range migration;

iii) Computational cost is high, both in processing and data-storage.

Velocity SAR - VSAR

This configuration uses several antennas along the direction of flight. A single antenna transmits and the array of antennas record the echoes. This technique was proposed by Friedlander and Porat in [25] with the purpose of detecting and relocating moving targets. The VSAR processor produces a cube with axis range - cross-range - velocity. The result consists in multiple images for the different scatterers velocities. The major drawback of VSAR are the huge computational requirements and low accuracy in the relocation of fast-moving targets. In [58], Xia proposed an extension of VSAR by using more than one carrier frequency, the multi-frequency VSAR (MF-VSAR). Using that scheme the fast-moving targets can be accurately relocated. This technique requires however a huge amount of data to process, besides the high mission costs.

1.5 Conclusion

This chapter introduced the stripmap SAR geometry and summarized some of the most popular imaging algorithms in the SAR community. The framework of the wavefront reconstruction algorithm was introduced. We then addressed the problem of moving targets imaging and presented the modifications required by the wavefront algorithm in order to achieve correctly focused images of that kind of targets. Basically, the wavefront reconstruction algorithm was adapted to depend of parameter $\alpha = \sqrt{\mu^2 + \nu^2}$, the magnitude of the relative velocity of the moving targets with

respect to the radar. The blind angle ambiguity was then pointed out. This ambiguity refers to the fact that the mapping from the moving object initial coordinates and velocity vector (x_0, y_0, μ, ν) to the motion transformed coordinates and relative velocity vector magnitude (X, Y, α) is not one to one. That is, if vector (X, Y, α) is known we cannot determine the directions of vector (μ, ν) and vector (x_0, y_0), but only their norm and the angle between them. By using only the phase of the signal echoed by a moving target, one needs to have stereo measurements to solve the blind angle ambiguity.

At the end of the chapter we have summarized the state-of-the-art methodologies to deal with moving targets, more specifically, to detect, to image, and to estimate the trajectory parameters of moving targets. These methodologies were separated into two categories: the strategies using a single SAR sensor and strategies using an array of sensors. The main conclusion is that the techniques which rely on data from an array of sensors do not suffer from the blind angle ambiguity and have greater capability to deal with slowly moving targets. However, they are more expensive, not only from the computational point of view, because of the huge quantity of data to process, but also due to the higher number of sensors required, which, in some situations, leads to prohibitive mission costs.

Chapter 2

Solving the Blind Angle Ambiguity

2.1 Introduction

In the previous chapter we characterized the so-called *azimuth position uncertainty problem* or *blind angle ambiguity*. This ambiguity refers to impossibility of inferring the complete moving target trajectory parameter vector from the phase history of a single antenna based SAR sensor. In this chapter we will show that this limitation can be overcome by introducing information about the antenna radiation pattern.

We start by deriving the analytical expression of the term due to the antenna radiation pattern on the expression of the signal echoed by a moving target. Basically, we will see that the returned echo in the slow-time frequency domain is a scaled and shifted replica of the antenna radiation pattern. The scale and the shift depend on the cross-range velocity and on the slant-range velocity, respectively. Therefore, the blind angle ambiguity may be solved by exploiting the joint information of the antenna radiation pattern and the phase history. To find bounds on the estimation accuracy, we compute the Fisher information matrix for the velocity parameters of the received signal as function of the antenna radiation pattern. This bound supply us with a tool

to select the best antenna radiation patterns. At the end of the chapter, the derived bounds are compared with results provided by the estimator published by us in [47].

2.2 Antenna Radiation Pattern in Slow-Time Frequency Domain

Let us recall that the expression for the received echo from a moving object in the two-dimensional frequency domain is given by (see page 14)

$$S_m(\omega, k_u) = A(\omega, k_u) P(\omega) f_m e^{-j\psi}, \tag{2.2.1}$$

where

$$\psi = \sqrt{4k^2 - \left(\frac{k_u}{\alpha}\right)^2} X + \frac{k_u}{\alpha} Y. \tag{2.2.2}$$

Let us now concentrate on the antenna pattern $A(\omega, k_u)$. Soumekh in [55, ch. 6.7], based on the Fourier decomposition of a spherical wave, derives a formula for $A(\omega, k_u)$, valid for static targets. Herein, we present a different approach to compute $A(\omega, k_u)$, valid for constant velocity moving targets.

The two-way antenna radiation pattern from a planar aperture illuminated with constant polarization is [14, ch. 4]

$$a(\theta, \phi, \omega) \propto g^2(k \sin\theta \cos\phi, k \sin\theta \sin\phi), \tag{2.2.3}$$

where $g(k_{y_a}, k_{z_a})$ is the Fourier transform of the electrical field in the antenna aperture and θ and ϕ are the spherical coordinates angles shown in Fig. 2.1.

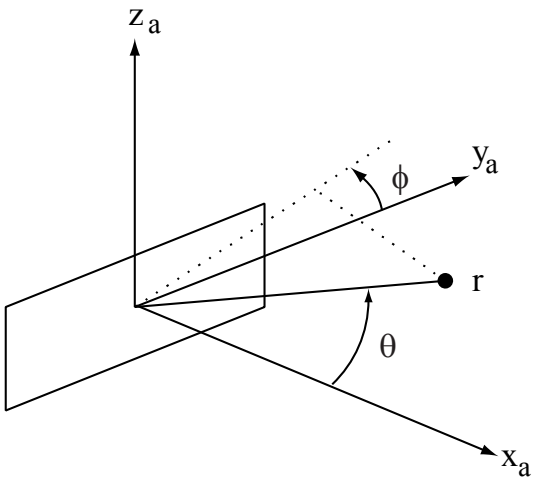

Figure 2.1: Antenna aperture in the plane $x_a = 0$, where x_a, y_a, z_a are orthogonal axes.

From Fig. 2.2 we see that

$$k_{y_a} \equiv k \sin\theta \cos\phi = k\frac{\Delta y_a}{r} = k\frac{y_0 - \nu u}{r} \tag{2.2.4}$$

$$k_{z_a} \equiv k \sin\theta \sin\phi = k\frac{\Delta z_a}{r} = k\frac{x_0 - \mu u - \bar{x}}{r}\tan\beta. \tag{2.2.5}$$

On the other hand, replacing αY and α^2, given respectively by (1.3.4) and (1.3.5), into (2.2.2) we obtain, after some manipulation,

$$k_u = 2k\mu\frac{x_0 - \mu u}{r} + 2k\nu\frac{y_0 - \nu u}{r}. \tag{2.2.6}$$

From (1.3.1) and (2.2.4), we have

$$\frac{x_0 - \mu u}{r} = \sqrt{1 - \left(\frac{k_{y_a}}{k}\right)^2}. \tag{2.2.7}$$

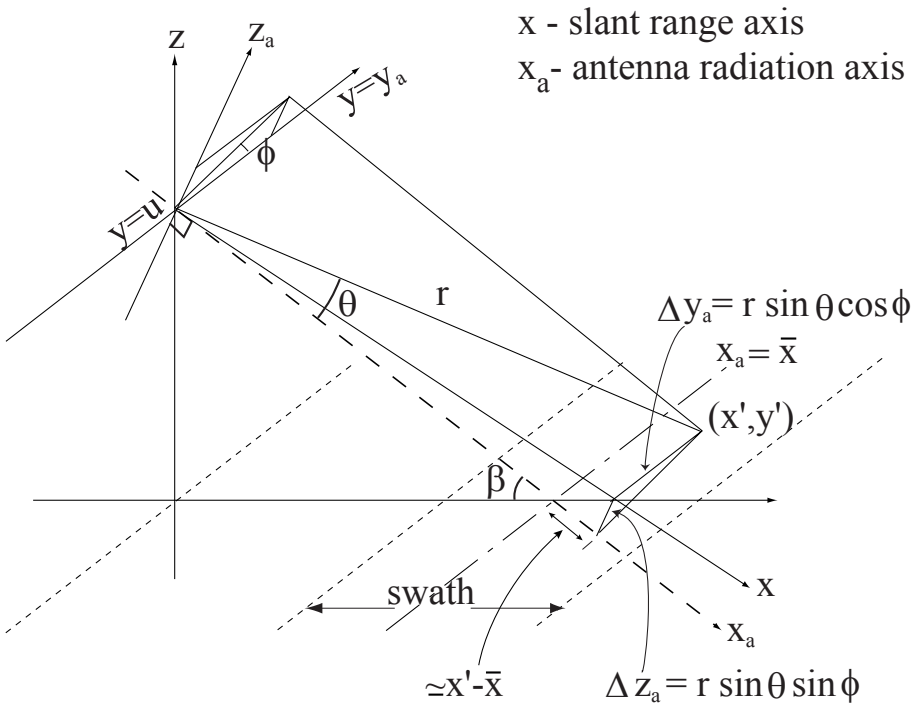

Figure 2.2: Antenna aperture in the plane $x_a = 0$, at cross-range $y = u$, moving at constant altitude in the cross-range direction, and illuminating a moving target with slant-plane coordinates $(x = x' = x_0 - \mu u, y = y' = y_0 - bu)$.

Introducing (2.2.7) and (2.2.4) into (2.2.6), we obtain

$$k_u = 2k\mu\sqrt{1-\left(\frac{k_{y_a}}{k}\right)^2} + 2\nu k_{y_a}. \tag{2.2.8}$$

Equation (2.2.8) can be converted into a $2nd$ order polynomial and solved with respect to k_{y_a}. We note however that $\sqrt{1-(k_{y_a}/k)^2} \simeq 1-(\sin\theta\cos\phi)^2/2$. As a numerical example let us suppose that the antenna beamwidth is smaller than, say, 10°. In this situation $(\sin\theta\cos\phi)^2/2 < 4\times10^{-3}$. Therefore, the approximation $\sqrt{1-(k_{y_a}/k)^2} \simeq 1$ is valid for most SAR applications, since they typically use much narrower beamwidths. We have then

$$k_{y_a} \approx \frac{1}{2\nu}[k_u - 2k\mu], \tag{2.2.9}$$

and

$$k_{z_a} \approx k\left(1-\frac{\bar{x}}{r'}\right)\tan\beta, \tag{2.2.10}$$

where r' denotes the range corresponding to the middle of the integration interval. The expression for k_{z_a} was obtained by replacing (2.2.7) into (2.2.5) and again noting that $\sqrt{1-(k_{y_a}/k)^2} \simeq 1$.

The spatial frequency k_{z_a} depends on the wavenumber k and on the target range r'. Let us assume that the moving target and the background, made of static targets, have been spotlighted such that the target region is confined to $(x,y) \in [x_m, x_M]\times[y_m, y_M]$. If $x_M - x_m$, the length of the target area in slant-range, is much smaller than $\bar{x}$, then $\bar{x}/r' \simeq 1$ and we have

$$A(\omega, k_u) \propto g^2\left[\frac{1}{2\nu}(k_u - 2k\mu), 0\right], \tag{2.2.11}$$

i.e., the range dependence of $A(\omega, k_u)$ can be neglected. If $x_M - x_m$ is not much smaller than $\bar{x}$, then the antenna radiation pattern becomes dependent on the range

r'. However, this dependency can be removed by introducing a proper slant-range dependent gain. From now on we assume that the antenna radiation pattern does not depend on r'.

In deriving $A(\omega, k_u)$, we have assumed that the antenna has broadside geometry, i.e., the antenna radiation axis is orthogonal to the azimuthal direction. However, there are situations, for example due to wind drift, in which the antenna displays squinted geometries. In order to include general geometries in the echo amplitude $A(\omega, k_u)$, let us assume that the antenna aperture shown in Fig. 2.2 has been rotated by an angle θ_0 with respect to axis z_a such that the rotated radiation axis has coordinates $\theta = \theta_0$ and $\phi = 0$. Notice that the antenna radiation pattern $A(\omega, k_u)$ given by (2.2.11) is parameterized only by the relative velocity vector (μ, ν) measured in the slant-plane defined by the coordinates y_a and x_a. Therefore, the antenna radiation pattern for a squinted geometry is given by

$$A(\omega, k_u) \propto g^2 \left[\frac{1}{2\nu_s}(k_u - 2k\mu_s), 0 \right], \tag{2.2.12}$$

where (μ_s, ν_s) is the relative velocity vector (μ, ν) expressed in the coordinates x_a and y_a rotated by θ_0; i.e.,

$$\begin{bmatrix} \mu_s \\ \nu_s \end{bmatrix} = \begin{bmatrix} \cos\theta_0 & \sin\theta_0 \\ -\sin\theta_0 & \cos\theta_0 \end{bmatrix} \begin{bmatrix} \mu \\ \nu \end{bmatrix}.$$

The shift $k_{DC} \equiv 2k\mu_s$ is commonly termed the Doppler centroid.

As a conclusion, the illumination function in the slow-time Doppler domain, k_u, takes the shape of the antenna radiation pattern with respect to k_{y_a}. The shape becomes expanded by factor $2\nu_s$ and shifted by $2k\mu_s$. For broadside antenna geometry (i.e., $\theta_0 = 0$) the expansion is given by $2k\nu$ (i.e., depends only on the cross-range

relative velocity) and the shift is given by $2k\mu$ (i.e., depends only on the slant-range relative velocity).

Notice that the phase $\psi(\omega, k_u)$ is informative with respect to α, X, and Y, whereas $A(\omega, k_u)$ is informative with respect to μ_s and ν_s. Once these parameters have been inferred, we solve equations (1.3.3), (1.3.4), and (1.3.5) to determine the moving target parameters (μ_s, ν_s, x_0, y_0). The azimuth ambiguity is therefore solved using a single sensor.

The proposed method when applied to background targets without internal motion yields the Doppler centroid of these targets. This parameter is of prime importance in SAR imaging. Furthermore, and given that the relative velocity vector (μ, ν) of a background target is known before hand, the squint angle θ_0 can be obtained from the vector (μ_s, ν_s) of a background target by computing $\theta_0 = \text{angle}\,(\mu, \nu) - \text{angle}\,(\mu_s, \nu_s)$. Hence, we assume from now on that $\theta_0 = 0$.

In the remaining of the thesis we assume that the background targets are static (i.e., $\mu = 0$ and $\nu = 1$). This scenario happens in airborne SAR. However, all concepts and ideas apply to constant velocity moving background targets, as it happens, for example, in spaceborne SAR due to the earth rotation.

2.3 Design of the Antenna Radiation Pattern

In this section we derive the Fisher information matrix for the velocity vector of moving targets as function of the antenna radiation pattern. This study provides us with a tool for selecting the best antenna radiation patterns in the sense of achieving the best velocity estimates. We assume that the moving target parameters α, X, Y are

known in order to the Fisher information matrix depend only on the antenna radiation pattern and on the velocity parameters μ and ν. The narrow band approximation is also taken, that is, the antenna radiation pattern will not be considered as depending on the fast-time frequency.

Let us begin by considering a single moving target with constant complex reflectivity f_m, coordinates (x_0, y_0) when the platform is at position $y = 0$, and speed vector $(v_x, v_y) = (\mu v_r, b v_r)$ defined in the slant-plane (x, y); vector (μ, b) denotes the target relative velocity with respect to the radar. The nth ground static target has complex reflectivity f_n and coordinates (x_n, y_n). When the radar is positioned at the coordinate $y = u$, the corresponding received signal in the fast-time frequency domain ω and in the slow-time frequency domain k_u, after quadrature demodulation, is [see expressions (1.2.5) and (1.3.7)]

$$\begin{aligned} S(\omega, k_u) = P(\omega) A(k_u, \theta) f_m e^{-j\sqrt{4k^2 - \left(\frac{k_u}{\alpha}\right)^2} X} e^{-j\frac{k_u}{\alpha} Y} \\ + P(\omega) A(k_u, \theta_0) \sum_n f_n e^{-j\sqrt{4k^2 - k_u^2} x_n} e^{-jk_u y_n}, \end{aligned} \tag{2.3.1}$$

where $P(\omega)$ is the transmitted pulse, $k = 2\pi/\lambda$, $\theta = (\mu\nu)$, $A(k_u, \theta) \propto g^2\,[1/(2\nu)(k_u - 2k\mu)]$, $\nu = 1 + b$, $\alpha = \sqrt{\mu^2 + \nu^2}$, $\alpha Y = \mu x_0 + \nu y_0$, and $\sqrt{X^2 + Y^2} = \sqrt{x_0^2 + y_0^2}$.

The first term on the right hand side of equation (2.3.1) is due to the moving target; the remaining terms are due to the static ground. The reflectivity of all targets is assumed to be independent of the aspect angle. Vector $\theta_0 \equiv (0, 1)$ is the velocity of a static target. After pulse compression and phase compensation for the moving target (assuming α, X, and Y known) and computing the inverse Fourier

transform with respect to the fast-time frequency we obtain the signal $S_c(x, k_u)$[1],

$$\begin{aligned} S_c(x,k_u) &= R_p(x)A(k_u,\theta)f_m + A(k_u,\theta_0)\times \\ &\times \sum_n f_n R_p(x-x_n+X)e^{-j\frac{k_u^2}{4k}(x_n-\frac{X}{\alpha^2})}e^{-jk_u(y_n-\frac{Y}{\alpha})}, \end{aligned} \tag{2.3.2}$$

where the Fresnel approximation, i.e.,

$$\left[4k^2-(k_u/\alpha)^2\right]^{1/2} \approx 2k - \frac{1}{4k}\left(k_u/\alpha\right)^2, \tag{2.3.3}$$

and the narrow band approximation, i.e. $A(\omega, k_u, \theta) \approx A(k_u, \theta)$, were taken; function $R_p(x)$ is the auto-correlation of the transmitted pulse, computed at $t = 2x/c$.

2.3.1 Signal Statistics

Let us define $\mathbf{S} \equiv [S_{-N} \cdots S_0 \cdots S_N]^T$, where $S_i \equiv S_c(0, k_{u_i})$, $k_{u_i} = \frac{i}{2N}\Delta K$, for $i = -N, ..., 0, ..., N$, where ΔK is the spatial sampling frequency, assumed to be larger than the synthetic aperture bandwidth (spatial sampling interval smaller than half of the antenna azimuthal width). Define also $\mathbf{A}(\theta) = [A_{-N}(\theta) \cdots A_0(\theta) \cdots A_N(\theta)]$ where $A_i(\theta) = A(k_{u_i}, \theta)$.

If we assume that parameter θ is known, then only the noise term in the expression (2.3.2) is random. By considering that the number of static scatterers is large, none is predominant, and that they are uniformly distributed within a wavelength, then the complex noise term is circularly symmetric and Gaussian [33, ch. ??]!!!!!!!!. Density of vector $\mathbf{S}$ conditioned to θ and f_m is therefore

$$p(\mathbf{S}|f_m, \theta) = N(\widetilde{\mu}_s, \mathbf{C}_s), \tag{2.3.4}$$

[1]Although this notation is not strictly correct, since we are defining a function based on its arguments, we have adopted it for better clarity.

where $\widetilde{\mu}_S = E[\mathbf{S}]$ and $\mathbf{C}_s = E[(\mathbf{S} - \widetilde{\mu}_s)(\mathbf{S} - \widetilde{\mu}_s)^H]$. The operator $(.)^H$ denotes the conjugate transpose of a matrix.

We show in appendix that $E[\mathbf{C}_s] = 0$ and $\mathbf{C}_s = \sigma^0 L E_{R_p} \mathrm{diag}(|[A(\theta_\mathbf{0})]_i|^2)$, for $i = -N, ..., N$, where σ^0 is the backscattering coefficient of the clutter and E_{R_p} is the energy of the autocorrelation of the transmitted pulse. Then, the expected value of vector $\mathbf{S}$ is

$$E[\mathbf{S}] = f_m \mathbf{A}(\theta). \tag{2.3.5}$$

2.3.2 Velocity Estimation Bounds

We now compute the Fisher information matrix elements for the velocity parameters as function of the antenna radiation pattern. This matrix, for a circular complex Gaussian process is given by (see, e.g. [34, ch. 3])

$$\begin{aligned} [I(\theta)]_{ij} &= \mathrm{tr}\left[C_s^{-1}(\theta)\frac{\delta C_s(\theta)}{\delta\theta_i}C_s^{-1}(\theta)\frac{\delta C_s(\theta)}{\delta\theta_j}\right] \\ &+ 2\mathrm{Re}\left[\frac{\delta\tilde{\mu}^H(\theta)}{\delta\theta_i}C_s^{-1}(\theta)\frac{\delta\tilde{\mu}(\theta)}{\delta\theta_j}\right], \qquad i,j = 1,2. \end{aligned} \tag{2.3.6}$$

The first term in equation (2.3.6) is zero because the noise covariance matrix is independent of the moving target parameters. Recalling that $\tilde{\mu}(\theta) = f_m \mathbf{A}(\theta)$, then

$$\frac{\delta\tilde{\mu}^H(\theta)}{\delta\mu} = f_m^* \frac{-k}{\nu}[\dot{A}_0(\theta), \dot{A}_1(\theta), \cdots, \dot{A}_{N-1}(\theta)] \tag{2.3.7}$$

$$\frac{\delta\tilde{\mu}^H(\theta)}{\delta\nu} = f_m^* \frac{2k\mu - k_u}{2\nu^2}[\dot{A}_0(\theta), \dot{A}_1(\theta), \cdots, \dot{A}_{N-1}(\theta)], \tag{2.3.8}$$

where $\dot{A}(\theta) \equiv \partial A(k_u, \theta)/\partial k_u$.

After some algebraic manipulation the Fisher matrix elements can be written as

$$\begin{aligned} I_{11}(\theta) &= \kappa\frac{k^2}{\nu^2}\sum_{i=-N}^{N}\frac{|\dot{A}_i(\theta)|^2}{|A_i(\theta_0)|^2} \\ &\approx \frac{2N\kappa k^2}{\Delta K\nu^2}\int\frac{|\dot{A}(k_u,\theta)|^2}{|A(k_u,\theta_0)|^2}\,dk_u, \qquad (2.3.9) \\ I_{22}(\theta) &= \kappa\sum_{i=-N}^{N}\frac{|\dot{A}_i(\theta)|^2}{|A(\theta_0)_i|^2}\left(\frac{2k\mu-k_{ui}}{2\nu^2}\right)^2 \\ &\approx \frac{2N\kappa}{\Delta K}\int\frac{|\dot{A}(k_u,\theta)|^2}{|A(k_u,\theta_0)|^2}\left(\frac{2k\mu-k_u}{2\nu^2}\right)^2 dk_u, \qquad (2.3.10) \end{aligned}$$

and,

$$\begin{aligned} I_{12}(\theta) &= I_{21}(\theta) = \kappa\frac{-k}{\nu}\sum_{i=-N}^{N}\frac{|\dot{A}_i(\theta)|^2}{|A_i(\theta_0)|^2}\left(\frac{2k\mu-k_{ui}}{2\nu^2}\right) \\ &\approx \frac{2N\kappa(-k)}{\Delta K\nu}\int\frac{|\dot{A}(k_u,\theta)|^2}{|A(k_u,\theta_0)|^2}\left(\frac{2k\mu-k_u}{2\nu^2}\right)dk_u \qquad (2.3.11) \end{aligned}$$

where $\kappa = 2|f_m|^2/(\sigma^0 L)$, and it is assumed that $A(k_u,\theta_0) \neq 0$ for $k_u \in [-\Delta K/2, \Delta K/2]$.

Elements I_{11} and I_{22} refer to the slant-range velocity and to the cross-range velocity, respectively. A brief analysis of these two elements lead us to do the following conclusions:

- In practical applications, $A(k_u,\theta_0)$ is bandlimited, that is, it goes to zero as $|k_u|$ increases; therefore, as the shift between $\dot{A}(k_u,\theta)$ and $A(k_u,\theta_0)$ increases, the size of the integral where $A(k_u,\theta_0)$ is nearly zero increases, leading to larger integral values.

- The element I_{22} is affected by a quadratic factor centered on $k\mu$. This factor amplifies the integral by a factor proportional to its distance from the central frequency $k\mu$; therefore, the higher $|\dot{A}(k_u,\theta)|$ at the band extremes, the higher I_{22}.

- The information matrix element I_{11} is multiplied by $(k/\nu)^2 \approx k^2$, which implies better estimation results for the slant-range velocity component than for the cross-range velocity component.

Based on this analysis one can anticipate the following:

i) Higher range velocities lead to better estimates due to the larger displacements between $A(k_u, \theta_0)$ and $A(k_u, \theta)$;

ii) The slant-range velocity estimate is more accurate than the cross-range velocity estimate;

iii) Antenna radiation patterns with high derivatives at its band extremes lead to the best accuracy.

2.3.3 Simulation Results

We now consider three shapes of antenna radiation patterns: Gaussian, triangular and trapezoidal. The Cramer-Rao lower bound (CRLB) for the cross-range and slant-range speeds velocities is computed for each shape as function of the ground superposition. Table 2.1 shows the parameters used, where $|f_m|^2/(\sigma^0 L) = 1$.

Figures 2.3 and 2.4 plot the square root of the CRLB for the range and cross-range velocities versus the superposition $|K_a - k\mu|/K_a$, where K_a is the $-3\,\mathrm{dB}$ antenna bandwidth. The label *trapezoid*(x) refers to a trapezoid with top length equal to $(1-x)\%$ of the base length.

As expected, due to its higher derivatives at the band extremes, the trapezoidal

Table 2.1: Simulation parameters.

Parameter	Value
Carrier frequency	5GHz
Altitude	10Km
Velocity	300Km/h
Look angle	20^0
SNR	0dB

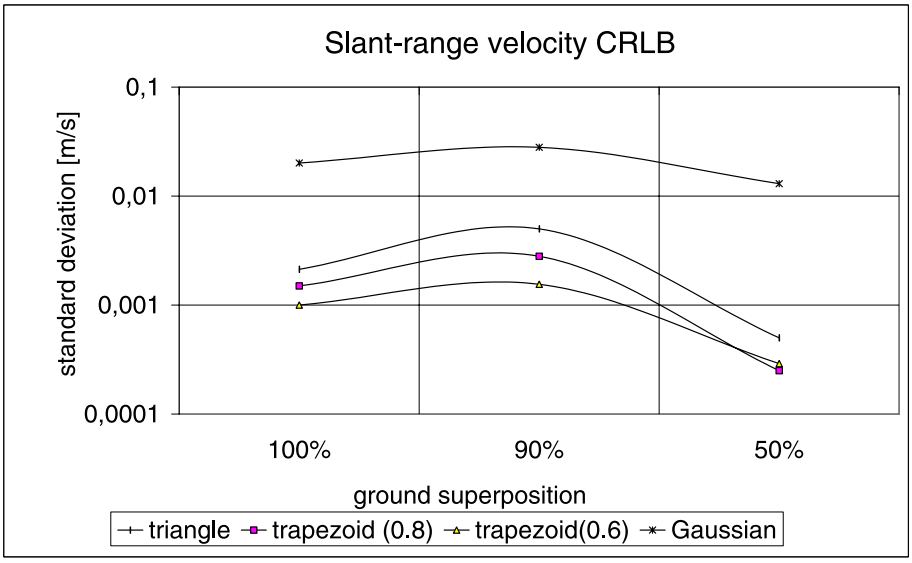

Figure 2.3: CRLB (square root) of slant-range velocity parameter versus the ground-return superposition.

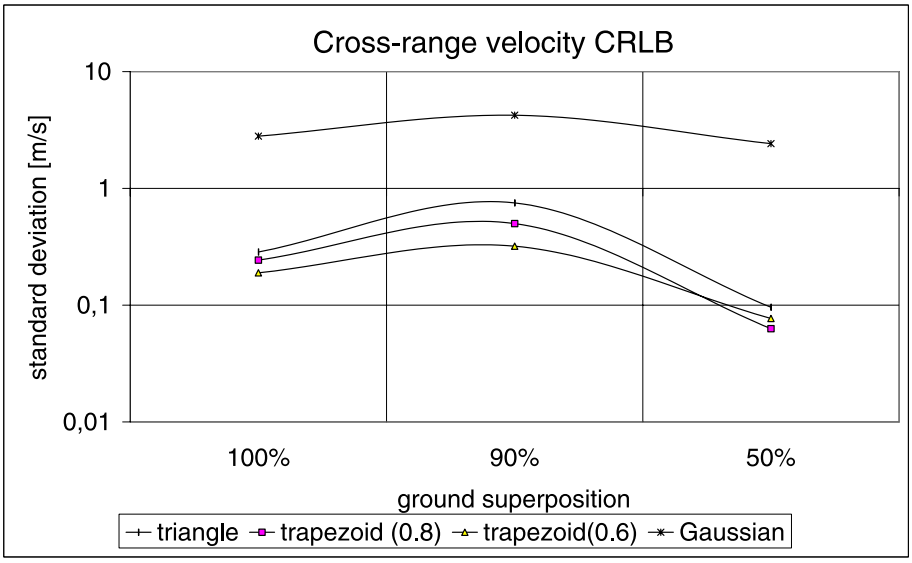

Figure 2.4: CRLB (square root) of cross-range velocity parameter versus ground-return superposition.

shape performs better followed by the triangular and by the Gaussian shapes. Notice that the Gaussian shape is nearly one order of magnitude worse than the remaining antenna radiation patterns.

Figures 2.5 and 2.6 plot sample standard deviations of the estimates from a velocity estimator developed by us in [46]. These experimental results are in agreement with those plotted in Fig.s 2.3 and 2.4, confirming the advantages of using antenna radiation patterns exhibiting significant derivatives at their band extremes.

2.4 Conclusions

In this chapter we derived the expression for the antenna radiation pattern in the (ω, k_u) domain for constant velocity moving targets. It was shown that the echoed signal is a scaled and shifted version of the antenna radiation pattern. The scale

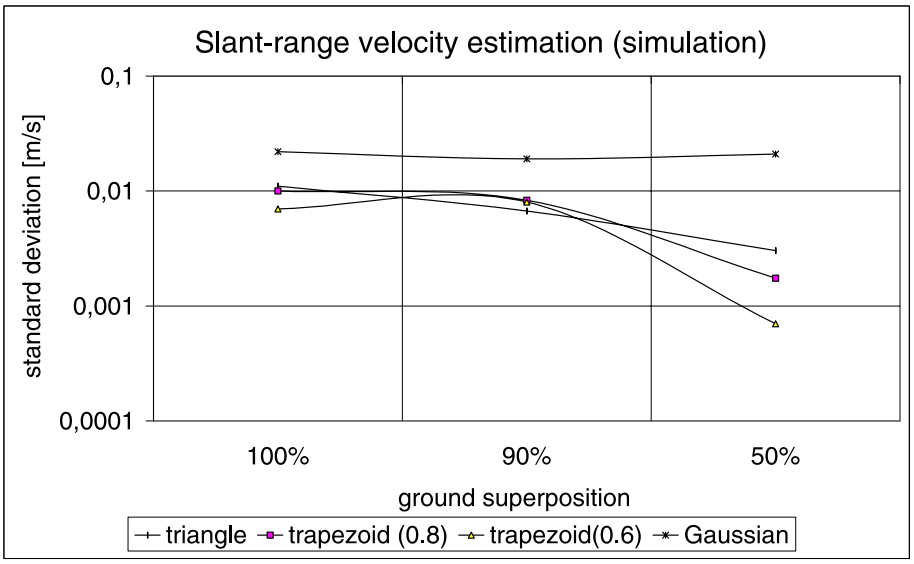

Figure 2.5: Standard deviation of slant-range speed parameter estimation versus ground-return superposition.

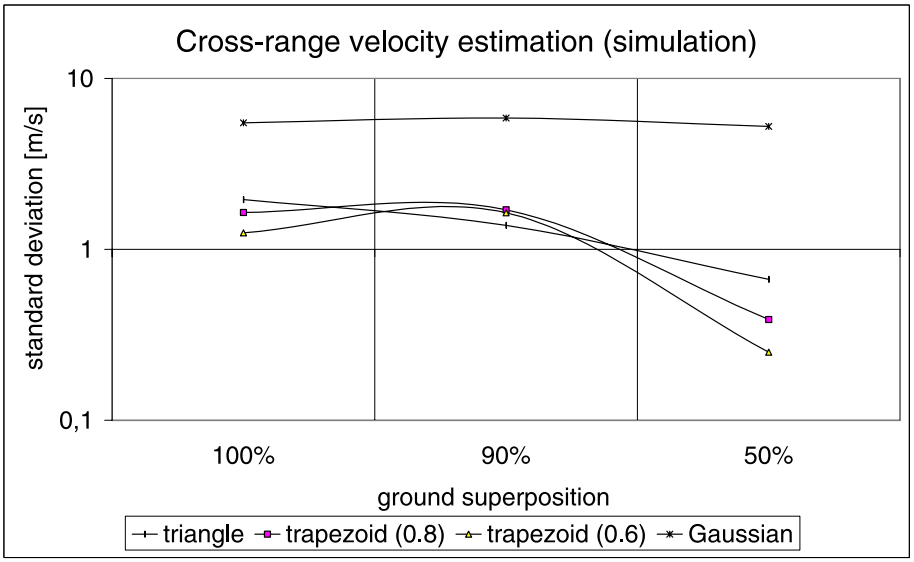

Figure 2.6: Standard deviation of cross-range speed parameter estimation versus ground-return superposition.

and the shift depend on the cross-range velocity and on the slant-range velocity, respectively. By exploiting the joint information of the antenna pattern and the phase history, the blind angle ambiguity was solved. We then computed the Fisher information matrix for the velocity parameters to see how accurate the measurements would be and how would they depend on the antenna radiation pattern. We concluded then that the velocity estimation could accurately be done and that the antenna radiation pattern should have high derivative at its band extremes. This theoretical behaviour was confirmed with results provided by an estimator developed by us in [47].

Chapter 3

Velocity Estimation and Trajectory Estimation Using a Single SAR Sensor

3.1 Introduction

In this chapter we propose a novel procedure to detect multiple moving targets and to estimate their parameters (velocity and coordinates) using a single SAR sensor. Basically, we exploit the structure of the amplitude and the phase modulations of the returned echo from a moving target in the Fourier domain. The echo amplitude is a scaled and shifted replica of the antenna radiation pattern; the scale and shift are functions of the slant-range and the cross-range velocities, respectively. The echo phase is a function of the moving target velocity magnitude and of the target coordinates. A generalized likelihood ratio test is then derived to detect moving targets and to estimate their trajectory parameters.

A crucial step in the detection/estimation scheme is a matched filtering operation, depending on the moving target parameters, that simultaneously copes with range

migration and compresses two-dimensional signatures into one-dimensional ones without degrading the slant-range resolution. This matched filtering operation introduces, therefore, a huge simplification on the detector/estimator structure.

The proposed technique yields good results, even for very low signal to clutter ratios (SCRs), whenever the moving target spectra are not totally overlapped with the clutter spectrum. Otherwise, the detector and the estimator still work provided that, roughly, SCR$>$ 10 dB.

The chapter is organized as follows. We start by characterizing the compressed signals when approximate moving target parameters are used. We then address aspects of cross-range sampling and derive background and noise statistics. A generalized likelihood ratio test to detect moving targets and estimate their kinematics parameters is proposed. The detection/estimation problem is formalized as one of detection and parameter estimation of deterministic signals immersed in Gaussian noise. An efficient scheme to compute the generalized likelihood ratio test is then proposed. At the end of the chapter we present results illustrating the effectiveness of the proposed methodology.

3.2 Compression of the Moving Target Echo

Let us consider a single moving target with parameters (μ, ν, X, Y, f_m) originating the echo

$$S(\omega, k_u) = S_m(\omega, k_u) + S_0(\omega, k_u), \tag{3.2.1}$$

where S_m and S_0 are due to the target and to the background, respectively, and

$$S_m(\omega, k_u) = P(\omega)A(k_u)f_m e^{-j\psi(\omega,k_u)}, \tag{3.2.2}$$

$$S_0(\omega, k_u) = P(\omega)A_0(k_u)\sum_n f_n e^{-j\psi_n(\omega,k_u)}, \tag{3.2.3}$$

where the dependency of A on ω has been omitted, vector $A_0(k_u)$ denotes the amplitude echo of a static target (i.e., $\mu = 0, \nu = 1$), and

$$\psi(\omega, k_u) = \sqrt{4k^2 - \left(\frac{k_u}{\alpha}\right)^2}X + \frac{k_u}{\alpha}Y, \tag{3.2.4}$$

and

$$\psi_n(\omega, k_u) = \sqrt{4k^2 - k_u^2}X + k_u Y. \tag{3.2.5}$$

According to (3.2.2), the moving target echo is spreaded over the two dimensional domain $(\omega, k_u) \in S_{PA}$, the support[1] of $P(\omega)A(k_u)$, thus introducing complexity in any moving target detection/estimation scheme. To compress the moving target echo into a one-dimensional domain, let us define the signal

$$s_c(t, k_u) \equiv \mathcal{F}^{-1}_{(\omega)}\left[S(\omega, k_u)P^*(\omega)e^{j\psi'(\omega,k_u)}\right], \tag{3.2.6}$$

where $\psi'(\omega, k_u)$ is given by (3.2.4) for moving target parameters $(\alpha', X', 0)$ *close* to $(\alpha, X, 0)$. In appendix A, we show that if $\mu \ll c/(BD_y)$, where c is the speed of light, B the pulse bandwidth, and D_y the cross-range aperture width, and $|X/\alpha^4 - X'/\alpha'^4| \ll (64\pi k_0^3)/|k_u|^4_{max}$, then

$$s_c(t, k_u) = \underbrace{f_m R_p[t - \tau(k_u)]A(k_u)e^{-j\eta(k_u)}}_{s_{mc}} + w(t, k_u), \tag{3.2.7}$$

[1] By support of g, we mean the set of (ω, k_u) points where $g(\omega, k_u) \neq 0$.

with

$$\tau(k_u) = \frac{2(X - X')}{c} + \frac{1}{c}\left(\frac{k_u}{2k_0}\right)^2 \left(\frac{X}{\alpha^2} - \frac{X'}{\alpha'^2}\right) \tag{3.2.8}$$

$$\eta(k_u) = -\frac{k_u^2}{4k_0}\left(\frac{X}{\alpha^2} - \frac{X'}{\alpha'^2}\right) + k_u\frac{Y}{\alpha} + \varphi, \tag{3.2.9}$$

where $R_p(t)$ is the deterministic autocorrelation of the transmitted pulse $p(t)$, $\varphi = 2k_0(X - X')$, and $w(t, k_u)$ is the term due to the background echo.

The energy of autocorrelation $R_p(t)$ is highly concentrated about $t = 0$. Therefore, the energy of $s_{mc}(t, k_u)$ is highly concentrated about $t = \tau(k_u)$. For $\alpha'^2 X = \alpha^2 X'$, the delay $\tau(k_u)$ does not depend on k_u, meaning that energy of $s_{mc}(t, k_u)$ is clustered along the cross-range direction. By exploiting this fact, we derive, in the next section, a moving target detector and parameter estimator that simultaneously copes with range migration and straightens the moving target signatures in the (t, k_u) domain along coordinate k_u without degrading the slant-range resolution. For a given X', the estimator scans the set $\alpha \in [\alpha_{min}, \alpha_{max}]$ and detects moving targets with coordinate X in an interval such that $|X/\alpha^4 - X'/\alpha'^4| \ll (64\pi k_0^3)/|k_u|^4_{max}$.

3.3 Noise statistics

The moving target echo is contaminated by the system noise and by the background echo. In order to formulate the moving target detection and estimation problems we are addressing, we need to determine the statistics of both noises.

In appendix B.1 we show that if the number of background scatterers per resolution cell is large, none is predominant, they are mutually independent, and each one has phase independent of its amplitude, then the random field $w(k_u, t)$ is zero-mean complex Gaussian circular. Assuming that backscattering coefficient σ° is constant

within the target area, then the covariance of $w(k_u, t)$ at time t, $C_w(k_{u1}, k_{u2}) \equiv E\left[s_c(k_{u1}, t)s_c^*(k_{u2}, t)\right]$, satisfies

$$C_w(k_{u_1}, k_{u_2}) = \begin{cases} \beta|A(k_{u_1})|^2 & k_{u_1} = k_{u_2} \\ 0 & k_{u_1} - k_{u_2} = 2l\pi/L, \end{cases} \tag{3.3.1}$$

where l is an integer, $\beta \equiv \sigma^\circ L E_{R_p}$, L is the target area cross-range length, and E_{R_p} is the energy of the autocorrelation of the transmitted pulse.

In deriving (3.3.1) we have assumed that the background targets have constant velocity and do not display internal motion, such as leaves moving in the wind, or waves in water bodies. We should say however that if there are internal motion in the SAR scene, the best approach to determine the covariance $C_w(k_{u_1}, k_{u_2})$ is, probably, to estimate it directly from data, for it depends on the internal motion statistics, which are normally unknown.

Concerning the system noise $n(t, u)$, we assume that it is zero-mean complex Gaussian circular and white. The SAR receiver filters $n(t, u)$ with the fast-time compression filter $P^*(\omega)$; since the system samples the cross-range domain with the sampling frequency k_s, we will consider the noise ideally lowpass filtered at $k_s/2$ in $n(t, u)$, with respect to slow-time u.

A reasoning similar to that of Appendix B leads to the conclusion that

$$C_n(k_{u_1}, k_{u_2}) = \begin{cases} \gamma, & k_{u_1} = k_{u_2} \\ 0, & k_{u_1} - k_{u_2} = 2l\pi/L. \end{cases} \tag{3.3.2}$$

where l is an integer and $\gamma \equiv \sigma^n L E_p$, with σ^n being the noise spectral power and E_p the energy of $p(t)$.

Under the assumption of constant reflectivity σ° along the cross-range dimension,

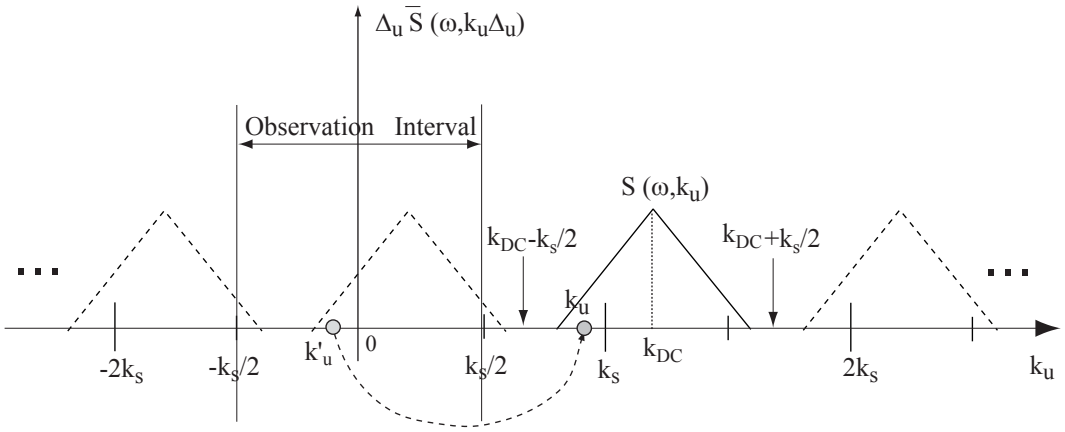

Figure 3.1: Illustration of the relation between the discrete Fourier transform of $s(\omega, n\Delta_u)$ with respect to n, $\overline{S}(\omega, k_u\Delta_u)$, and the Fourier transform of $s(\omega, u)$ with respect to u, $S(\omega, k_u)$.

the background noise plus the system noise satisfies

$$C_w(k_{u_1}, k_{u_2}) \approx \begin{cases} \beta|A(k_{u_1})|^2 + \gamma, & k_{u_1} = k_{u_2} \\ 0, & k_{u_1} - k_{u_2} = 2l\pi/L. \end{cases} \tag{3.3.3}$$

3.4 Cross-range Sampling

From (2.2.3) and (2.2.11), and noting that the aperture radiated field is confined to $|\theta| \leq \theta_M \ll 1$ and $|\phi| \ll 1$, we conclude that the support of $s_{mc}(t, k_u)$ with respect to k_u is $k_u \in [-2\nu k\theta_M + k_{DC}, 2\nu k\theta_M + k_{DC}]$, where $k_{DC} = 2k\mu_s$ is the Doppler centroid as defined in (2.2.12). The antenna beamwidth $2\theta_M$ depends on the aperture illumination. Using the indicative value $\theta_M = \lambda/(2D_y)$ (D_y denotes the cross-range aperture width), we have $k_u \in [-2\nu\pi/D_y + k_{DC}, 2\nu\pi/D_y + k_{DC}]$. The bandwidth of $s_{mc}(u, t)$ with respect to u is therefore $4\pi\nu/D_y$. As the SAR system is sampled with respect to the cross-range, then, according to the Nyquist theorem, the cross-range sampling interval must satisfy $\Delta_u \leq D_y/(2\nu)$.

Let $\bar{S}(\omega,\Omega)$ be the discrete Fourier Transform of sequence $s(\omega,n\Delta_u)$ with respect to the integer variable n. The function $\Delta_u\bar{S}(\omega,k_u\Delta u)$ is a periodic extension of $S(\omega,k_u)$ of period $k_s\equiv 2\pi/\Delta_u$. Since the sampling frequency k_s is above the Nyquist rate, the successive replicas of $S(\omega,k_u)$ do not overlap. This is illustrated in Fig. (3.1), which shows spectra $\Delta_u\bar{S}(\omega,k_u\Delta u)$ and $S(\omega,k_u)$.

To obtain the compressed moving target echo (3.2.6) we should then compute

$$s_c(t,k_u)\equiv\mathcal{F}^{-1}_{(\omega)}\left[\Delta_u\bar{S}(\omega,k_u\Delta_u)P^*(\omega)e^{j\psi'(\omega,k_u)}\right], \tag{3.4.1}$$

for $k_u\in[k_{DC}-k_s/2,k_{DC}+k_s/2[$. In practice, the discrete Fourier transform $\bar{S}(\omega,\Omega)$ is computed by the fast Fourier transform (FFT) algorithm at a set of equispaced discrete frequencies $k_u\in[-k_s/2,k_s/2[$ (observation interval in Fig. (3.1)). These frequencies should be mapped onto the interval $[k_{DC}-k_s/2,k_{DC}+k_s/2[$, as it is indicated by an arrow in Fig. (3.1) linking k'_s to k_s. Note that, for a given Doppler centroid k_{DC}, the couple (k_u,k'_u) is unique and satisfies

$$k_u=qk_s+k'_u,\qquad k_u\in[k_{DC}-k_s/2,k_{DC}+k_s/2[, \tag{3.4.2}$$

where q is an integer. The Doppler centroid dependent mapping (3.4.2) between k_u and k'_u plays an important role in the algorithms presented in the next section.

3.5 Detection/Estimation Problem

Suppose that we have identified a pair (X',α') such that the quadratic phase term in expression (3.2.8) is neglegible in comparison with the fast-time range resolution. In this case, the signal $s_{mc}(t,k_u)$ has been straightened along $\tau=(2/c)(X-X')$. Furthermore, assuming that we measure τ, then the motion transformed coordinate

X and the relative speed α are approximately given by $X \simeq X' + (c/2)\tau$ and $\alpha \simeq \alpha'\sqrt{X/X'}$.

Define

$$\begin{aligned} \mathbf{s} &\equiv [s_{-N}, \ldots, s_0, \ldots, s_{N-1}]^T \\ \mathbf{a} &\equiv [a_{-N}, \ldots a_0, \ldots, a_{N-1}]^T, \end{aligned} \tag{3.5.1}$$

where

$$\begin{aligned} s_i &= s_c(\tau, k_{u_i}) e^{j\frac{k_{u_i}^2}{4k_0}\frac{X'}{\alpha'^2}} \\ a_i &= A(k_{u_i}) e^{j\frac{k_{u_i}^2}{4k_0}\frac{X}{\alpha^2}} e^{-j\frac{k_{u_i}Y}{\alpha}}, \end{aligned}$$

with $k_{u_i} = k_{u_0} + (2\pi i)/L$ for $i = -N, \ldots, 0, \ldots, N-1$, $N = \lceil Lk_s/(4\pi) \rceil$ ($\lceil x \rceil$ denotes the smallest integer larger than or equal to x), and k_{u_0} the multiple of $(2\pi)/L$ closest to k_{DC}. Since the fast Fourier transform (FFT) is used to compute the discrete time Fourier transform, then using $2N$ points in the k_u domain implies using $2N$ points in the u domain to sample the cross-range length L . Therefore, with this setting, the cross-range sampling interval is $\Delta_u = L/(2N) \leq (2\pi)/k_s$, thus satisfying the Nyquist limit.

For a given moving target parameters vector $\theta \equiv (\mu, \nu, X, Y)$ and reflectivity f_m, the density of vector $\mathbf{s}$ is

$$p(\mathbf{s}|f, \theta) = \mathcal{N}(\mu_s, \mathbf{C}_s), \tag{3.5.2}$$

where the mean $\mu_s \equiv E[\mathbf{s}]$ and the covariance $\mathbf{C}_s \equiv E[(\mathbf{s}-\mu_s)(\mathbf{s}-\mu_s)^H]$ are, according to (3.2.7) and (3.3.3) and assuming that $R_p(0) = 1$, given by

$$\begin{aligned} \mu_s &= f_m \mathbf{a}(\theta) \\ \mathbf{C}_s &= \text{diag}\left(\beta|\widetilde{A}_0(k_{u_i})|^2 + \gamma\right), \quad i = -N, \cdots, N-1, \end{aligned}$$

where the operator $\widetilde{h}(k_u)$ denotes a k_s-periodic extension of $h(k_u)$.

The problem at hand is a binary test: under the hypothesis $\mathcal{H}_0$, the received signal is the background echo; under the alternative hypothesis $\mathcal{H}_1$, the received signal is the background echo plus the moving target echo, i.e.,

$$\begin{aligned} \mathcal{H}_0 : &\quad \mathbf{s} = \mathbf{w} \\ \mathcal{H}_1 : &\quad \mathbf{s} = f_m \mathbf{a}(\theta) + \mathbf{w}, \end{aligned} \tag{3.5.3}$$

where $\mathbf{w} \equiv [w_{-N} \cdots w_0 \cdots w_{N-1}]^T$, with $w_i \equiv \widetilde{w}(k_{u_i}, \tau)$, for $i = -N, ..., 0, ..., N-1$.

We adopt the *generalized likelihood ratio test* (GLRT) [35] to our detection problem, which, in the present case, amounts to computing the test

$$l(\mathbf{s}) \underset{\mathcal{H}_0}{\overset{\mathcal{H}_1}{\gtrless}} \eta, \tag{3.5.4}$$

with η being the detection threshold and

$$l(\mathbf{s}) \equiv \ln \left\{ \frac{p(\mathbf{s}|\widehat{f}_m, \widehat{\theta})}{p(\mathbf{s}|f_m = 0)} \right\}, \tag{3.5.5}$$

where the maximum likelihood estimates $(\widehat{f}_m, \widehat{\theta})$ are given by

$$(\widehat{f}_m, \widehat{\theta}) = \arg \max_{f_m, \theta} \left\{ -[\mathbf{s} - f_m \mathbf{a}(\theta))]^H \mathbf{C}_s^{-1} [\mathbf{s} - f_m \mathbf{a}(\theta)] \right\}, \tag{3.5.6}$$

and $p(\mathbf{s}|f_m = 0)$ is the density of noise $\mathbf{w}$.

To compact the notation, we introduce the inner product $\langle \mathbf{x}, \mathbf{y} \rangle \equiv \sum_{i=-N}^{N-1} x_i c_i^{-1} y_i^*$ and the induced norm $\|\mathbf{x}\|^2 \equiv \langle \mathbf{x}, \mathbf{x} \rangle$, where $\mathbf{x}, \mathbf{y} \in C^{2N}$ (C denotes the complex set) and $c_i \equiv [\mathbf{C}_s]_{ii}$.

Noting that the distance $\|\mathbf{s} - f_m \mathbf{a}\|$ is minimized when $\langle \mathbf{s} - f_m \mathbf{a}, \mathbf{a} \rangle = 0$ (i.e., the

error $\mathbf{s} - f_m\mathbf{a}$ is orthogonal to $\mathbf{a}$) and after some algebra we obtain

$$\widehat{f}_m = \frac{\langle \mathbf{s}, \widehat{\mathbf{a}} \rangle}{\|\widehat{\mathbf{a}}\|^2} \tag{3.5.7}$$

$$\widehat{\theta} = \arg\max_{\theta} \left\{ \frac{|\langle \mathbf{s}, \mathbf{a}(\theta) \rangle|^2}{\|\mathbf{a}(\theta)\|^2} \right\} \tag{3.5.8}$$

$$l(\mathbf{s}) = \frac{|\langle \mathbf{s}, \widehat{\mathbf{a}} \rangle|^2}{\|\widehat{\mathbf{a}}\|^2}, \tag{3.5.9}$$

where $\widehat{\mathbf{a}} \equiv \mathbf{a}(\widehat{\theta})$.

Since $\langle \mathbf{s}, \mathbf{a} \rangle = \|\mathbf{a}\| \, \|\mathbf{s}\| \cos \alpha_{\mathbf{as}}$, where $\alpha_{\mathbf{as}}$ is the angle between vectors $\mathbf{a}$ and $\mathbf{s}$, the maximum likelihood estimator of θ seeks the estimate $\widehat{\mathbf{a}}$ with highest angular proximity to observed data $\mathbf{s}$. Moreover, the inner products present in (3.5.8) implements noise plus clutter suppression by attenuating vectors $\mathbf{a}(\theta)$ and $\mathbf{s}$ proportionally to noise plus clutter power $\beta |\widetilde{A}_0(k_{u_i})|^2 + \gamma$.

We adopt the Neyman-Pearson approach to signal detection. Therefore, the threshold η that maximizes the *probability of detection* $P_D = \{\mathbf{s} : l(\mathbf{s}) > \eta \,|\, \mathcal{H}_1\}$ is found from the *false alarm probability* $P_{FA} = \{\mathbf{s} : l(\mathbf{s}) > \eta \,|\, \mathcal{H}_0\}$. Explicit expressions for densities $p(l|\mathcal{H}_0)$ and $p(l|\mathcal{H}_1)$ are not available because $\widehat{\mathbf{a}}$ is an unknown nonlinear function of random vector $\mathbf{s}$. In order to obtain approximate values of η and to derive bounds for the detector performance, we assume for a while that the detector has perfect knowledge of the parameter $\mathbf{a}$ (this is the so-called *clairvoyant detector* [35]). In this case, the probability of $\langle \mathbf{s}, \mathbf{a} \rangle$ is $\mathcal{N}(0, \|\mathbf{a}\|^2)$ under hypothesis H_0 and $\mathcal{N}(f_m \|\mathbf{a}\|^2, \|\mathbf{a}\|^2)$ under hypothesis H_1. Thus, the density of $2l$ is

$$2l \sim \begin{cases} \chi^2_2 & \text{under } \mathcal{H}_0 \\ \chi'^2_2(|f_m|^2 \|\mathbf{a}\|^2) & \text{under } \mathcal{H}_1, \end{cases}$$

where χ^2_2 denotes the *chi-squared* density with 2 degrees of freedom and $\chi'^2_2(\lambda)$ denotes the *noncentral chi-squared* density with 2 degrees of freedom and noncentrality

parameter λ. Since density χ^2_2 is the exponential density of mean 2, the threshold η is then given by

$$\eta = -\ln P_{FA}.$$

The detector performance depends only on the noncentrality parameter

$$\begin{aligned} |f_m|^2\|\mathbf{a}\|^2 &= \sum_{i=-N}^{N-1} \frac{|f_m|^2 E_p^2 |A(k_{u_i})|^2}{\beta|\widetilde{A}_0(k_{u_i})|^2 + \gamma} \\ &\simeq \frac{1}{2\pi}\int_{\frac{-k_s}{2}}^{\frac{-k_s}{2}} \frac{|f_m|^2 E_p^2 |\widetilde{A}(k_u)|^2}{\sigma^0 E_{R_p}|\widetilde{A}_0(k_u)|^2 + \sigma^n E_p}\, dk_u. \end{aligned} \tag{3.5.10}$$

The expression on the right hand side of (3.5.10) is the best signal to clutter plus noise ratio (SCNR_{opt}) that it is possible to attain, which is achieved by compressing the signal plus clutter noise signature (3.2.7) with the matched filter $A^\star(k_u)/(\sigma^0 E_{R_p}|\widetilde{A}_0(k_u)|^2 + \sigma^n E_p)$ (see, e.g., [29] for the derivation of the matched filter).

For a given backscattering coefficient σ^0 and noise spectral power σ^n, the SCNR_{opt} depends on the antenna radiation pattern $A(k_u)$ through the relative velocities μ and ν. Assuming a large clutter to noise ratio (CNR), then the function $1/(\sigma^0 E_{R_p}|\widetilde{A}_0(k_u)|^2 + \sigma^n E_p)$ exhibits a high-pass shape with cut-band roughly corresponding to the support of $A_0(k_u)$. Therefore, the lowest values of SCNR_{opt} correspond to antenna radiation patterns $A(k_u)$ whose support are totally contained in the support of $A_0(k_u)$. If the support of $A(k_u)$ becomes a little displaced with respect to the support of $A_0(k_u)$, then part of $A(k_u)$ is amplified by the high-pass filter and the SCNR_{opt} becomes large, thus increasing the probability of detection. As a conclusion, the targets most hard to detect are those with cross-range velocity parallel to the platform motion (i.e., $\nu \leq 1$) and slant-range relative velocities multiple of $k_s/(2k_0)$. These conclusions reinforce the results from Chapter 2, where the analysis of the Fisher Information matrix elements of the velocity components gave us similar outcomes.

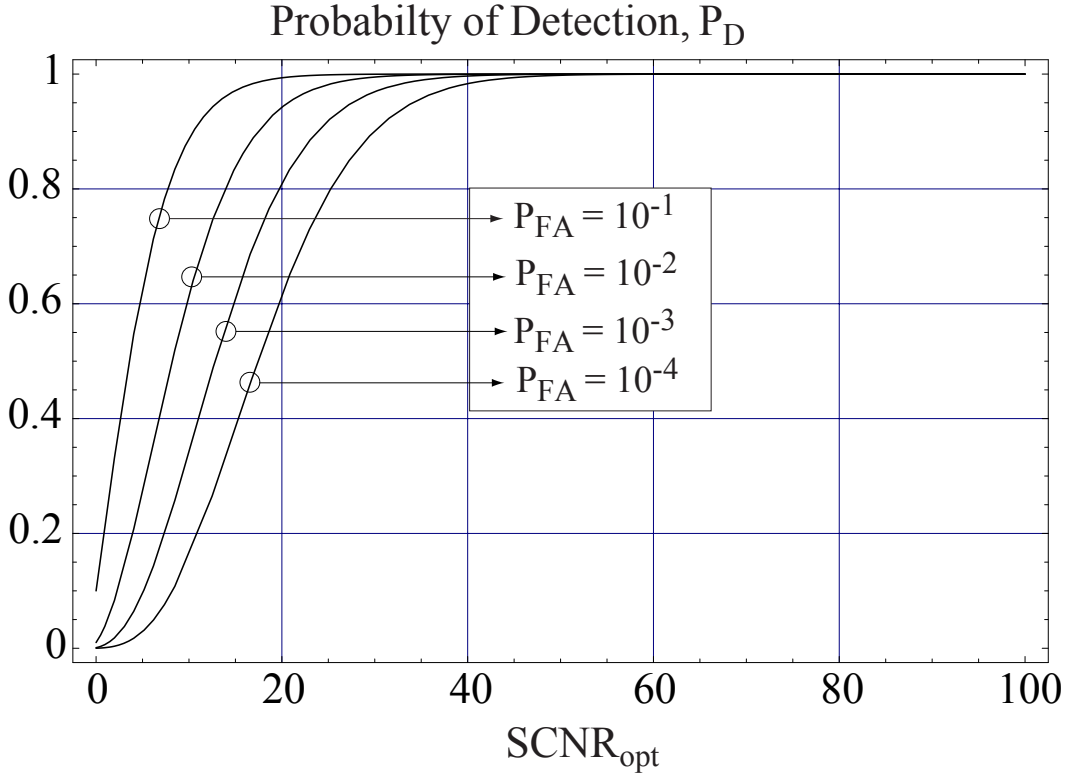

Figure 3.2: Detection performance of the Neyman-Pearson detector, assuming perfect knowledge of the moving target parameters.

Fig. 3.2 plots the detection performance of the Neyman-Pearson detector, assuming perfect knowledge of the moving target parameters (μ, ν, X, Y). As an indication of the detector performance, we have $P_D > 0.8$ for $\text{SCNR}_{opt} \gtrsim 10$ and $P_{F_A} = 10^{-2}$. The detection probability of the realizable detector is, of course, below the bounds plotted in Fig. 3.2.

According to the rationale just presented, the SCNR_{opt} is the most important figure concerning detection performance in SAR. Nevertheless, most authors when referring to SCNR do not have SCNR_{opt} in mind. This is a source of confusion, as the SCNR depends on the compression filter. In this paper and for comparison purposes, when referring to SCNR, we are assuming a flat compression filter. We then have

$$\text{SCNR} \simeq \frac{1}{2\pi} \frac{\left| f_m E_p \int_{\frac{-k_s}{2}}^{\frac{-k_s}{2}} \widetilde{A}(k_u)\, dk_u \right|^2}{\int_{\frac{-k_s}{2}}^{\frac{-k_s}{2}} \left(\sigma^0 E_{R_p} |\widetilde{A}_0(k_u)|^2 + \sigma^n E_p \right) dk_u}. \tag{3.5.11}$$

The SCNR, as given by (3.5.11), does not depend on the slant-range relative velocity μ. The same is not true concerning SCNR_{opt}, as we have discussed above: assuming a high CNR, even a small μ leads to a high SCNR_{opt}.

3.6 Moving Target Parameters Estimation Algorithm

Computing the maximum likelihood estimate (3.5.8) amounts to a multidimensional nonlinear optimization of the unknown parameters $(\mu, \nu, X, Y) \in \mathbb{R}^4$, with unbearable computational burden. Herein, instead of computing the exact maximizer of $l(\mathbf{s}, \theta) \equiv |\langle \mathbf{s}, \mathbf{a}(\theta) \rangle|^2 / \|\mathbf{a}(\theta)\|^2$, we adopt a suboptimal approach that iteratively maximizes $l(\mathbf{s}, \theta)$

on given subsets of $\mathbb{R}^4$. First we assume that there are available rough estimates of X, α, and k_{DC}; the first two allows to get vector $\mathbf{s}$ from the compressed signal $s_c(t, k_u)$ and the former assures that the support of $S_m(\omega, k_u)$, with respect to k_u, is contained in $[\widehat{k}_{DC} - k_s/2, \widehat{k}_{DC} + k_s/2[$. Latter on this section, we present a scheme to derive this estimates.

Let us denote

$$l(\mathbf{s}, \mu, \nu) \equiv \arg\max_{Y} l(\mathbf{s}, \mu, \nu, Y). \tag{3.6.1}$$

Parameter X has been omitted as we are assuming that it is known. The dependency of $l(\mathbf{s}, \theta)$ on Y is only through the term $|\langle \mathbf{a}, \mathbf{s} \rangle|$, which can be expanded as

$$|\langle \mathbf{a}, \mathbf{s} \rangle| \quad = \quad \left| \sum_{i=-N}^{N-1} b_i e^{-j\Omega i} \right|. \tag{3.6.2}$$

where $b_i \equiv A(k_{u_i}) e^{jk_{u_i}^2/\alpha^2} c_i^{-1} s_i^*$ and $\Omega \equiv 2\pi Y/(L\alpha)$. Notice that, by using the FFT, $|\langle \mathbf{a}, \mathbf{s} \rangle|$ can be computed efficiently at $\Omega_i = (\pi/N)i$, for $i = -N \ldots, 0, \ldots, N-1$. The frequency $\widehat{\Omega} = \Omega_i$ corresponding to the maximum of $|\langle \mathbf{a}, \mathbf{s} \rangle|$ leads $\widehat{Y} = \alpha L \widehat{\Omega}/(2\pi)$. The absolute error of $\widehat{Y}$ due to the discrete nature of the FFT is $\alpha L/(4N) \simeq \alpha \Delta_u/2$.

Algorithm 1 DetectMultipleTargets$[S(\omega, k_u), \bar{x}, k_0]$

Initialization: $\eta := -log(P_{F_A})$

1: **repeat**
2: $(\widehat{\alpha}, \widehat{k}_{DC}, \widehat{X}, l) :=$ **SearchStrongestTarget**$[s(\omega, k_u)]$
3: **if** $l >= \eta$ **then** {found another candidate}
4: $(\widehat{\mu}, \widehat{\nu}, \widehat{Y}) :=$ **GetParameters**$\mu\nu Y(\widehat{\alpha}, \widehat{k}_{DC}, \widehat{X})$ {get its parameters}
5: $f(t, u) := \mathcal{F}^{-1}_{(k_u)}[s_c(t, k_u, \widehat{\alpha}, \widehat{k}_{DC})]$ {focus it}
6: $f(t, u) := f(t, u)\,\mathrm{mask}\,(\widehat{X}, \widehat{Y})$ {delete it for new iteration}
7: $s(\omega, k_u) = \mathcal{F}_{(t,u)}[f(t, u)]$
8: **end if**
9: **until** $l < \eta$

The proposed algorithm to detect and estimate the moving target parameters is now explained. The main procedure is presented in Algorithm 1 (**DetectMultipleTargets**). The procedure searches, for each iteration, for the strongest target in the target area. This is achieved with procedure presented in Algorithm 2 (**SearchStrongestTarget**) which, besides returning the estimated value of the objective function for that target, also provides the aforementioned rough estimates of parameters α, k_{DC} and X. If the evaluation of the objective function for that target exceeds a predetermined threshold η, then we estimate its parameters using the procedure described in Algorithm 3 (**GetParameters**$\mu\nu Y$). Before proceeding to the next target, and to avoid false alarms, the already processed target is removed from the target area. Step 5 and Step 6 of Algorithm 1 implements this procedure. Step 5 focus the moving target at coordinates $(\widehat{X}, \widehat{Y})$. Step 6 removes the moving target by multiplying the focused image $f(u,t)$ with a mask centered at moving target coordinates $(\widehat{X}, \widehat{Y})$.

Algorithm samples the vector (α, k_{DC}, X) to maximize the objective function. For each compressed image $s_c(k_u, t)$, computed for $t_n = (2/c)(X(n) - X_c)$ with the FFT algorithm, we compute the likelilihood ratio test $l(\mathbf{s}, 0, \alpha(i))$ for each column $s = s_c(:, t_n)$ assuming an omnidirectional antenna. If we had not assumed an omnidirectional antenna in Algorithm **SearchStrongestTarget**, the search would have to be done on the parameters (μ, ν, X, k_{DC}), leading to a higher complexity. Step 17 corrects the estimate of α using the fact that $X/\alpha^2 \simeq X'/\alpha'^2$, when the moving target signature has been straightened.

Algorithm **GetParameters**$\mu\nu Y$ implements the scheme we propose to estimate parameters μ, ν and Y. The rough estimates of α, k_{DC} and X were determined by

Algorithm 2 $(\widehat{\alpha}, \widehat{k}_{DC}, \widehat{X}, l) :=$ **SearchStrongestTarget**$[s(\omega, k_u), \bar{x}, k_0]$

Initialization: $\{\alpha_i\}_{i=1}^{M_\alpha}$, $\{k_{DC_i}\}_{i=1}^{M_k}$, X_c, $l(1{:}3, 1{:}M_x) = 0$

for $i = 1 : M_k$ **do** {for all Nyquist intervals}
  $\hat{k}_{DC} = k_{DC_i}$
  for $j = 1 : M_\alpha$ **do** {for all αs}
    $\hat{\alpha} = \alpha_i$
    $s_c = s_c[\hat{\alpha}, \hat{k}_{DC}, X_c]$ {comp. signature (3.2.6)}
    for $n = 1 : M_x$ **do** {for all ranges}
      $\mathbf{s} := \mathbf{s}(\hat{\alpha}, \hat{k}_{DC}, X(n))$
      $obj := l(\mathbf{s}, 0, \hat{\alpha})$ {omnidirectional antenna}
      if $obj > l(1, n)$ **then** {stronger target found?}
        $l(1, n) = obj$, $l(2, n) = \hat{\alpha}$, $l(3, n) = \hat{k}_{DC}$ {store its parameters}
      end if
    end for
  end for
end for
$n := \text{index}\,(\max(l(1, :)))$
$\widehat{X} = X(n)$
$\widehat{\alpha} := l(2, n)\sqrt{X(n)/X_c}$
$\widehat{k}_{DC} = l(3, n)$

Algorithm 3 $(\widehat{\mu}, \widehat{\nu}, \widehat{Y}, \hat{x}_0, \hat{y}_0,) :=$ **GetParameters**$\mu\nu Y[\widehat{\alpha}, \widehat{k}_{DC}, \widehat{X}, S(\omega, k_u)]$

$\mathbf{s} := \mathbf{s}(\widehat{\alpha}^{(0)}, \widehat{X}, \widehat{k}_{DC})$ {fast-time compression}
for $t := 1 : t_{max}$ **do**
  $(\mu, \nu) :=$**Get**μ**Fixed**$\alpha(\mathbf{s}, \mu, \nu)$
  $\widehat{\nu}^{(t)} :=$**Get**ν**Fixed**μ $(\mathbf{s}, \widehat{\mu}^{(t)}, \nu)$
  $\widehat{\alpha}^{(t)} := \sqrt{(\widehat{\mu}^{(t)})^2 + (\widehat{\nu}^{(t)})^2}$
end for
$\widehat{Y} = \alpha L \widehat{\Omega}/(2\pi)$
$\widehat{x}_0 = (\widehat{\nu}\widehat{X} + \widehat{\mu}\widehat{Y})/\widehat{\alpha}$
$\widehat{y}_0 = (\widehat{\nu}\widehat{Y} - \widehat{\mu}\widehat{X})/\widehat{\alpha}$ {Solve azimuth ambiguity}

Algorithm **SearchStrongestTarget**. In order to minimize the search space this algorithm uses two one-dimensional searches. In step 3, Algorithm 4 (**Get**μ**Fixed**α) is used to maximize $l(\mathbf{s}, \mu, \nu)$ over the circle $\mu^2 + \nu^2 = \left(\alpha^{(t-1)}\right)^2$. Step 4 uses Algorithm 5 (**Get**ν**Fixed**μ) to maximize $l(\mathbf{s}, \mu, \nu)$ over the line $\mu = \mu^{(t)}$.

Algorithm 4 (μ, ν) :=**Get**μ**Fixed**$\alpha[s, \alpha, k_{DC}]$.

Initialization: $\Delta\mu_{max} = k_s/(4k_0)$, $\mu_c = \widehat{k}_{DC}/(2k_0)$

1: **for** $i = -M_\mu, \ldots, M_\mu$ **do**
2: $\quad \mu(i) := \mu_c + (i/M_\mu)\Delta\mu_{max}$
3: $\quad \nu(i) := \sqrt{(\widehat{\alpha}^{(t-1)}) - \mu^2(i)}$
4: $\quad l(i) := l(\mathbf{s}, \mu(i), \nu(i))$
5: **end for**
6: $i :=$ index $(\max(l))$
7: $\widehat{\mu}^{(t)} := \mu(i)$, $\widehat{\nu}^{(t)} := \nu(i)$

Algorithm **Get**μ**Fixed**α implements step 3 of **GetParameters**$\mu\nu Y$ by means of a discrete search with $2M_\mu + 1$ equispaced points in the interval $\mu \in [\mu_c - \Delta\mu_{max}, \mu_c - \Delta\mu_{max}]$ keeping $\alpha = \widehat{\alpha}^{(t-1)}$. Velocities μ_c and $\Delta\mu_{max}$ correspond to the cross-range frequency $\widehat{k}_{DC}$ and to half of sampling frequency k_s, respectively.

Algorithm 5 $(\hat{\nu}, \hat{\Omega})$:=**Get**ν**Fixed**$\mu[s, \hat{mu}, \hat{k}_{DC}]$

Initialization: $\Delta\nu_{max}$

1: **for** $i = -M_\nu, \ldots, M_\nu$ **do**
2: $\quad \nu(i) := \widehat{\nu}^{(t)} + (i/M_\nu)\Delta\nu_{max}$
3: $\quad \alpha(i) := \sqrt{\left(\widehat{\mu}^{(t)}\right)^2 + \nu^2(i)}$
4: $\quad l(i) := l(\mathbf{s}, \widehat{\mu}(t), \nu(i))$
5: **end for**
6: $i :=$ index $(\max(l))$
7: $\widehat{\nu}^{(t)} := \nu(i)$
8: $\widehat{\Omega} = \Omega(i)$

Algorithm 5 (**Get**ν**Fixed**μ) implements the step 4 of **GetParameters**$\mu\nu Y$ by means of a discrete search with $2M_\nu + 1$ in the interval $\nu \in [\widehat{\nu}^{(t)} - \Delta\nu_{max}, \widehat{\nu}^{(t)} + \Delta\nu_{max}]$

Table 3.1: Mission parameters used in simulation.

Parameter	Value
Carrier frequency	2.5 GHz
Chirp bandwidth	50 MHz
Swath central slant-range	10 km
Platform velocity	600 km/h
Antenna azimuthal length	4 m
Antenna radiation pattern	Raised cosine
Cross-range sampling interval	1 m
Cross-range resolution	2 m
Slant-range sampling interval	1.5 m
Slant-range resolution	3 m

keeping $\mu = \widehat{\mu}^{(t)}$.

We have implemented the unidimensional discrete searches of Algorithms **Get**μ**Fixed**α and **Get**ν**Fixed**μ in a multigrid fashion using ten points per resolution level and three depth levels. This procedure work very well and speeds up by orders of magnitude the execution times of these algorithms.

3.7 Results

The methodology developed in the previous section is now applied to synthetic and real data. The former contains point targets and an extended target, all in homogeneous background. The latter deals with real targets with simulated motion in a real background.

3.7.1 Synthetic Data

In this subsection we present results based on synthetic data aiming at the evaluation of the proposed technique. Tables 3.1 and 3.2 display the SAR mission parameters

Table 3.2: Moving target parameters. Targets 1 to 8 are point-like whereas target 9 is extended [6 m (range)× 2 m (cross-range)]. Coordinates are in meters.

	Initial coord.		Velocity		MT coord.	
Target	x_0	y_0	μ	ν	X	Y
1	-95	-80	0.00	1.0	-95.0	-80.0
2	-35	-80	0.01	1.0	-34.7	19.6
3	25	-80	0.01	0.9	25.2	31.4
4	85	-80	0.01	0.8	85.2	46.1
5	-85	80	0.00	1.2	-85.0	80
6	-25	80	0.06	1.0	-47.7	677.3
7	35	80	0.11	1.1	-22.8	1078.0
8	95	80	0.15	1.2	7.1	1331.5
9	0	0	0.01	1.0	-0.5	100

and the trajectory parameters of nine moving targets, respectively. Targets 1 to 8 are point-like, whereas target 9 is extended having 6 m in slant-range by 2 m in cross-range. The extended target was simulated with 15 point scatterers, all with the same reflectivity except for the central scatterer, which has reflectivity 10 times higher.

Fig. 3.3 illustrates the moving target positions at $u = 0$ and their velocities. Vertical and horizontal axes represent cross-range and slant-range recentered at the central range $\bar{x} = 10$ km, respectively. The velocity direction of each target is represented by the respective arrow direction, while the velocity magnitude is written close to the respective arrow in km/h. The target area is rectangular centered at $(X, Y) = (\bar{x}, 0)$ and with cross-range and slant-range lengths of 512 m and 384 m, respectively. The shadowed area represents the antenna footprint at $u = 0$, whose synthetic array length is 256 m, for the parameters given in Table 5.1.

The antenna radiation pattern is $A_0(k_u) = 1 + \cos(2\pi k_u)$ for $|k_u| \leq \pi/2$ and $A_0(k_u) = 0$ for $|k_u| > \pi/2$. Since the cross-range sampling interval is 1 m, the sampling frequency is $k_s = 2\pi$ and thus $k_s = 2\pi$, i.e., the bandwidth of a static target is half

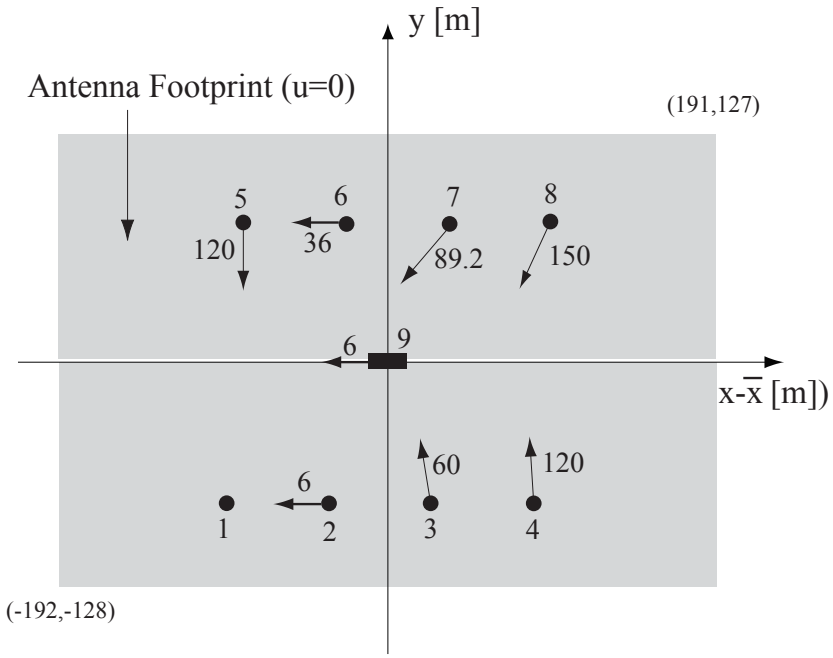

Figure 3.3: Illustration of the moving target positions at $u = 0$ and their velocities. Vertical and horizontal axes represent cross-range and slant-range recentered at the central range $\bar{x} = 10000\,\mathrm{m}$, respectively. The velocity direction of each target is represented by the respective arrow direction, while the velocity magnitude is written close to the respective arrow in km/h.

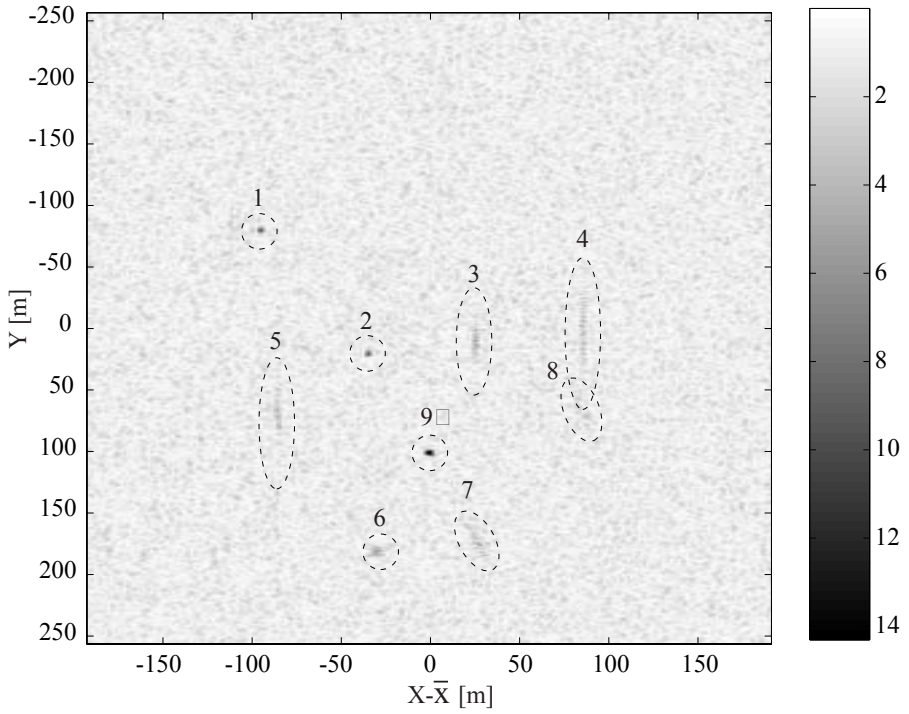

Figure 3.4: Imaging of the target area focused with relative speed $\alpha = 1.0$ and Doppler centroid $k_{DC} = 0$. The signal to clutter ratio (SCR) and the clutter to noise ratio (CNR) are both 20 dB. Targets 1, 2, and 9 are focused. All other targets are defocused as their relative speeds or Doppler centroids are different from that used by the imaging algorithm. For displaying purposes, the cross-range motion transformed coordinates of targets 6 , 7, and 8 have been wrapped into the interval $[-256, 256]$ m.

the sampling frequency k_s.

Fig. 3.4 displays the target area image focused for targets with relative speed $\alpha = 1.0$ and Doppler centroid $k_{DC} = 0$. The signal to clutter ratio (SCR) and the clutter to noise ratio (CNR) are both 20 dB. Targets 1, 2, and 9 are focused. All other targets are defocused as their relative speeds or Doppler centroids are different from those used by the imaging algorithm. The cross-range coordinate at which the defocused targets are displayed exhibits errors with respect to those shown in Table 3.2. These errors increase with the error in the Doppler centroid. For displaying

purposes, the cross-range motion transformed coordinates of targets 6 , 7, and 8 have been wrapped into the interval $[-256, 256]$ m.

Fig. 3.5a displays the compressed signal in the $(t = 2X/c, k_u)$ domain given by (3.2.6), corresponding to the target area shown in Fig. 3.4 and using the moving target parameters $\alpha' = 1.0$, $X' = \bar{x}$, and $K'_{DC} = 0$. SCR and CNR are both 20 dB, as in Fig. 3.4. For better perception, Fig. 3.5b shows the moving target signatures without ground clutter and system noise. For displaying purposes, the slow-time Doppler frequency coordinates of targets 6, 7, and 8 have been wrapped into the interval $[-\pi, \pi]$ rad/m.

We see from Fig. 3.5 that only targets 6, 7, and 8 produce off-vertical aligned signatures. This was to be expected as $\tau(k_u)$ given by (3.2.8) is proportional to k_u^2 and targets 6, 7, and 8 have the larger Doppler centroids among all targets.

Fig. 3.6 shows the likelihood ratio test computed by Algorithm 2. For illustration purposes, an omnidirectional antenna was assumed. In fact, if the true antenna has been used $A_0(\omega, k_u)$, then the stronger signatures would have totally masked the weaker ones. The algorithm was parameterized with $M_\alpha = 30$, $\alpha_1 = 0.7$, $\alpha_{M_\alpha} = 1.3$, $M_k = 24$, $k_{DC_1} = -3$, and $k_{DC_{M_k}} = 3$, leading to sampling intervals of the relative velocity and of the Doppler centroid of 0.02 and 0.25, respectively. All moving targets originated spikes at correct moving target slant-range coordinates. Notice, however, the presence of two spurious spikes at slant-ranges -17 and -6. These spikes do not produce false alarms because Algorithm 1 selects only the moving target with the highest likelihood ratio in each iteration. It is worth noting that targets 1, 5, and 8, although not discernible among the ground clutter in Fig. 3.5, yield a large likelihood ratio, as we can read from Fig. 3.6.

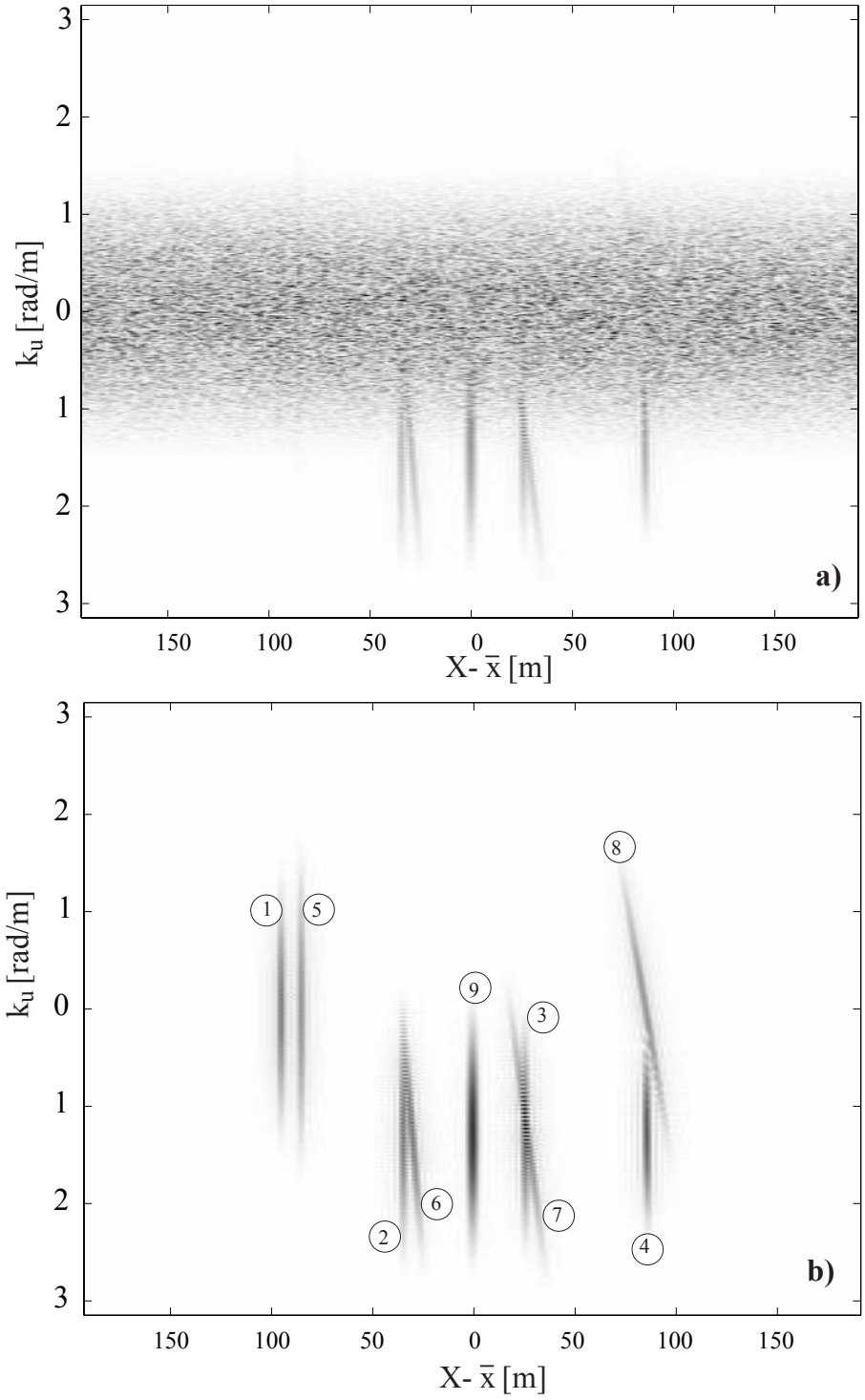

Figure 3.5: Compressed signal in the (X, k_u) domain given by (3.2.6), corresponding the target area shown in Fig. (3.4) and using the moving target parameters $\alpha' = 1.0$, $X' = \bar{x}$, and $K'_{DC} = 0$. The signal to clutter ratio and the clutter to noise ratio are SCR = 20 dB and CNR = 20 dB, respectively, as in Fig. 3.4. Part a) displays moving target signatures plus clutter noise plus system noise; part a) displays only the moving target signatures.

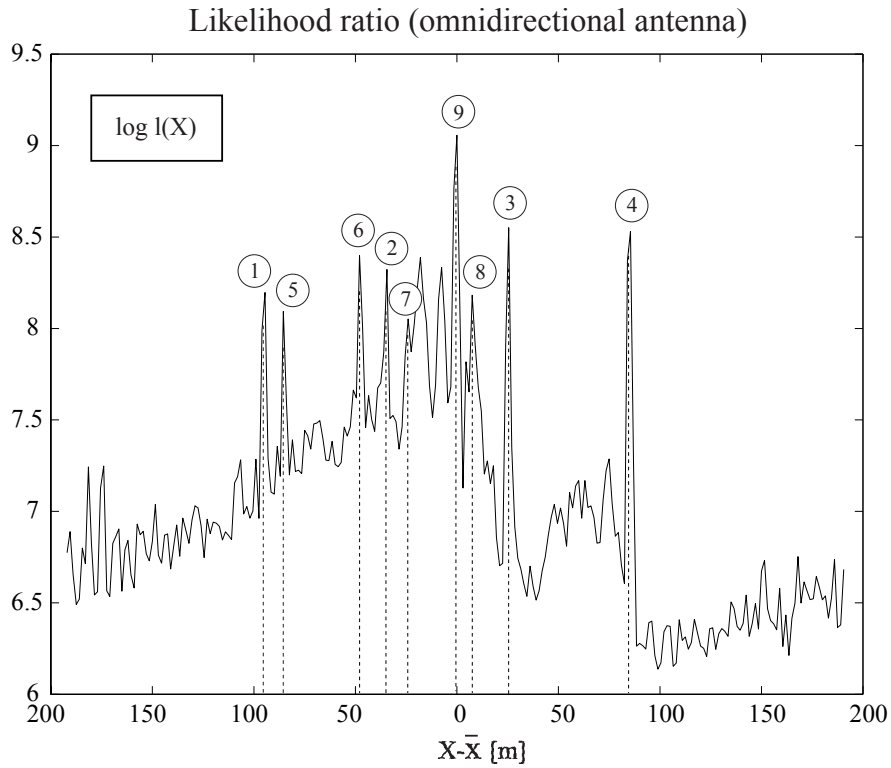

Figure 3.6: Likelihood ratio test computed by Algorithm 2. For illustration purposes we have assumed an omnidirectional antenna. All moving targets originated spikes at correct moving target slant-range coordinates. The presence of two spurious spikes at slant-ranges -17 and -6 will not produces false alarms because Algorithm 5 selects only the moving target with the highest likelihood ratio in each iteration.

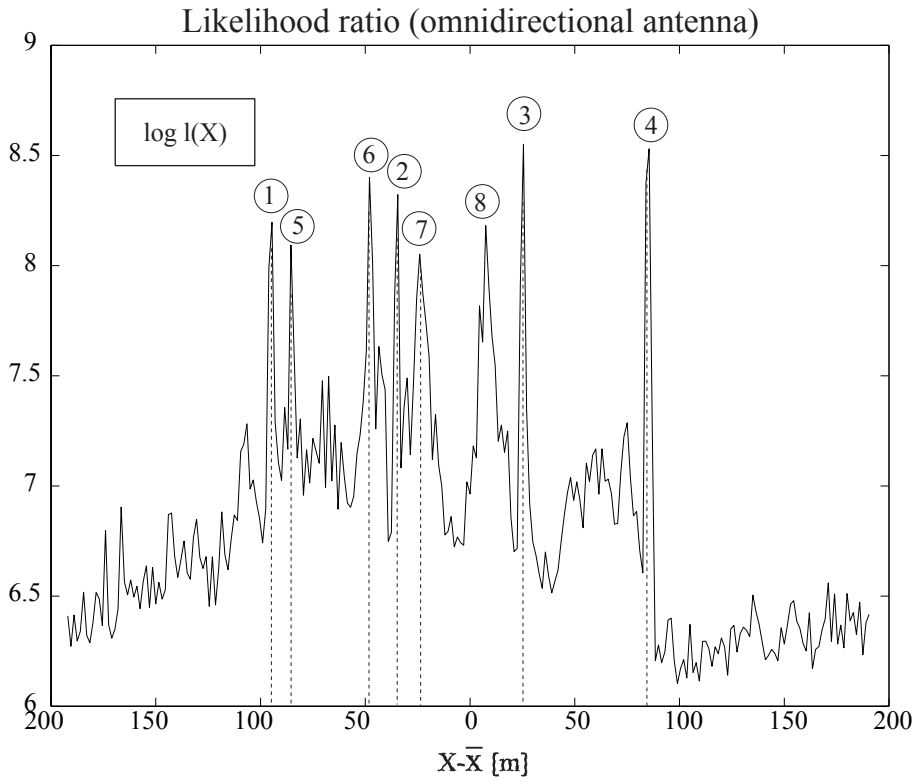

Figure 3.7: Likelihood ratio test computed by Algorithm 2, using an omnidirectional antenna, after deleting the signature of target 9 (step 6 of Algorithm 1). All the remaining targets 1 to 8 originated spikes at correct moving target slant-range coordinates. The spurious spikes present in Fig. 3.6 at slant-ranges -17 and -6 have been removed.

Table 3.3: Estimation results for SCR $= 20\,dB$ and CNR $= 20\,dB$. Coordinates are in meters.

	Initial coord.		Velocity ($\times 10^3$)		GLR
Target	$\widehat{x}_0 - x_0$	$\widehat{y}_0 - y_0$	$\widehat{\mu} - \mu$	$\widehat{\nu} - \nu$	$\log l$
1	0.5	-1.8	0.12	7.9	4.17
2	0.2	0.4	0.03	3.2	8.71
3	0.2	0.5	-0.06	3.8	8.70
4	0.3	-1.0	0.03	2.4	8.62
5	-0.5	0.4	0.03	3.2	5.08
6	-0.5	1.0	-0.09	4.1	8.68
7	-1.6	0.1	-0.02	3.5	8.70
8	0.1	-1.1	0.1	3.4	5.07
9	0.5	4.0	-0.4	4.6	9.04

Fig. 3.7 shows the likelihood ratio test computed by Algorithm 2 after deleting the signature of target 9 (step 6 of Algorithm 1). All the remaining targets 1 to 8 produced spikes at correct moving target slant-range coordinates. The spurious spikes present in Fig.3.6 at slant-ranges -17 and -6 have been removed.

Table 3.3 presents the estimation errors of parameters (x_0, y_0, μ, ν) for the nine moving targets present in the target area. Parameters t_{max}, M_μ, and M_ν of Algorithms 3, 4, and 5 were set to 2, 10, and 10, respectively. Algorithms 2 and 3 were applied in multigrid fashion using three depth levels. The last column of Table 3.3 shows, for each target, the logarithm of the likelihood ratio $\log l$. The higher values of $\log l$ correspond to targets with the higher SCNR_{opt}, or, equivalently, to targets with small spectral overlapping with the background spectrum. Using the Neyman-Pearson threshold $\eta = -\log P_F$ derived in the previous section, the upper bound for the probability of false alarm P_F allowing the detection of all moving targets is $P_F = 1.5 \times 10^{-2}$.

Roughly, the errors in x_0 and in y_0 are of the order of 0.5 m and 1 m, respectively,

Table 3.4: Estimation results for $SCR = 14\,dB$ and $CNR = 20\,dB$. Coordinates are in meters.

	Initial coord.		Velocity ($\times 10^3$)		GLR
Target	$\widehat{x}_0 - x_0$	$\widehat{y}_0 - y_0$	$\widehat{\mu} - \mu$	$\widehat{\nu} - \nu$	$\log l$
1	0.4	-1.7	0.08	10.0	3.50
2	0.2	-0.7	0.05	3.2	8.02
3	0.2	0.5	-0.06	3.8	8.00
4	0.3	-2.8	0.14	4.4	7.94
5	-0.5	0.1	0.06	3.2	4.41
6	-0.5	1.0	-0.09	4.1	8.01
7	-3.0	1.9	-0.2	3.0	8.01
8	-0.1	-4.8	0.6	3.4	4.48
9	0.5	5.1	-0.5	4.6	8.35

being lower than the slant-range and cross-range resolutions. The errors in μ and ν are of the order of 10^{-4} and 4×10^{-3}, respectively. The proposed approach yields good results even for targets with spectrum totally or almost totally superimposed on the background noise, which is the case for targets 1, 5, and 8. Extended target 9 exhibits the largest initial cross-range error. This is due to model mismatch, as we assume the targets to be point-like. Nevertheless, the estimated moving target parameters are still good for many purposes.

Table 3.4 present results similar to Table 3.2 for SCR = 14 dB and CNR = 20 dB. The estimates are similar to those presented in Table 3.3 with a little degradation mainly for targets 1 and 9. The logarithm of the likelihood ratio $\log l$, compared with the previous example, decreases by, roughly, 0.5.

Table 3.5 shows the sample root mean square error (rmse) of the moving target velocity estimates $(\widehat{x}_0, \widehat{y}_0, \widehat{\mu}, \widehat{\nu})$ as a function of the slant-range velocity μ, for $\nu = 1.2$, SCR = 10 dB, and CNR = 20 dB. Values shown were obtained from 64

Table 3.5: Sample root mean square error of $(\widehat{x}_0, \widehat{y}_0, \widehat{\mu}, \widehat{\nu},)$ as function of μ, for $\nu = 1.2$, SCR$= 10\,dB$, and CNR$= 20\,dB$.

μ	rmse$(\widehat{x}_0)$	rmse$(\widehat{y}_0)$	rmse$(\widehat{\mu})$	rmse$(\widehat{\nu})$
0.005	0.64	5.6	6.9×10^{-4}	9.4×10^{-3}
0.01	0.66	3.1	3.6×10^{-4}	4.4×10^{-3}
0.015	0.22	1.9	2.1×10^{-4}	3.7×10^{-3}
0.02	0.38	2.0	2.2×10^{-4}	3.2×10^{-3}
0.025	0.33	1.3	1.6×10^{-4}	2.9×10^{-3}

Table 3.6: Estimation results with model mismatch. Data was generated with a raised cosine shaped antenna and with SCR$= 20\,dB$ and CNR$= 20\,dB$. The estimation algorithm assumed, compared with the true values, an antenna radiation pattern 10% broader, a backscattering coefficient 10% higher, and a noise spectral power 10% lower. Coordinates are in meters.

	Initial coord.		Velocity	
Target	$\widehat{x}_0 - x_0$	$\widehat{y}_0 - y_0$	$(\widehat{\mu} - \mu)10^3$	$(\widehat{\nu} - \nu)10^3$
1	0.5	-1.0	0.05	3.8
2	0.2	-2.5	0.22	2.8
3	0.2	-2.2	0.18	3.8
4	0.3	-2.1	0.11	2.4
5	-0.5	-0.7	-0.16	3.2
6	-0.1	-1.6	0.17	2.4
7	-2.6	-1.2	0.15	2.5
8	-0.1	1.0	-0.21	-2.5
9	0.5	1.9	-0.20	4.6

Monte Carlo simulations per point. Parameter μ determines the percentage of superposition between background and moving target spectra. The selected values of $\mu = 0.005, 0.01, 0.015, 0.02, 0.05$ corresponds to spectral superpositions of $84\%, 68\%, 51\%, 36\%, 20\%$, respectively. As expected, estimates improve when the spectral superposition becomes lower. For SCR$= 0\,dB$ and CNR$= 20\,dB$ the root mean square error of $\widehat{x}_0$ is very close to the values shown in Table 3.5, whereas the root mean square error of $\widehat{y}_0$, $\widehat{\mu}$, and $\widehat{\nu}$ is higher by a factor ranging between 2 and 3.

Table 3.7: MSTAR mission parameters.

Parameter	Value
Carrier frequency	9.6 GHz
Chirp bandwidth	591 MHz
Swath central range	4.5 km
Depression angle	15°
Platform velocity	220 km/h
Cross-range sampling interval	0.203 m
Cross-range resolution	0.304 m
Slant-range sampling interval	0.202 m
Slant-range resolution	0.305 m

Often, in real applications, the antenna radiation pattern, the clutter power, and the noise power are not known exactly. To illustrate the robustness of the proposed scheme to model mismatches, we have applied the proposed estimation scheme to simulated data generated with the mission parameters shown in Table 5.1 and SCR = 20 dB and CNR = 20 dB, but using, in the estimation algorithm and compared with the true values, an antenna radiation pattern 10% broader, a backscattering coefficient 10% higher, and a noise spectral power 10% lower. Table 3.6 displays the moving target estimates obtained. In spite of model mismatches considered, the results exhibit only a little degradation, when compared with those of Table 3.3 computed in a model matched scenario.

3.7.2 Real Data

In this section, images from MSTAR data public collection (see [**?**]) collected by Sandia National Laboratory using STARLOS sensor were used. Main mission parameters are given in Table 3.7. Fig. 3.8 shows a visible (top) and two X-Band (middle and bottom) images of the BTR 60 transport vehicle. The aspect angles of the middle

and of the bottom images are nearly 0° and 90°, respectively. Fig. 3.9a shows an X-Band SAR image of ground plus six moving targets (transport vehicles BTR 60) focused with the *wavefront reconstruction algorithm* [53] (see Appendix C) parameterized for static target (i.e., $\mu = 0$ and $\alpha = 1$). The true vehicle positions, at $u = 0$, are indicated with numbered white circles. For better perception, Fig. 3.9b shows (as a negative) only the image of moving vehicles. Notice that only vehicle 1 is correctly focused and located. The remaining vehicles are blurred or wrongly located or both, as the image was focused using static target parameters, i.e., $\mu = 0$ and $\nu = 1$. The shape of the blurring depends on the moving target velocity mismatch. Target 2 is blurred along cross-range, due to a relative velocity mismatch; targets 3 and 4 are split due to a fractional Doppler centroid mismatch; finally, targets 5 and 6 are blurred in both directions, due to relative velocity and Doppler centroid mismatches.

The clutter signature in the (k_u, ω) domain was computed by reversing the wavefront reconstruction steps described in Appendix C. First, we compute expression $S(k_X, k_Y)$ [see (1.2.6)] and then interpolate this function to obtain $S_0(\omega, k_u)$ in a rectangular grid according to (1.2.7) and (1.2.8) for $\alpha = 1$. The nth moving targets signature was generated, according to (2.2.1), by computing

$$S_n(\omega, k_u) = \sum_i A_n(k_u) P_n(\omega) f_{in} e^{-j\sqrt{4k^2 - \left(\frac{k_u}{\alpha_n}\right)^2} X_{ik} + \left(\frac{k_u}{\alpha_n}\right) Y_{ik}}, \tag{3.7.1}$$

where indexes i and n denote the ith pixel of the nth moving target.

In a real scenario, the antenna radiation pattern can be measured or estimated from a point target. In the present data set, although there are strong targets, we are not sure if they are point-like. For this reason we resort to power spectrum estimation tools to determine the shape of the antenna radiation pattern $|A_0(k_u)|$, the variance $\beta|A_0(k_u)|^2 + \gamma$ of the clutter plus noise signature $w(k_u, t)$, and the pulse

Figure 3.8: Visible (top) and X-Band (middle and bottom) images of the BTR 60 transport vehicle (data from the MSTAR data public collection). Aspect angles of the middle and bottom images are nearly 0° and 90°, respectively.

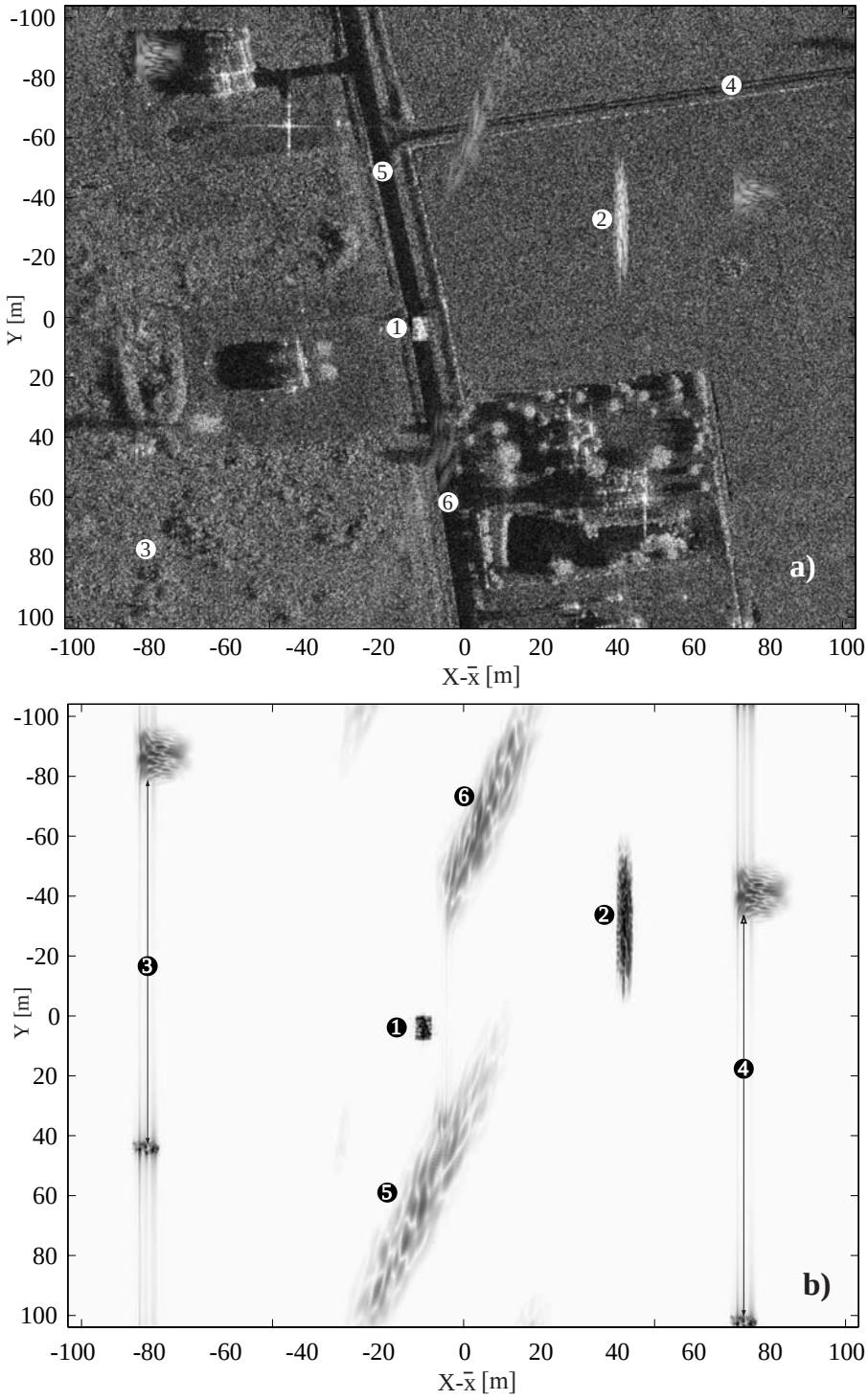

Figure 3.9: Real scene focused using parameters ($\mu = 0, \nu = 1$). Part a) shows an X-Band image containing moving targets (transport vehicles BTR 60) over ground clutter. The true vehicle positions, at $u = 0$, are indicated with numbered white circles. Part b) is the same as part a), but displays only the moving targets in negative and focused with static targets parameters (i.e., $\mu = 0$ and $\nu = 1$). Both data (moving targets and ground clutter) were built using data from the MSTAR data public collection.

$P(\omega)$. Concerning the variance $\beta|A_0(k_u)|^2 + \gamma$, an homogeneous rectangular region (north-east and south-west coordinates $(100, -60)$ and $(5, 20)$, respectively, in Fig. 3.9) was selected, then computed the sample mean of $|w(t, k_u)|^2$ along t coordinates and finally applied smoothing along k_u coordinate. The magnitude of pulse function $|P(\omega)|$ was determined using a similar procedure.

Fig. 3.10 shows the estimated magnitude of the antenna radiation pattern. Notice that the cross-range sampling frequency k_s is only marginally above the Nyquist frequency, thus placing stringent performance requirements on the moving target detector, as these target signatures will always overlap, at least partially, the clutter signature, regardless of the slant-range velocity.

In simulating the moving targets signatures, $A_0(k_u)$ has been used as antenna radiation pattern and the respective estimated magnitudes as the pulse function $P(\omega)$. One notes that, although $|A_0(k_u)|$ and $|P(\omega)|$ might be different from $A_0(k_u)$ and $P(\omega)$, this has no impact on the results, as the performance of the detection and estimation schemes proposed in the previous section depends only on the magnitudes of those functions.

Table 3.8 shows the parameters of the six vehicles moving in the target area. The SCR with respect to the strongest moving scatterer is 30dB for target 1 and 20dB for targets 2 to 6. Initial positions x_0 and y_0 are relative to the strongest moving scatter. The Doppler centroids normalized to the Nyquist frequency of targets 1-2, 3-4, 5 and 6 are 0.0, 0.5, 1.75 and -1.75, respectively.

Table 3.9 presents the estimation errors. Excepting the initial cross-range position y_0 of targets 5 and 6, all estimates are very accurate. The error of the initial position x_0 and of the motion transformed coordinates X and Y are less than 1 m; the error

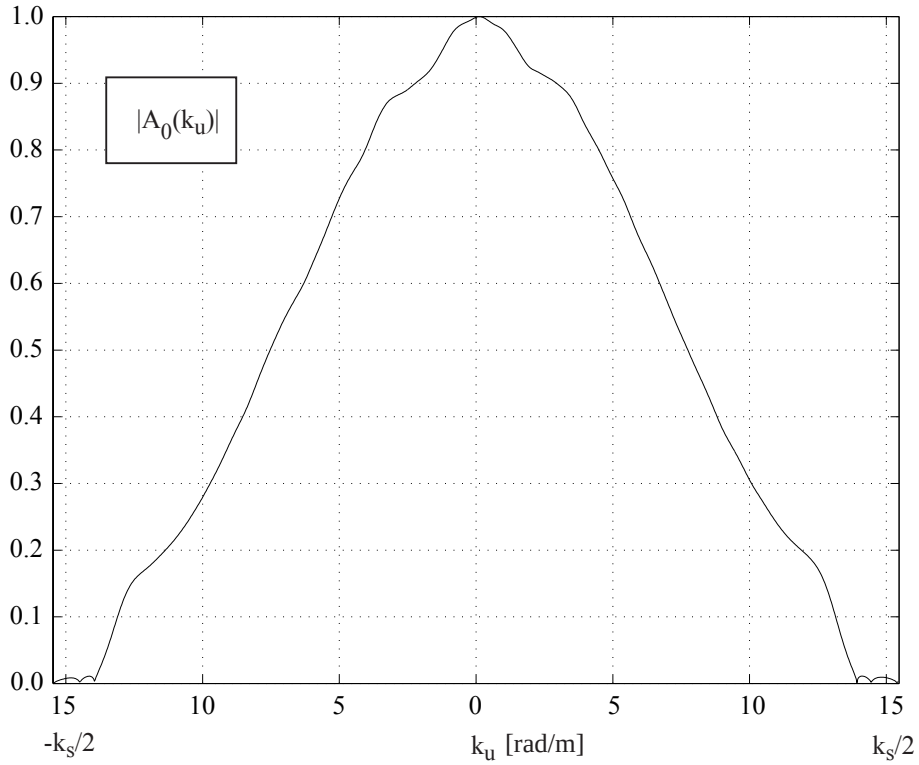

Figure 3.10: Estimated magnitude of the antenna pattern $A_0(k_u)$.

Table 3.8: Moving target parameters of the six tanks spotted in Fig. 3.9. Coordinates are in meters.

	Initial coord.		Rel. vel.		Vel. (km/h)
Target	x_0	y_0	μ	ν	$\|v\|$
1	-12.5	0	0.0	1.0	0
2	40	-40	0.0	1.1	22
3	-80	80	0.0385	1.0	8.5
4	70	-76	0.0385	1.0	8.5
5	-21	-52	0.1346	0.8	53
6	-4	65	-0.1346	1.2	53

Table 3.9: Estimation results for the six extended targets shown in Fig. 3.9. Coordinates are in meters.

	Initial coord.		MT coord.		Rel. vel. ($\times 10^2$)	
Target	$\widehat{x}_0 - x_0$	$\widehat{y}_0 - y_0$	$\widehat{X} - X$	$\widehat{Y} - Y$	$\widehat{\mu} - \mu$	$\widehat{\nu} - \nu$
1	0.00	-2.2	0.0	0.0	0.05	0.01
2	-0.18	-0.86	-0.18	0.0	0.02	0.02
3	0.00	-2.03	-0.08	-0.02	0.04	-0.004
4	0.01	-1.3	0.09	0.2	0.03	-0.073
5	-0.11	5.01	-0.01	-1.15	-0.15	0.021
6	-0.36	-8.36	0.12	1.00	-0.20	-1.00

of the slant-range velocity μ and of the cross-range velocity estimates are less 0.4% and 1%, respectively. Concerning the initial cross-range position y_0, targets 5 and 6 present the larger errors, the reason being the extended nature of the targets. In fact, a thorough inspection of the vertical tank shown in Fig. 3.8 reveals that the most predominant scatterers are very close in reflectivity and aligned along the cross-range coordinate. Theses two targets interfere generating an equivalent Doppler domain dependent reflectivity $f(k_u)$ that distorts the antenna radiation pattern $A(k_u)$, leading to errors on the relative slant-range velocity. This phenomenon is equivalent to having targets with reflectivities dependent on the aspect angle. Surprisingly, the errors induced by these model mismatches are perfectly acceptable with respect to the slant-range velocity itself, the same not being true for the initial position y_0. While we obtained errors smaller than 2 m for those targets exhibiting a clearly predominant scatterer, this was not the case with targets 5 and 6, for which we obtained errors of the initial cross-range positions of 5.01 m and -8.36 m, respectively. Recall that $\widehat{y}_0 = (\widehat{\mu}\widehat{X} + \widehat{\nu}\widehat{Y})/\widehat{\alpha}$ and that $\widehat{X} \simeq 4500$ m; therefore, to have errors less than, say, 1 m in $\widehat{y}_0$, the relative slant-range estimate $\widehat{\mu}$ must exhibit an absolute error smaller than 2.2×10^{-4}. This is not achieved for targets 5 and 6, where the errors of the relative

slant-range velocities are -1.5×10^{-3} and -2.2×10^{-3}, respectively.

3.8 Limitations of the Proposed Method

The major limitations of the proposed method are 1) the assumption of point targets and 2) independence of the antenna radiation pattern with respect to the fast-time frequency. The first is violated when the target is extended and does not have any predominant scatterer; the second is violated when the Doppler centroid k_{DC} is very large.

Concerning limitation 1), the mean $E[s_i] = fa_i$ of random variable s_i, introduced in (3.5.1), is not valid in the case of an extended target. A solution to this problem is modelling extended targets as arrays of discrete point targets, each one with reflectivity f_i and distance d_i to a reference point. The mean value of s_i would then be given by $E[s_i] = a_i \sum_n f_n e^{-j\frac{k u_i d_n}{\alpha}}$. The determination of f_i and d_i, for $i = 1, \ldots$ is a subject to be addressed in the near future. Anyway, as manmade extended targets have predominant scaterers exhibiting nearly point-like behavior, the proposed approach applies largely to these targets.

Concerning limitation 2), it can be overcome by partitioning the fast-time frequency support into small subsets and applying the proposed technique to the resulting data sets. If the accuracy of the estimates is poor, one may compute the sample mean of the moving target parameters estimates from all data sets.

3.9 Conclusions

This chapter presents a novel methodology to detect multiple moving targets in stripmap SAR and to estimate their trajectory parameters using a single sensor. By taking into account the antenna radiation pattern, the proposed algorithm determines, for each moving target (assumed to have constant velocity), not only the target location in the slant-plane, but also the two components of the velocity vector (cross-range and slant range velocities). Therefore, *the so-called azimuth position uncertainty* inherent to single sensor based systems is solved.

Whatever the domain (i.e., space, frequency, or mixed) adopted to detect the moving targets and estimate their parameters, their signatures are spread over a two-dimensional set, thus introducing complexity in any processing scheme. To reduce this complexity, a step was introduced that compresses moving target signatures along the slow-time Doppler domain for a given fast-time. Besides compressing moving targets signatures, this step yields, for each moving target candidate, the slant-range motion transformed estimate and an approximate estimate of the relative speed.

A generalized likelihood ratio test approach was then adopted to detect moving targets and derive their trajectory parameters. Determining the maximum likelihood estimate necessary to compute the generalized likelihood ratio test would amount to a multidimensional nonlinear optimization of the unknown parameters, with unbearable computational burden. Instead of computing the exact maximum likelihood estimate, a suboptimal approach was adopted that iteratively maximizes the likelihood function on given subsets of the search space. The detection threshold was set according to the Neyman-Pearson criterion. Is was found that in the ideal case of perfect knowledge of density parameters (clairvoyant detector), the detector performance depends only

on optimal signal to clutter plus noise ratio (SCNR_{opt}) obtained with the matched filter (filter matched to the signal signature immersed in clutter plus system noise). As an indication of the detector performance, for a false probability of 10^{-2} we have a detection probability greater that 0.8 for $\mathrm{SCNR}_{opt} \gtrsim 10$.

The effectiveness of the proposed method was illustrated with synthetic and real data. In the former case we simulated an S-band image with 8 point moving targets and an extended target with a predominant scatterer. For $\mathrm{SCR} = 20\,\mathrm{dB}$ and $\mathrm{CNR} = 20\,\mathrm{dB}$ we obtained estimates of the relative slant-range and cross-range velocities within an error of, approximately, 0.01% and of 0.4%, respectively. The initial position coordinates displayed errors less than the slant-range and cross-range resolutions. These values only degrade slightly for $\mathrm{SCR} = 14\,\mathrm{dB}$ and $\mathrm{CNR} = 20\,\mathrm{dB}$.

Real data results were obtained from X-Band images of the MSTAR public data collection collected by Sandia National Laboratory using STARLOS sensor. The ground clutter and moving target signatures (transport vehicles BTR 60) were obtained by resynthesizing the respective reflectivities using an inverse wavefront reconstruction algorithm. The SCR of all moving targets, measured with respect to the strongest moving scatter was less than 20dB. With the exception of the initial cross-range position, all estimates were very accurate. The errors of the initial position x_0 and of the motion transformed coordinates X and Y are less than 1 m; the error of the slant-range velocity μ and of the cross-range velocity estimates are less 0.4% and 1%, respectively. Concerning the initial cross-range positions, we obtained errors smaller than 2 m for those targets exhibiting a clearly predominant scatterer. This is was not the case for targets 5 and 6 that had two predominant targets with similar reflectivity at the same cross-range motion transformed coordinate. For this targets

the error of the initial cross-range position is 5.01 m for target 5 and -8.36 , for target 6.

The major limitations of the proposed method are the assumptions of 1) independence of the antenna radiation pattern with respect to the fast-time frequency and 2) of point-like moving targets. The first limitation can be circumvented by partitioning the fast-time frequency into small subsets and applying the proposed technique to the resulting data bases. The solution for the second limitation is modelling extended targets as arrays of discrete point targets, each one with a given reflectivity and distance to a reference point. This approach is to be exploited in future work. Anyway, as most man-made extended targets have predominant scatterers exhibiting nearly point-like behavior, the proposed approach applies generally to these targets.

Chapter 4

Trajectory Parameters Estimation Using the Signature Curvature Information

4.1 Introduction

In previous chapter we presented a technique to estimate all the moving target parameters using a single SAR sensor, thus solving the blind angle ambiguity. In this chapter we present a more efficient technique, although less accurate, to estimate the same trajectory parameters. This technique works in the (x, u) domain and does not try to straighten the moving target signature. Instead, it uses the data along the signature curvature that is dependent of the moving target trajectory parameters. Due to the fact that the methodology uses the signature curvature to estimate the velocity vector, it is able to work with moving targets inducing Doppler-shifts beyond the limit imposed by the mission PRF.

We start by writing the received signal in the (x, u) domain, after pulse compression. Then we note that the signature curvature is dependent of the trajectory

parameters, and if they are known then we can form an observation vector composed by the signature values extracted along this curvature. By assuming that this signature is immersed in white noise we derive a maximum likelihood estimator for the moving target parameters. At the end of the chapter we present results using simulated and real data to exemplify the potential of the proposed methodology.

4.2 Estimation Problem

Let us consider a moving target with slant-range and cross-range coordinates (x_0, y_0) when the platform is at position $y = 0$, and speed vector $(v_x, v_y) = (\mu_m v_R, b_m v_R)$ defined in the spatial domain (x, y); symbol v_R denotes the platform speed and (μ, b) is the target relative velocity with respect to the radar. The moving target coordinates are $(x', y' = u_0)$ when the radar platform is broadside to it as illustrated in Fig. 4.2.

When the radar is positioned at coordinate $y = u$, the corresponding received echo from a moving target, after quadrature demodulation and pulse compression, is

$$s(x, u) = a(y_0 - \nu u) p_c(x - r(u)) f_m \exp^{-j2k_0 r(u)},$$

where $a(u)$ is the two-way antenna radiation pattern (it is assumed that the dependency of $a(x, u)$ on x is negligible and that there are no pointing errors of the antenna[1]); $\nu \equiv 1 + b$, $p_c(x)$ denotes the compressed emitted pulse in the range direction, $k_0 \equiv 2\pi/\lambda_0$ is the wavenumber at wavelength λ_0, and $r(u)$ is the distance between the platform and the moving target, given by

$$r(u) = \sqrt{(x_0 - \mu u)^2 + (y_0 - \nu u)^2}. \tag{4.2.1}$$

[1]For clearness of the exposition we considered no pointing errors of the antenna. If pointing errors are present and known, they can easily be included in the proposed approach.

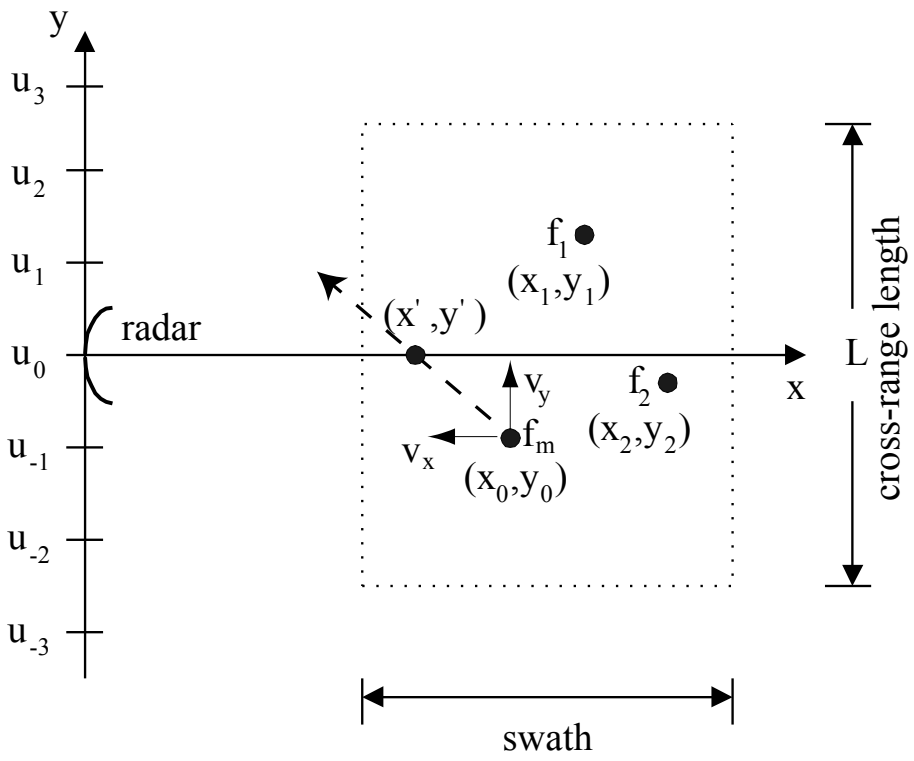

Figure 4.1: Considered SAR scenario.

Defining $u' \equiv u - u_0$, $r(u)$ can be re-written as

$$r(u') = \sqrt{(x' - \mu u')^2 + (\Delta y - \nu u')^2}, \tag{4.2.2}$$

where Δy models an error on the estimation of y'. Approximating $r(u')$ by a series expansion about $u' = 0$, and retaining only the terms through the quadratic, results

$$r(u') \approx r_0 - \underbrace{\frac{x'\mu + \nu\Delta y}{r_0} u' + \frac{(\mu_m^2 + \nu_m^2)}{2r_0} u'^2}_{\psi(u')}, \tag{4.2.3}$$

where $r_0 = \sqrt{x'^2 + \Delta y^2}$. If we could estimate $\psi(u')$, then we could form a vector using data collected at coordinates $s(x = r_0 + \psi(u'), u')$, leading to

$$s(r_0 + \psi(u'), u') = a(\Delta y - \nu u') p_c(0) f_m e^{-j2k_0 r(u')}. \tag{4.2.4}$$

Since $p_c(\zeta)$ exhibits high resolution about $\zeta = 0$ then $s(u', x)$ becomes clustered about $x = r_0 + \psi(u')$, for all u' belonging to the support of a. Therefore, the range migration curvature is known, and we can form a vector containing the signature samples echoed by the moving target.

Assume now that the received signal is immersed in white noise, $n(x, u')$, i.e., $y(x, u') = s(x, u') + n(x, u')$.

Define vectors

$$\begin{aligned} \mathbf{y} &\equiv [y_{-N}, \ldots, y', y_N]^T \\ \mathbf{s} &\equiv [s_{-N}, \ldots, s_0, s_N]^T, \end{aligned}$$

where,

$$\begin{aligned} y_i &= y(r_0 + \psi(u_i), u_i) \\ s_i &= a(\Delta y - \nu_m u_i) e^{-j2k_0 r(u_i)}, \end{aligned}$$

with $u_i = u_s i$, where u_s is the sampling space in the cross-range direction, $i = -N, \ldots, 0, \ldots, N$, and $2N+1$ is the number of samples in the cross-range direction.

Let us assume that the moving target parameters $\boldsymbol{\theta} = (\mu, \nu)$, Δy, and the reflectivity f_m are known. In this case only the noise term is random. Therefore, the density of vector $\mathbf{y}$ conditioned to $\boldsymbol{\theta}$ and f_m is

$$p(\mathbf{y}|f_m, \boldsymbol{\theta}) = \mathcal{N}(\mathbf{m_y}, \mathbf{C_y}) \tag{4.2.5}$$

where the mean $\mathbf{m_y} = f_m \mathbf{s}(\boldsymbol{\theta})$ and the covariance $\mathbf{C_y} = \sigma_n^2 \mathbf{I}$, and σ_n^2 is the noise power. Notice that $y_i = y_i(\boldsymbol{\theta})$. Consequently, the density in (4.2.5) is correct only for the true $\boldsymbol{\theta}_0$. However, for $\boldsymbol{\theta} \approx \boldsymbol{\theta}_0$, the range migration is known and the data used to form vector $\boldsymbol{s}$ is taken along the correct curvature thus leading to $y(\boldsymbol{\theta}) \approx y(\boldsymbol{\theta}_0)$. Thus, we still use (4.2.5) to derive the maximum likelihood (ML) estimator of $\boldsymbol{\theta}$. After some algebra we achieve the ML estimator of $\boldsymbol{\theta}$ as

$$\widehat{\boldsymbol{\theta}}_{ML} = \arg\max_{\boldsymbol{\theta}} \frac{|\sum_i y_i s_i^*(\boldsymbol{\theta})|}{\sum_i |s_i(\boldsymbol{\theta})|^2}. \tag{4.2.6}$$

Assuming that $a(u') = a(-u')$ and noting that $a(u') = a(\Delta y - \nu u') = a[\nu(\Delta y/\nu - u')]$, then (4.2.6) can be rewritten as the correlation

$$\widehat{\boldsymbol{\theta}}_{ML} = \arg\max_{\boldsymbol{\theta}} \frac{|\sum_i y_i s_{i-i_0}^*(\boldsymbol{\theta})|}{\sum_i |s_i(\boldsymbol{\theta})|^2}, \tag{4.2.7}$$

with

$$i_0 = \frac{\Delta y}{\nu u_s}. \tag{4.2.8}$$

4.3 Moving Target Parameter Estimation Algorithm

Algorithm 6 DetectMultipleTargetsMod

Initialization: η

repeat
  $(\hat{X}, \hat{Y}, l, s(X,Y))$:=**SearchStrongestTargetMod**$[S(k_u, \omega)]$
  if $l >= \eta$ **then** {found another candidate}
    $\hat{S}(\omega, k_u)$ =InverseWaveFront$[s(X,Y) * \overline{MASK(\hat{X}, \hat{Y})}]$
    $(\hat{x}_0, \hat{y}_0, \hat{\mu}, \hat{\nu})$ =**GetParameters**$[\mathcal{F}^{-1}_{(\omega,k_u)}(\hat{S}(x,u))]$
    $\hat{k}_{DC} = 2k\hat{\mu}$
    $\alpha = \sqrt{\hat{\mu}^2 + \hat{\nu}^2}$
    $\hat{X} = (\hat{\nu}\hat{x}_0 - \hat{\mu}\hat{y}_0)/\hat{\alpha}$
    $\hat{Y} = (\hat{\mu}\hat{x}_0 + \hat{\nu}\hat{y}_0)/\hat{\alpha}$
    $s(X,Y)$ =WaveFront$[s(k_u, \omega), \hat{k}_{DC}, \hat{\alpha}]$ {focus target}
    $s(k_u, \omega)$ =InverseWaveFront$[s(X,Y) * MASK(\hat{X}, \hat{Y})]$ {and remove it}
  end if
until $l < \eta$

In Algorithm 6 we present function **DetectMultipleTargetsMod** which is a modified version of Algorithm 1 presented in previous chapter. Although following the same ideas it was adapted to meet the needs of the estimator developed in this chapter. The strategy consists in searching, at each iteration, for the strongest target in the target area. This can be achieved with an algorithm similar to the one already presented in the previous chapter (Algorithm 2: **SearchStrongestTarget**), but with slight modifications, that is, it should also return a coarse estimation of the motion transformed coordinate $\hat{Y}$ and the compressed data in the (X,Y) domain [2]. The algorithm then carry on if the evaluation of the objective function exceeds a predetermined threshold. In such a case it resynthesizes the signature of the digitally spotlighted object, via an *inverse wavefront* algorithm. This procedure is shown in

[2] An efficient way to accomplish this goal consist in filtering in the 2D frequency domain the returns from the static ground and compress the data using the wavefront algorithm. The (X,Y) coordinates of the strongest target correspond to the position of the maximum absolute value of the compressed data.

step 4 of the algorithm. Function **GetParameters**, which is described in Algorithm 7, is then used to estimate parameters $(\hat{x}_0, \hat{y}_0, \hat{\mu}, \hat{\nu})$. The algorithm then proceeds to the next target after removing the current one from the data. This procedure is shown in steps 10-11.

Algorithm 7 GetParameters$(\hat{s}(x,u))$

Initialization: $\{\mu_i\}_{i=1}^{M_\mu}, \{\nu_i\}_{i=1}^{M_\nu}$

1: $(\hat{x}', \hat{y}')$ =**GetSignatureCenter**$[\hat{s}(x,u)]$
2: $u' = u - \hat{y}'$
3: **for** $i = 1 : M_\mu$ **do**
4: **for** $j = 1 : M_\nu$ **do**
5: $\boldsymbol{y} := s(\hat{x}' + \psi(u'), u')$ {form vector using data extracted along curve given by eq. (4.2.3)}
6: $\boldsymbol{o}$ =Correlation$[\boldsymbol{y}, \boldsymbol{s}]$ {correlation (4.2.7)}
7: $[value, coord] = GetMax(\boldsymbol{o})$
8: **if** $value > max$ **then** {found higher objective function value}
9: $max := value$
10: $\Delta y := coord$
11: $\hat{\mu} := \mu(i)$
12: $\hat{\nu} := \nu(j)$
13: **end if**
14: **end for**
15: **end for**
16: $\hat{y}_0 = \hat{y}' + \hat{\nu}\Delta y$
17: $\hat{x}_0 := \hat{x}' + \hat{\mu}\Delta y$

Function **GetParameters** is presented in Algorithm 7 and implements the scheme proposed to estimate parameters $(\hat{x}_0, \hat{y}_0, \hat{\mu}, \hat{\nu})$. It receives the resynthesized signature of the current moving target in the (x,u) domain (compressed in the fast-time domain but uncompressed on the slow-time domain). Then it uses as reference coordinates $(\hat{x}', \hat{y}')$ the *centre* of the signature. These coordinates are estimated by algorithm **GetSignatureCenter**. The algorithm then changes the coordinate reference in the slow-time domain according to $u' = u - \hat{y}'$ and performs a 2D search in the (μ, ν) space.

This search can be done via two one-dimensional searches as was done in scheme presented in the previous chapter. We opt now for the two-dimensional search just for the sake of clearness of the exposition. For each (μ, ν) pair, the algorithm form the observation vector $\boldsymbol{y}$ using data extracted along the curve given by eq. 4.2.3. In step 6 it computes the correlation (4.2.7). Step 7 of the algorithm retrieves the correlation maximum absolute value and the coordinate where it occurs. If the maximum value is the greatest observed until that iteration then it stores the value, position and the pair (μ, ν) for which it occurs. At the end of the algorithm $\hat{y}_0$ and $\hat{x}_0$ are computed.

Algorithm 8 GetSignatureCenter$(\hat{s}(x,u))$

1: $b(u) = SUM(abs(\hat{s}(x,u)), X_{DIM})$ $\{b$ contains the sum along the x dimension$\}$
2: $\hat{y}' =$**MeanCoord**$(b(u))$
3: $\hat{x}' =$**MeanCoord**$(\hat{s}(x,\hat{y}'))$

Algorithm 8 describes function **GetSignatureCenter**. The main idea behind the estimation of (x', y') consists in first summing, for each cross-range coordinate and along the x direction, all the absolute values of the resynthesized signature. Then, estimate as y' the coordinate corresponding to the mass center of the summation. Finally, estimate as x' the coordinate corresponding to the mass center of the signature along the coordinate estimated as y'. This strategy to estimate the coordinate pair $(\hat{x}', \hat{y}')$ is very simple but gives reasonable results, as will be seen on the results section.

Using the results from the presented strategy we have all the information needed to achieve a focused and correctly positioned image of the moving targets.

Table 4.1: Mission parameters used in the simulation.

Parameter	Value
Carrier frequency	5 GHz
Chirp bandwidth	100MHz
Altitude	12Km
Velocity	637Km/h
Look angle	20^0

4.4 Results

The scheme developed in the previous section to estimate the moving targets kinematics will now be evaluated using synthetic and real data. The synthetic data includes both point-like targets and extended targets. The real data includes a military transport vehicle, a BTR-60, from the MSTAR dataset, with simulated motion in a real background. Due to efficiency concerns, the observation vector we will not be filled with data data sampled on the exact curvature described by eq. (4.2.4). Instead, it will consist on data present on cell nearest to the desired range coordinate. Otherwise, a resampling or data interpolation should be done. Anyway, as will be seen, the results are quite good for most applications.

4.4.1 Synthetic data

In this subsection we present results using synthetic data. We will use three types of simulated targets: point-like targets, extended homogeneous targets and extended targets with predominant scatterers. The mission parameters used in the simulations are summarized in Table 4.1.

We will start by considering a point-like target moving with slant-range velocity $v_x = -7.959\,\mathrm{m/s}$ (exactly 3 times the maximum velocity imposed by the used PRF),

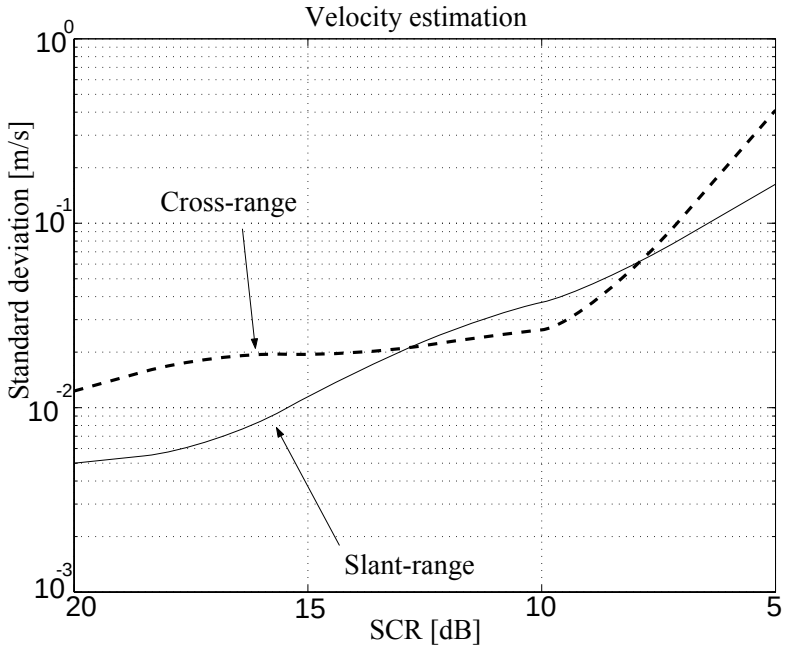

Figure 4.2: Velocity estimation as function of the SCR, for 64 monte-carlo runs. The achieved results enable the focusing of the moving targets even in low SCR conditions.

and cross-range velocity $v_y = 8\,\mathrm{m/s}$. The target cross-range coordinate is $y_0 = 209\,\mathrm{m}$ when the platform is at the center of the target area ($y = 0\,\mathrm{m}$). Using this point-like moving target, we carried out 64 Monte-Carlo simulations per SCR value. The clutter was simulated has having constant reflectivity modulus and phase uniformly distributed in a 2π interval. Fig. 4.2 presents the corresponding standard deviation of the velocity estimates as function of the SCR. For SCR$\geq$ 10dB, both the velocity components are accurately estimated. When the SCR is bellow that value, the estimates start to degrade seriously as can be seen in the plot. With a SCR of 20dB the algorithm is able to solve the azimuth ambiguity with an error of 0.45m. Fig. 4.4.1 plots the standard deviation of the error on the cross-range position estimation as function of the SCR. As can be seen, if the SCR is better than 10dB, the algorithm

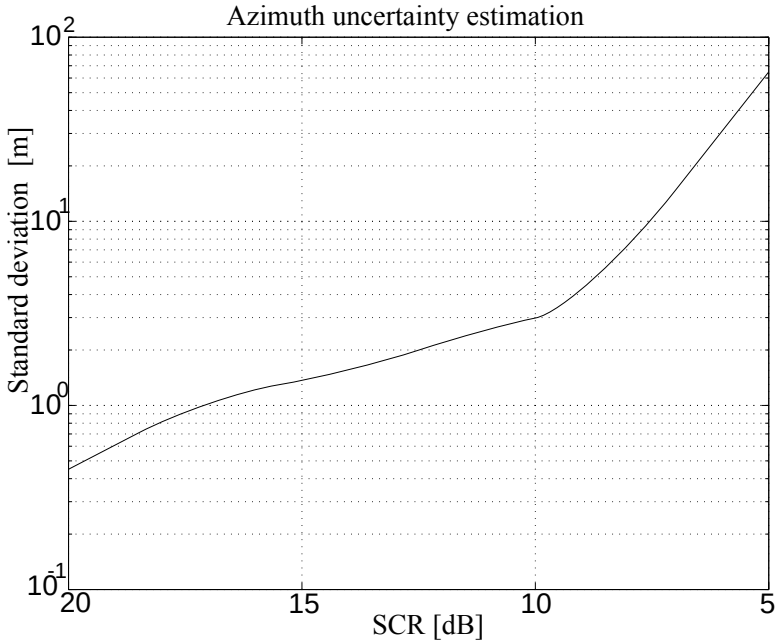

Figure 4.3: Moving object position estimation as function of the SCR, for 64 Monte Carlo simulations per point.

has the ability to reposition the moving target with accuracy high enough for most applications.

Our second experiment consists on applying the proposed scheme to an extended moving target with homogeneous reflectivity. The velocity parameters are those used on the previous experiment. A degradation is expected to occur because all the theory was developed for point-like targets. Although the slant-range velocity is estimated with an error of 0.3m/s the cross-range velocity component as suffered a high degradation and now exhibits an error of 4.2m/s. The repositioning in the cross-range dimension is also severely affected and presents now an error of 28.3m

The last experiment consists in repeating the simulation but now with an extended moving target exhibing a predominant scatterer (10dB above the average reflectivity). The results are expected to improve as the predominant scatterer will feed the estimator with data that partly behaves as a point-like target. The estimation results are really better than those of the previous simulation: the slant-range velocity has an error of 0.041 m/s and the cross-range velocity is estimated with an error of 0.29 m/s. The repositioning is done with an error of 1.6m. These estimation results enable both the focusing and the correct repositioning of the moving target. For illustration purposes, the likelihood function of $\boldsymbol{\theta}$ is sketched in Fig. 4.4.1.

Table 4.2 summarizes the estimation results for the three considered targets. As can be seen, if the target is point-like, or, if it has some predominant scatterers, the proposed scheme performs quite well and enables the velocity estimation, focusing and repositioning with accuracy high enough for most applications.

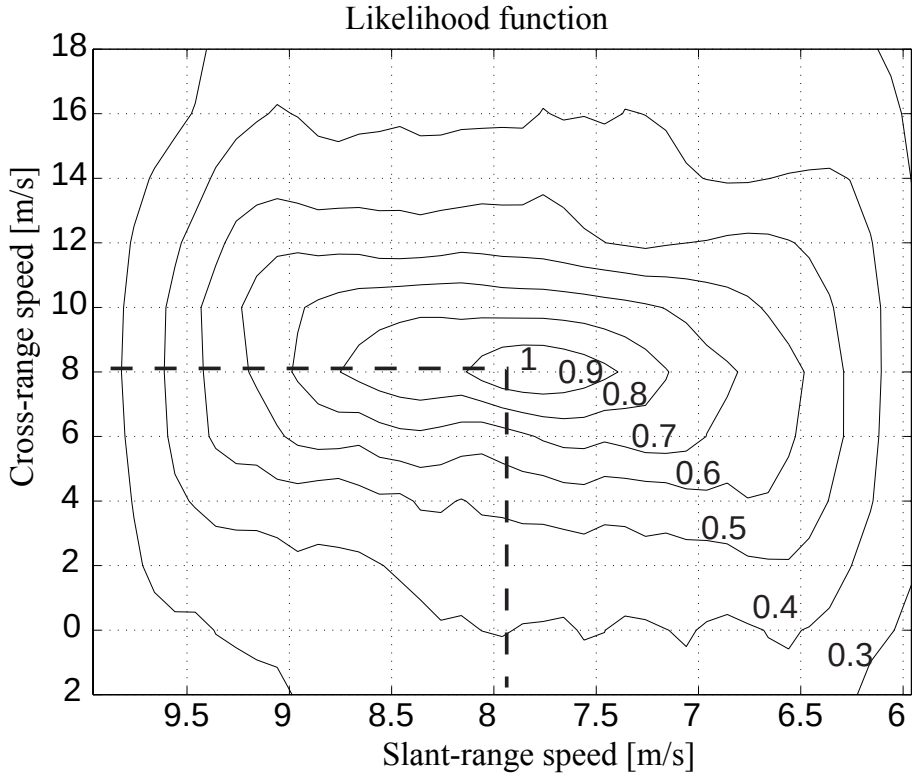

Figure 4.4: Likelihood function of the point-like target used in the simulation. The true velocity vector is $(v_x, v_y) = (-7.95, 8)$m/s. The estimated velocity vector is $(\hat{v}_x, \hat{v}_y) = (-7.945, 8.0123)$m/s.

Table 4.2: Estimation results for three types of targets (SCR=20dB). All the targets move with slant-range speed of -7.959m/s and cross-range speed of 8m/s. The slant-range speed is three times the maximum imposed by the mission PRF.

Target type	v_x error	v_y error	x_0 error	y_0 error
point-like	0,005m/s	0,0123m/s	0,02	0,45m
7×12m extended	0,3m/s	4,2m/s	0,18	28,3m
7× 12m extended (one predominant)	0,041m/s	0,29m/s	0,07	1,6m

Table 4.3: Mission parameters used with real data from MSTAR.

Parameter	Value
Carrier frequency	9.6 GHz
Chirp bandwidth	250MHz
Altitude	12Km
Velocity	637Km/h
Look angle	15^0
Antenna radiation pattern	Raised Cosine
Oversampling factor	2

4.4.2 Real data

We will now present results using a BTR-60 vehicle and the background scene from Hunstville-Alabama, both taken from the MSTAR data. To obtain a smaller dataset a low-pass filtering to the original data and a decimation by a factor of 4 was done in both directions.

The mission parameters are those presented in Table 4.3. The SCR is approximately 20dB. The velocity of the BTR-60 is $(v_x, v_y) = (16.58, 2)$ m/s. Notice that the slant-range velocity is 12 times the maximum allowed by the mission PRF.

Fig. 4.5 presents the target area focused with static ground parameters. As expected, the vehicle appears misplaced, blurred and defocused. If correctly processed, the BTR-60 image should appear positioned at coordinates $(x_0, y_0) = (90, 124)$m, that is, on the road. After detection using a very simple methodology, similar to that proposed in [24], we digitally spotlighted the BTR-60 signature and resynthesized it.

Fig. 4.6 displays the resynthesized signature and the estimated $(\hat{x}', \hat{y}')$ provided by algorithm **GetSignatureCenter**. Using the estimated coordinates $(\hat{x}', \hat{y}') = (87, 123)$m we then proceeded with the algorithm to estimate $\boldsymbol{\theta} = (v_x, v_y)$. The

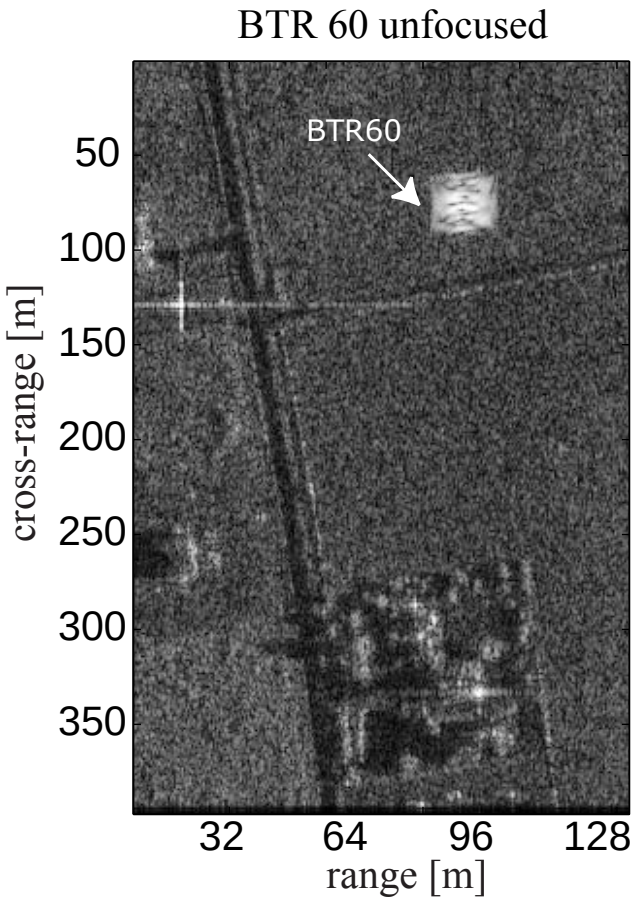

Figure 4.5: Target area focused using the wavefront reconstruction algorithm with static ground parameters. As expected, only the ground becomes focused. The moving vehicle appears misplaced, blurred and defocused. If correctly processed it should appear focused at coordinates $(x_0, y_0) = (90, 124)$m.

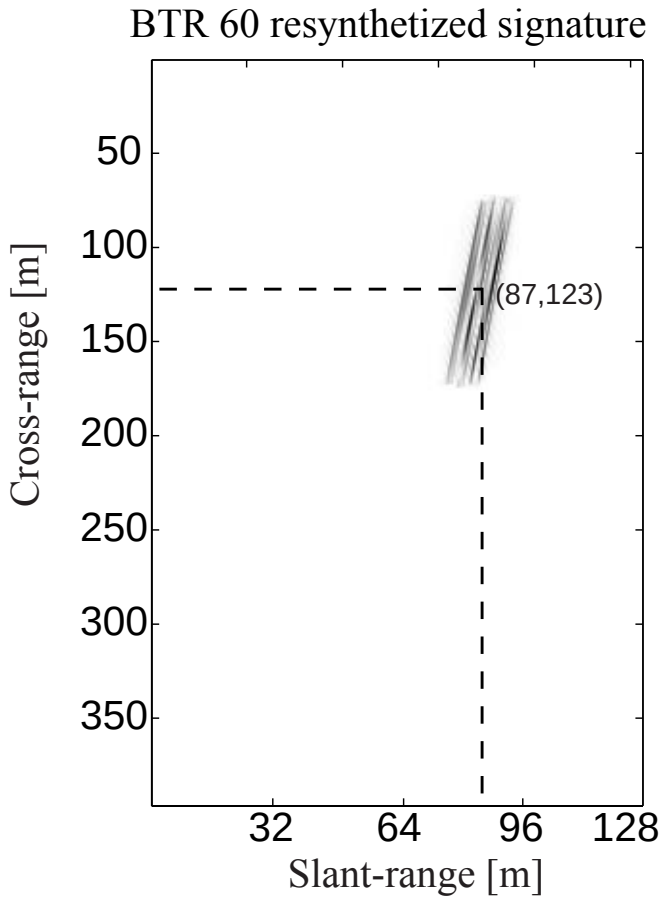

Figure 4.6: Resynthesized signature. Coordinates $(\hat{x}', \hat{y}') = (87, 123)$m were estimated by algorithm **GetSignatureCenter**.

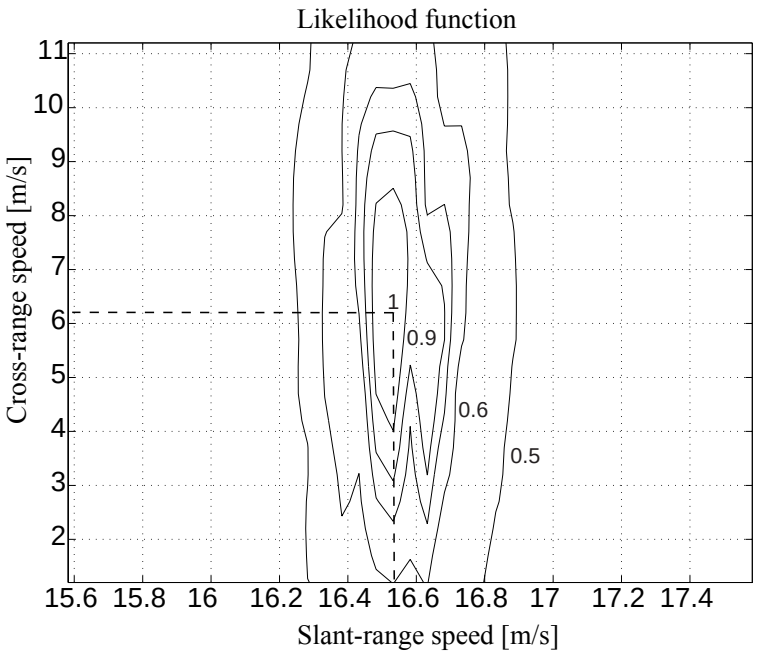

Figure 4.7: Likelihood function for the speed vector of the BTR-60 vehicle. The estimated velocity vector is $(\hat{v}_x, \hat{v}_y) = (16.53, 6.2)$m/s.

estimated velocity vector is $(\hat{v}_x, \hat{v}_y) = (16.53, 6.2)$m/s. The retrieved initial coordinates of the BTR-60 are $(\hat{x}_0, \hat{y}_0) = (87.6, 129)$m. These results permit both the focusing and repositioning of the moving target, as will be seen next. For illustration purposes the likelihood function of $\boldsymbol{\theta}$ is shown in Fig.4.7.

Using the estimated velocity and initial coordinates we focused and repositioned the BTR-60m as shown in Fig. **??**.

Notice that since we are using a single SAR sensor and because the moving target spectra (although 6 times folded) is completely superpositioned on that from the clutter, we cannot remove the defocused BTR-60 from the original image. To achieve that purpose we would need an induced Doppler-shift that shifts the spectra such that it does not completely overlap that from the clutter. Another possibility would be to have data from more than one SAR sensor [38].

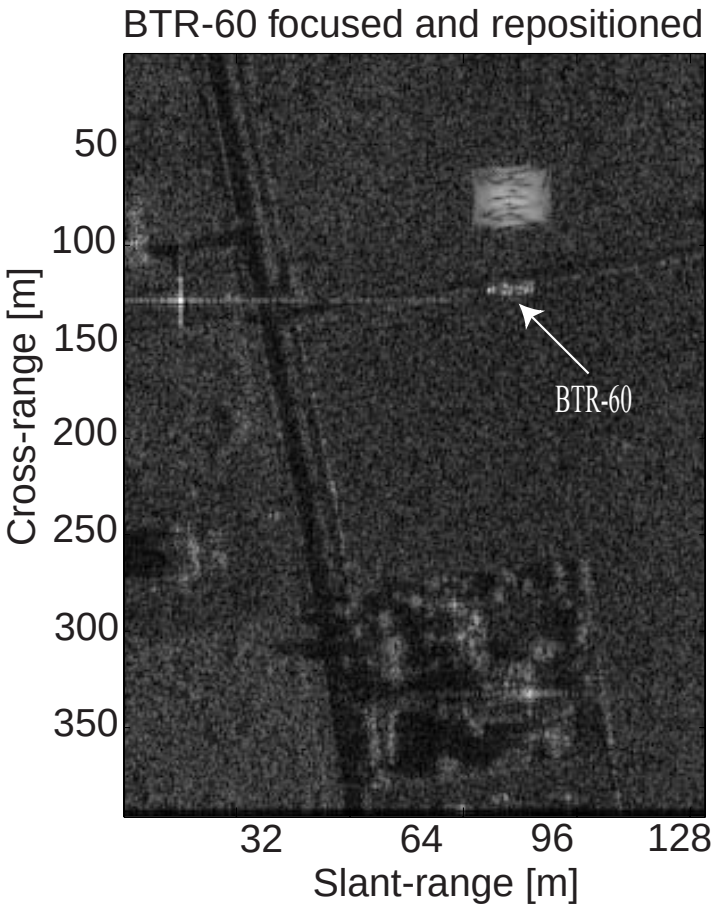

Figure 4.8: Focused and repositioned BTR-60. Notice that due to fact that a single SAR sensor is used and because the moving target spectra (although 6 times folded) is completely superpositioned on that from the clutter, the defocused BTR-60 cannot be removed from the image. To achieve that purpose using a single SAR sensor the velocity of the BTR-60 should induce a Doppler-shift on the returned echo such that it would not overlap that from the clutter, on the frequency domain.

Table 4.4: Estimation results for BTR-60 ($SCR = 20dB$). The target slant-range speed is $v_x = 16,58$m/s and the target cross-range speed is $v_y = 2$m/s. Notice that the slant-range velocity corresponds to 12 times the maximum unambiguous velocity allowed by the mission parameters.

Target type	v_x error	v_y error	x_0 error	y_0 error
BTR-60	0,005m/s	4,2m/s	2,4m	5m

The obtained results for the BTR-60 under study are summarized on table 4.4. As can be seen, the proposed methodology gave good velocity and position estimates. Using them we were able to focus and reposition the vehicle, with accuracy high enough for most common purposes.

From the results presented in this section we can conclude that the suggested strategy works well in the case of point-like targets or extended targets exhibiting some predominant targets. When this is not the case the algorithm still gives good results for the slant-range velocity. However it produces large errors on the cross-range velocity estimation and on the estimated cross-range initial position. However, the presented methodology can be used to estimate the velocity and initial coordinates of most man-made targets, since typically they exhibit predominant scatterers.

4.5 Conclusions

In this chapter we have presented a methodology for the estimation of all the moving target parameters using a single sensor. The main algorithm works in the (x, u) domain and gets the data along the signature curvature that is dependent of the moving target kinematics. To achieve efficiency and simplicity we derived the ML estimator of the velocity parameters by considering that the clutter behaves as white noise. That assumption lead us to a matched filter solution. The suggested methodology was shown to enable the estimation of both the full velocity vector of a moving target and its initial coordinates. Using this information we were able to focus the moving objects and reposition them on their approximate true coordinates. This strategy was tested with targets inducing Doppler-shifts beyond the Nyquist limit imposed by the mission PRF. In all experiments the targets had velocities ranging from 3 to 12

times the Nyquist limit. This limitation is overcome due to the fact that the velocity information is extracted in the 2D spatial domain instead of the Doppler-domain as is done by most techniques published in recent literature. A limitation inherent to the fact that we use a single SAR sensor was also readily apparent: although the proposed scheme enables the repositioning of the moving objects, in some situations their defocused versions cannot be removed on the original data. Such a case occurs when the moving objects spectra completely overlaps the clutter spectra.

The methodology was tested using a combination of simulated and real data. All the used moving targets had slant-range velocities well beyond the Nyquist limit imposed by the mission PRF. The technique was shown to provide good results when the objects are point-like targets or extended targets provided they exhibit some predominant scatterers. When this is not the case the slant-range velocity is estimated with good accuracy. However, the algorithm is no longer able to give accurate estimates of the cross-range velocity and the initial coordinates. To improve the estimation results we could perform more than one iteration of the algorithm, using corrected coordinate pair $(\hat{x'}, \hat{y'})$. However, the computational efficiency now achieved, when compared with the methodology presented on the previous chapter, would be lost.

Chapter 5

Unambiguous Doppler Shift Estimation for Moving Targets with High Range Velocity

5.1 Introduction

In Chapter 2 we have shown that a moving target induces in the synthetic aperture radar returned signal a Doppler-shift and a Doppler-spread in the slow-time frequency domain. Most techniques proposed in the recent literature to image moving targets and estimate their velocity parameters take advantage of this knowledge e.g., [6], [24], [46], [60]. Assuming a broadside geometry, the cross-range and slant-range velocities of a moving target are responsible for the spread and for the Doppler-shift, respectively, both in the slow-time frequency domain. Given a pulse repetition frequency (PRF), the Doppler-shift $f_D = 2v_x/\lambda$, where v_x is the target slant-range velocity and λ is the signal wavelength, is confined to

$$\frac{-PRF}{2} < f_D \leq \frac{PRF}{2}. \tag{5.1.1}$$

If the received signal is aliased (i.e., the induced Doppler-shift exceeds $PRF/2$) it has been mostly accepted that the true moving target slant-range velocity cannot be uniquely determined using a single antenna and a single pulse scheduling [4], [41]. Classical solutions to process such targets with a single antenna consist in increasing the PRF [4] or, alternatively, in using a non-uniform PRF as proposed in [41] and [62]. Increasing the PRF shortens the unambiguous range swath and increases the memory requirements to store the received signal. The use of a non-uniform PRF requires a non-conventional pulse scheduling, introducing complexity in image reconstruction algorithms.

In [36], a method has been proposed which copes with target motion induced Doppler-shifts up to $(3/2)\,PRF$. This is done by evaluating the Doppler-shift - possibly affected by aliasing - together with the range walk of the target. The present chapter proposes a novel technique to estimate the slant-range velocity of ground-based moving targets with velocities above the Nyquist limit. The method takes advantage of the linear dependence of the Doppler-shift on the slant-range velocity, at each fast-time frequency. In the two-dimensional frequency domain, a moving target echo exhibits a skew not subject to PRF limitations. In [3] this fact has already been exploited to retrieve the spectral support of SAR signals, with application to low contrast ground scenes in spaceborne SAR. In these scenarios the ground behaves as a moving target due to the earth rotation relatively to the radar platform. The method proposed therein works by applying a linear regression on the estimated Doppler centroids at each fast-time frequency. The problem that we are dealing with in this thesis cannot be solved by the same technique, because we are interested in returns from near point-like moving targets (e.g., many man-made objects), relatively to the

ground. Even after digitally spotlightingthe moving target signatures [54], the ground echoes exhibit sufficient power to corrupt the estimates given by spectral centroid type estimators. In this chapter we present a technique able to cope with this scenario. For scenes with signal-to-clutter ratio (SCR) higher than 14dB, the proposed estimator is effective, even when the ground echoes are completely superimposed, in the frequency domain, on the moving objects echoes.

This chapter is organized as follows. In Section 5.2 we review basic properties of moving target echoes in SAR and present the proposed methodology to retrieve unaliased estimates of the slant-range velocity. In Section 5.3 we show results taking real and simulated data to illustrate the effectiveness of the proposed scheme. We also study the applicability of the proposed technique for situations that do not comply with the the assumptions taken to derive the estimator.

5.2 Proposed Approach

This section derives the properties of the SAR raw-data echoed from a moving target in the two-dimensional frequency domain. After addressing the properties of the clutter raw-data in the two-dimensional frequency domain, we propose a methodology to unambiguously estimate the slant-range velocities of multiple moving targets.

In Chapter 2 we have shown that the amplitude modulation term $A(k_u, k)$ of the returned echo from a moving target takes, in the two-dimensional frequency domain, the shape of the two-way antenna radiation pattern according to

$$A(k_u, k) \propto g^2 \left(\frac{1}{2\nu}(k_u - 2k\mu) \right), \tag{5.2.1}$$

where g is related with the 2D Fourier transform of the electric field at the antenna

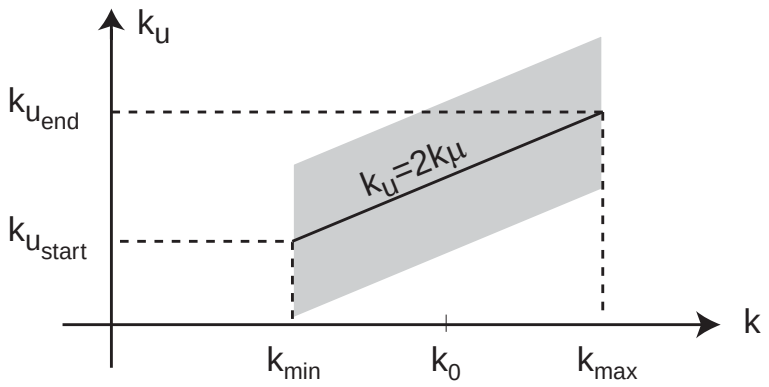

Figure 5.1: Support of the returned signal from a moving target with relative range velocity μ.

aperture.

Relatively to a static target, the shape g becomes shifted by $2k\mu$ and expanded by 2ν. If the transmitted pulse has bandwidth B, then k is confined to

$$k_{min} \cong -\frac{\pi B}{c} + k_0 < k \leq k_0 + \frac{\pi B}{c} \cong k_{max}, \tag{5.2.2}$$

where $k_0 \equiv 2\pi/\lambda_0$ and λ_0 is the carrier wavelength. For a moving target with relative slant-range velocity μ, we see from expression (5.2.1) that the support of the returned signal, $S_m(k_u, k)$, exhibits a slope of 2μ with respect to the k axis, as illustrated in Fig. 5.1. In this figure, $k_{u_{end}}$ and $k_{u_{start}}$ denote the Doppler-shifts at the fast-time frequencies k_{max} and k_{min}, respectively. We conclude then that

$$\mu = \frac{k_{u_{end}} - k_{u_{start}}}{2(k_{max} - k_{min})}, \tag{5.2.3}$$

regardless of the PRF. In the absence of electronic noise and ground clutter, $k_{u_{end}}$ and $k_{u_{start}}$ could be inferred using a simple centroid technique. This solution cannot, however, be applied in the case of ground moving targets, because the returned signal co-exists with clutter returns in the 2D spectrum. The weight of the clutter can be

reduced by spotlighting the moving target area [54]. This process consists in focusing with approximated moving target parameters (recall that the true moving target parameters are not known) and cropping the region containing the target of interest. In this chapter we focus the target region using static ground parameters ($\alpha = 1$). The moving targets will appear defocused, as their relative velocity α is different from the value used to focus the target region. They span, however, a region that is usually much smaller than the total illuminated scene. Each moving target can thus be *reasonably* separated from the signatures of the other (moving and stationary) targets. Once the moving target signature is spotlighted in the spatial domain, it is resynthesized back to the 2D frequency domain for further processing.

We show in the Appendix B.2 that if the number of the ground scatterers is large, none is predominant, and they are uniformly distributed within a wavelength, then the correlation of the static ground returns, in the (k_u, k) domain, decays very quickly in both dimensions. Concerning moving targets, the same is not true, as it is shown in the next subsection. Thus, the signals echoed by moving targets have statistical properties quite different from those of the clutter. In this chapter we exploit these distinct properties to derive a methodology to unambiguously estimate the moving targets slant-range velocities.

5.2.1 Moving target signature properties

The received signal from a moving target in the 2D frequency domain (k, k_u), after pulse compression, is given by (2.2.1) which we rewrite bellow

$$S_m(k, k_u) = |P(\omega)|^2 A(k, k_u) f_m e^{-j\sqrt{4k^2 - \left(\frac{k_u}{\alpha}\right)^2} X} e^{-j\frac{k_u}{\alpha} Y}, \tag{5.2.4}$$

where we recall that $P(\omega)$ is the Fourier transform of the transmitted signal, f_m is the moving target complex reflectivity, (X, Y) are the motion transformed coordinates, and $\alpha = \sqrt{\mu^2 + \nu^2}$ is the relative speed of the moving target with respect to the radar.

The autocorrelation function $R_{SS}(\Delta k_u, k_1, k_2)$ between $S_m(k_u, k_1)$ and $S_m(k_u, k_2)$ with respect to k_u is

$$R_{SS}(\Delta k_u, k_1, k_2) = \int_{-\infty}^{+\infty} S_m(k_u, k_1) S_m^*(k_u - \Delta k_u, k_2) dk_u. \tag{5.2.5}$$

From (5.2.1) we can write $A(k_u, k_1 + \Delta k) = A(k_u - 2\Delta k\mu, k_1)$. Using this fact and after applying some algebra to (5.2.5), we are lead to

$$\begin{aligned} &R_{SS}(\Delta k_u, k_1, k_1 + \Delta k) \approx \\ &\quad |P(\omega_1)|^2 |P(\omega_2)|^2 |f_m|^2 e^{-j\left[\frac{\Delta k_u}{\alpha} Y - \left(2\Delta k - \frac{\Delta k_u^2}{4(k_1 + \Delta k)\alpha^2}\right) X\right]} \\ &\times \int_{-\infty}^{+\infty} A(k_u, k_1) A^*(k_u - 2\Delta k\mu - \Delta k_u, k_1) e^{j\phi} dk_u, \end{aligned} \tag{5.2.6}$$

where $\omega_1 = k_1 c$, $\omega_2 = k_2 c$, $\Delta k = k_2 - k_1$, and

$$\phi = \frac{2 k_u \Delta k_u}{4(k_1 + \Delta k)\alpha^2} X. \tag{5.2.7}$$

If phase ϕ has an excursion smaller than π in the Doppler interval equivalent to the *antenna bandwidth*[1], the last line of (5.2.6) is a correlation between $A(k_u, k_1)$ and $A(k_u - 2\Delta k\mu, k_1)$, with respect to k_u, computed at Δk_u. The correlation magnitude $|R_{SS}(\Delta k_u, k_1, k_1 + \Delta k)|$ exhibits a maximum that is linearly dependent on Δk by a factor of 2μ.

The maximum relative slant-range velocity that can be estimated using this methodology is thus imposed by the above referred restriction on phase ϕ. To compute an

[1]Herein we use the term *antenna bandwidth* to designate the slow-time wavenumber interval corresponding to the -3 dB two-way beamwidth of the antenna.

expression for the maximum relative slant-range velocity that can be estimated, let us consider that the maximum magnitude of the correlation R_{SS} occurs at $\Delta k_u = 2\Delta k\mu$ and that the two-way antenna bandwidth is B_u $[rad/m]$. Considering that the relative velocity is $\alpha \approx 1$, then the relative slant-range velocity that can be estimated is bounded by

$$|\mu| < \frac{(k + \Delta k)\pi}{B_u \Delta k X}. \tag{5.2.8}$$

Bound (5.2.8) can be made larger by compensating in (5.2.4) the dependency on X using the target area approximate slant-range coordinates; i.e., multiplying signal $S_m(k_u, k)$ in (5.2.4) by $\exp\{j\sqrt{4k^2 - (k_u/\alpha')^2}X'\}$, where X' is the target approximate slant-range coordinate in the unfocused image and $\alpha' = 1$ is the target approximate velocity vector magnitude. In this way, phase ϕ, although not completely compensated, will exhibit a smaller excursion.

As a numerical example of bound (5.2.8), let us consider the AER-II SAR system parameters mentioned in [20] and an error of 50 m in the slant-range coordinate X of the moving target. Assuming the Transall aircraft cruise speed of 495 km/h, the maximum unambiguous velocity is approximately 200km/h, which is sufficient for most man made ground vehicles.

Another possibility to make the limit (5.2.8) less tight consists in partitioning the overall pulse-bandwidth into smaller bands, and computing μ by averaging the estimates of all bands.

In deriving (5.2.6) we have assumed that the antenna pattern $A(k_u, k)$ does not depend on the wavenumber k in the pulse bandwidth interval. This is valid for planar antennas [55, Ch. 6.3]. In the case of a curved radar aperture the antenna pattern depends on k. Nevertheless, this dependency does not invalidate the concepts just

presented as its effect does not occur in the Doppler domain.

5.2.2 Proposed methodology

In a realistic SAR scenario the received moving target echoes are *contaminated* with returns from the clutter and with electronic noise. Thus, the received signal $S(k_u, k)$ can be written, in the Fourier domain, as

$$S(k_u, k) = S_m(k_u, k) + S_0(k_u, k), \tag{5.2.9}$$

where S_0 is the term due to the clutter plus the electronic noise.

Based on the statistics of S_0 and on expression (5.2.4) of S_m, we could derive a maximum likelihood estimator of μ. However, the signal S_m depends on the unknown terms X, Y, α, and $A(k_u, k)$, besides the parameter μ in which we are interested. This dependency introduces complexity in the maximum likelihood approach. By exploiting the structure of the correlation between $S_m(k_u, k_1)$ and $S_m(k_u, k_2)$, we herein adopt a suboptimal solution that is simpler and, nevertheless, effective.

Based on the analysis made in the previous subsection, we present the following methodology to unambiguously compute μ:

1) Estimate a rough location of the moving targets using one of the strategies described in Chapter 1 and Chapter 3. Herein we adopt a methodology similar to that proposed by Freeman in [24] because it is simple and leads to good results. The strategy consists in first applying a high-pass filter in the (k_u, k) domain with stop-band adjusted to filter out static targets and then performing imaging using static ground parameters. A rough slant-range coordinate X' for each moving target is inferred from its slant-range position.

2) Process the SAR raw-data as if there were only static targets. The ground appears focused and the moving targets appear smeared, defocused, and misplaced.

3) For each detected moving target:

3.1) Digitally spotlight the moving target image in the spatial domain and re-synthesize its signature back to the (k_u, k) domain as described in the previous chapters, obtaining the signal $\hat{S}_m(k_u, k) = S_m(k_u, k) + S_{0R}(k_u, k)$, where S_{0R} denotes the remaining noise after the digital spotlight operation.

3.2) Proceed as illustrated in Algorithm 9. The algorithm receives as arguments the resynthesized signature $\hat{S}_m(k_u, k)$ and the target approximate slant-range coordinate X' and computes the estimate of μ. It starts by compensating phase ϕ using X' and the approximate relative velocity $\alpha' = 1$. This is accomplished by multiplying $\hat{S}_m(k_u, k)$ by $\exp\{j\sqrt{4k^2 - (k_u/\alpha')^2}X'\}$. If a more accurate phase compensation is needed, α can be estimated using the algorithm presented in [54].

The algorithm then computes the correlation $R_{\hat{S}\hat{S}}$ between $\hat{S}_m(k_u, k_0)$ and $\hat{S}_m(k_u, k)$ for a set of discrete wavenumbers within the transmitted pulse bandwidth. We obtain then

$$\begin{aligned} R_{\hat{S}\hat{S}}(\Delta k_u, k_0, k) &= R_{SS}(\Delta k_u, k_0, k) + R_{NN}(\Delta k_u, k_0, k) \\ &+ R_{SN}(\Delta k_u, k_0, k) + R_{NS}(\Delta k_u, k_0, k). \end{aligned} \tag{5.2.10}$$

Terms R_{SS} and R_{NN} denote the moving target and clutter-plus-noise autocorrelations, respectively. Terms R_{NS} and R_{SN} denote the crosscorrelations. The last three

terms are expected to have insignificant values when compared to R_{SS}. As shown in (5.2.6), $|R_{SS}|$ displays a maximum for each k at $\Delta k_u = 2(k - k_0)\mu$. In order to have independent clutter samples, the sampling interval in the Fourier domain should be large enough (see expressions (B.2.9) and (B.2.10) in Appendix I).

The last step of the algorithm consist in computing the linear regression on the ordinates corresponding to the maximum values of $|R_{SS}|$ to estimate μ and subsequently compute the target slant-range velocity. As shown in Appendix C.1, the slant-range velocity estimation accuracy is proportional to the number of independent samples used to compute the linear regression.

The suggested scheme relies on the detectability of the moving targets. As shown in Chapter 3 the moving targets most hard to detect are those with cross-range velocity parallel to the platform motion (i.e., $\nu \leq 1$) and slant-range velocities inducing Doppler-shifts in the slow-time frequency domain such that the moving target spectrum completely overlaps the clutter spectrum. The moving target detection strategy proposed in step 1) of the algorithm works by filtering out the static ground echoes in the (k_u, k) frequency domain. The proposed scheme, in spite of being very simple, yields good results even for moving targets with slant-range velocities multiple of the Nyquist velocity, as far as the respective two-dimensional spectrum exhibits a non-negligible skew.

In low SCR and low skew scenarios the moving target detection demands more sophisticated algorithms such as those proposed in Chapter 3, [22], or [23], [54], at expense of higher computational complexity. In Chapter 3 we have developed a

moving target detection strategy that is able to detect moving targets in the case of parallel to platform target motion, the most unfavourable scenario, for SCR as low as 10dB.

Notice that the suggested scheme does not require the knowledge of the parameters Y, α, or $A(k_u, k)$. It just needs an approximate value of X to estimate μ. This approximate value is given by the slant-range position where the moving target is imaged after applying the moving target imaging (MTI) algorithm described in step 1). To estimate the cross-range velocity component of each moving target, we suggest the combination of the scheme herein proposed to estimate μ with the methodology presented by Soumekh in [55, Ch. 6.7] to estimate $\alpha = \sqrt{\mu^2 + \nu^2}$. With the two quantities μ and α at hand, the estimation of ν is straightforward.

Algorithm 9 GetParameter$\boldsymbol{\mu}(\hat{S}_m(k, k_u), \hat{X})$

Initialization: $\{k_i\}_{i=1}^{M_k}$

1: $\hat{S}_m(k_u, k) = \hat{S}_m(k_u, k) \times \exp\{j\sqrt{4k^2 - k_u}\hat{X}\}$ {phase compensation}
2: $r = \hat{S}_m(k_u, k_0)$ {form reference signal at $k = k_0$}
3: **for** $i = 1 : M_k$ **do**
4: $\quad \boldsymbol{c}$ =**Correlation**$[r, \hat{S}_m(k_u, k(i))]$
5: $\quad \Delta k_u(i) = GetMax(\boldsymbol{c})$
6: **end for**
7: $\hat{\mu}$ =**LinearRegression**$[k, \Delta k_u]$

5.3 Results

The scheme proposed in the previous section is now applied to synthetic data and real data from the MSTAR public collection [57]. The synthetic data set contains seven moving targets, all with cross-range velocities several times above the Nyquist limit. The experiments with MSTAR data include clutter from Hunstville-Alabama

Table 5.1: Mission parameters used in simulation.

Parameter	Value
Carrier frequency	9 GHz
Chirp bandwidth	250MHz
Altitude	12Km
Velocity	637Km/h
Look angle	20^0
Antenna radiation pattern	Raised Cosine
Oversampling factor	2

Table 5.2: Moving targets parameters.

Target	x_0 [m]	y_0 [m]	v_x [km/h]	v_y [km/h]	$\frac{\lfloor v_x \rfloor}{v_{max}}$
1	-64	-64	-13.2	-36	2.5
2	0	-64	-26.5	-36	5
3	64	-64	-52.9	-36	10
4	-64	+64	13.2	36	2.5
5	0	+64	26.5	36	5
6	64	+64	52.9	36	10
7	0	0	52.9	0	10

and two BTR-60 transport vehicles with simulated movement.

5.3.1 Synthetic data

The synthetic data set includes six point-like targets and an extended target with dimensions of 6 meters in slant-range by 2 meters in cross-range. The extended target is simulated by using twelve point-like targets, all with the same reflectivity. The SCR, i.e., the ratio between the peak (squared magnitude) of the correctly focused moving target signal and the covariance of the clutter background, is set to 23dB. The mission parameters are presented in Table 5.1. The moving targets trajectory parameters are summarized in Table 5.2. Targets numerated from one to six are

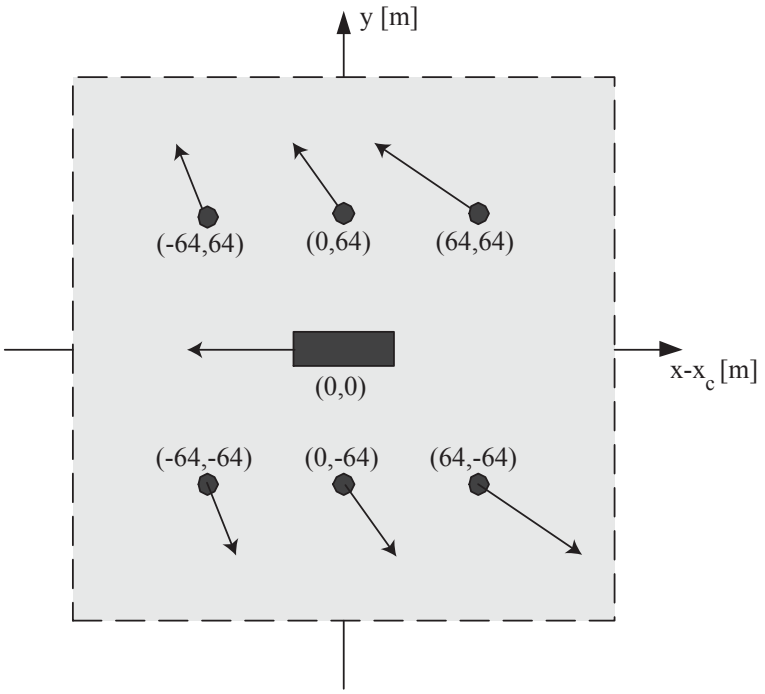

Figure 5.2: Simulated positions and velocities of moving targets. The slant-range coordinates are recentered at the central slant-range coordinate x_c. The velocity vector of each target is represented by an arrow with length proportional to the velocity magnitude.

point-like, whereas target number seven is extended. Coordinates x_0 and y_0 denote the moving targets positions when the SAR platform is at $u = 0$. The slant-range coordinates are recentered at the central slant-range coordinate x_c. The last column of this table displays the ratio between the moving target slant-range velocity magnitude $|v_x|$ and the maximum slant-range velocity allowed by the mission PRF, v_{max}. Notice that all the moving targets have slant-range velocities several times larger than the Nyquist velocity. Figure 5.2 shows the moving targets positions and their respective velocities. Each velocity vector is represented by an arrow with length proportional to the velocity magnitude.

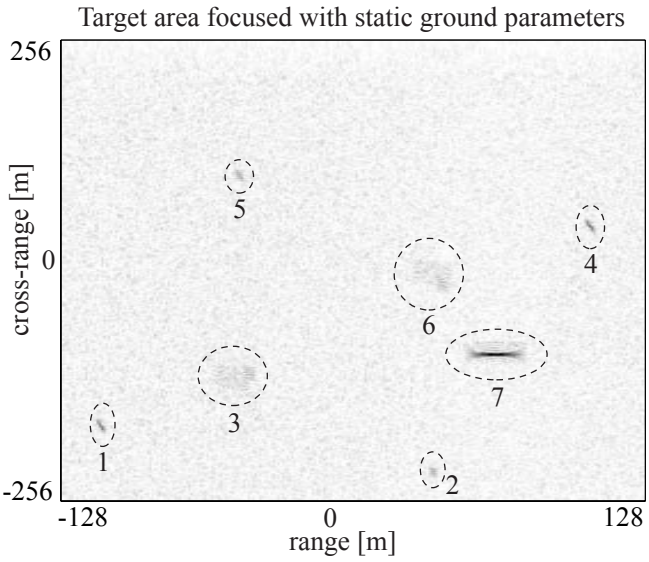

Figure 5.3: Reconstructed SAR image with static ground parameters. Moving targets appear defocused and misplaced.

Figure 5.3 presents the target area image focused using the wavefront reconstruction algorithm [55] with static ground parameters. As expected, all the moving targets appear misplaced and blurred. To detect the moving targets we proceed as explained in the first step of the algorithm described in Section II. We start by applying high-pass filtering in the (k_u, k) domain with stop-band adjusted to filter out static targets. In the present situation this procedure consists in setting to zero the data inside the interval $-\pi/2 < k_u < \pi/2\,[\text{rad/m}]$. We then perform imaging using the wavefront reconstruction algorithm with static ground parameters. The resulting MTI function is presented in Fig. 5.4, where we can see that all moving targets are clearly detectable.

For illustration purposes, we show in Fig. 5.5a) and Fig. 5.6a) the magnitude of the digitally spotlighted signatures of point-like target 3 and extended target 7, respectively.

In Fig. 5.5b) and Fig. 5.6b) we show the resulting data after performing the

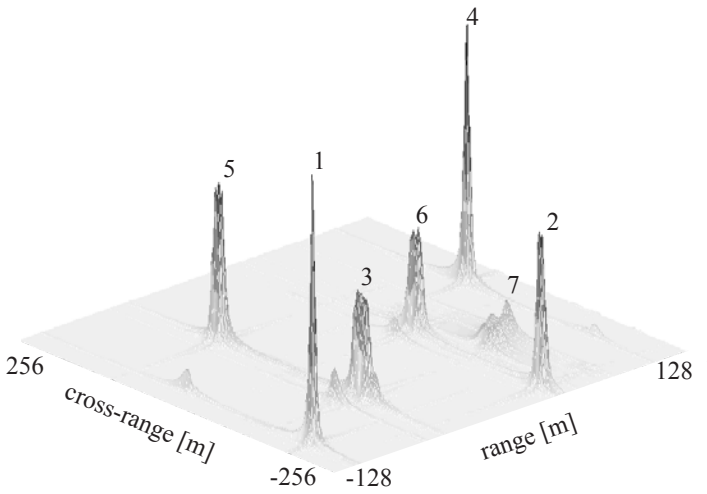

Figure 5.4: MTI function after static ground filtering.

Table 5.3: Slant-range velocity estimation results (SCR=23dB).

Target	$v_x[km/h]$	$\hat{v}_x[km/h]$	error
1	-13.2	-13.25	0.4%
2	-26.5	-26.69	0.6%
3	-52.9	-53.21	0.6%
4	13.2	13.24	0.3%
5	26.5	26.26	0.9%
6	52.9	52.5	0.7%
7	52.9	53.03	0.3%

proposed correlation. A straight line is clearly visible in both figures, although in the case of the moving target 7 the interaction between the multiple scatterers that compose the object causes the amplitude to fluctuate. The slope of the resulting lines is estimated by means of a linear regression. Table 5.3 presents the slant-range velocity estimates for all the moving objects in the scene. The accuracy is better than 1% for all targets and can be used to retrieve the true Doppler interval where the moving target signature belongs to.

To estimate the full velocity vector we combined the unaliased estimates of the

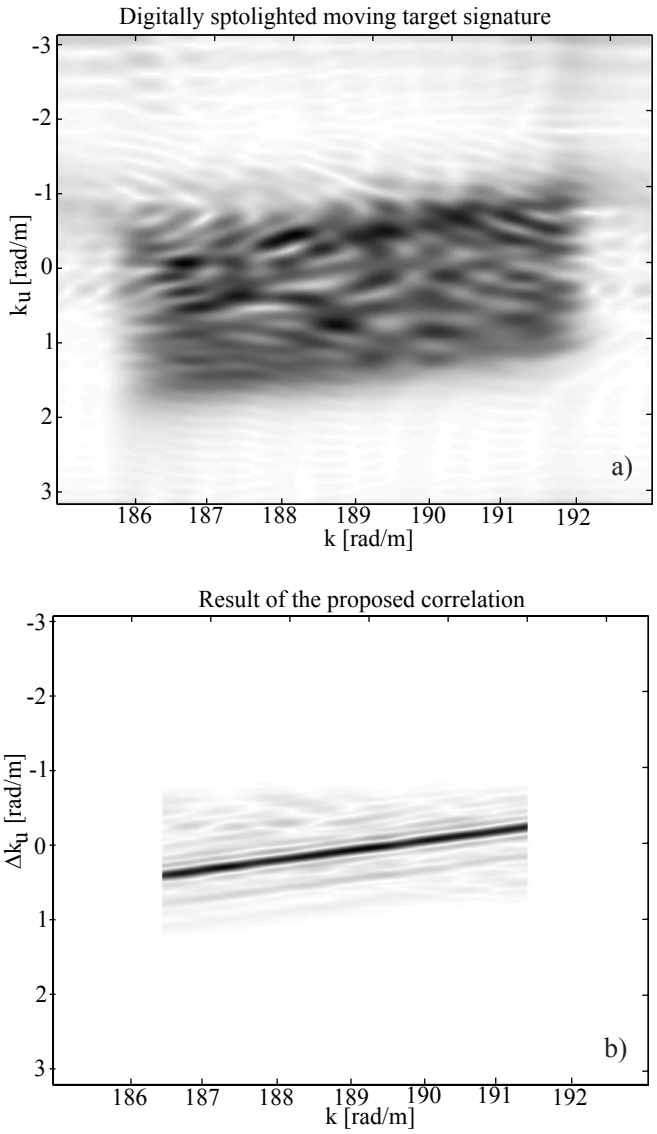

Figure 5.5: a) Moving target 3 signature in the (k_u, k) domain after the digital spotlight operation. b) The maximum of the proposed correlation changes linearly with the fast-time frequency as predicted.

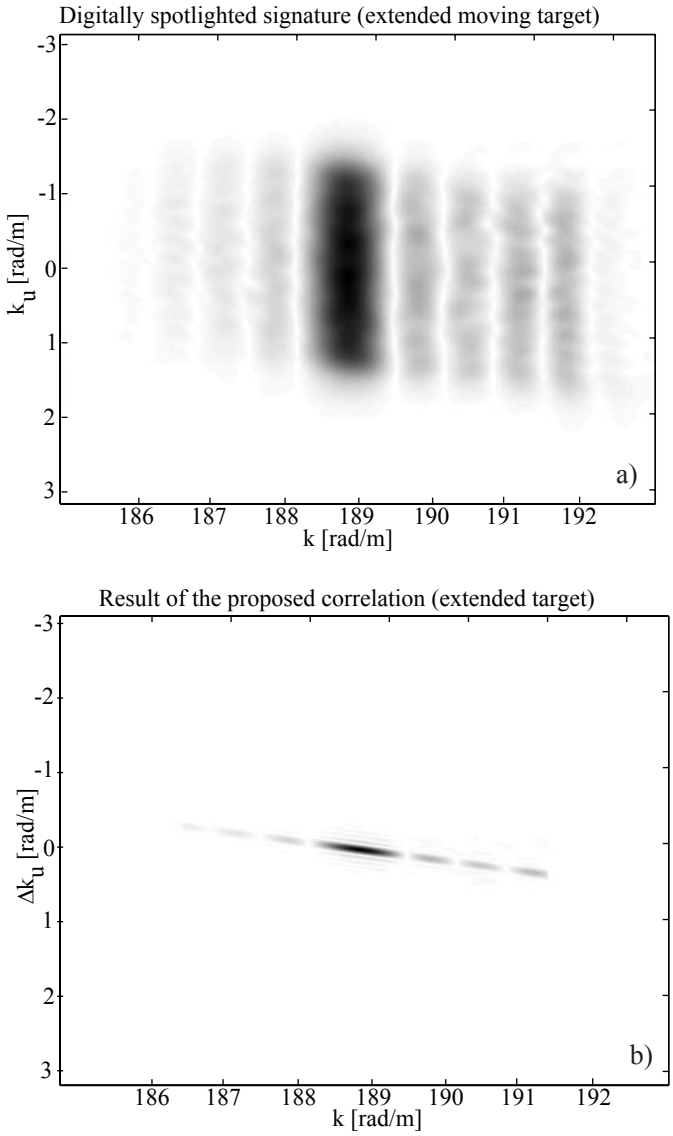

Figure 5.6: a) Extended moving target 7 signature in the (k_u, k) domain after the digital spotlight operation. b) Result from the proposed correlation. The maximum exhibits a fluctuation due to the interaction between the multiple scatterers that compose the object.

Table 5.4: Complete velocity vector estimation by joining two methodologies (SCR=$23dB$).

Target	$(v_x, v_y)[km/h]$	$(\hat{v}_x, \hat{v}_y)[km/h]$
1	(-13.2,-36)	(-13.25,-35.53)
2	(-26.5,-36)	(-26.69,-35.78)
3	(-52.9,-36)	(-53.21,-32.9)
4	(13.2,36)	(13.24,32)
5	(26.5,36)	(26.26,38.8)
6	(52.9,36)	(52.5,37.33)
7	(52.9,0)	(53.03,1.54)

slant-range velocity obtained herein with the estimates of the relative speed α measured as proposed by Soumekh in [55, ch. 6.7]. Table 5.4 presents the resulting full velocity vector estimates, illustrating the usefulness of this method. The accuracy is better than 2% with respect to the velocity vector norm.

5.3.2 Real data

In this subsection we apply the proposed strategy to real data from the MSTAR public collection. The clutter scene is taken from Huntsville, Alabama. The moving objects are two BTR-60 transport vehicles with simulated movement. The optical and X-band images of this type of vehicle are presented in Fig. 5.7.

The nth moving target signature was generated, according to (5.2.4), by computing

$$S_{mn}(k_u, \omega) = \sum_i A_n(k_u, k) P(\omega) f_{in} e^{-j\sqrt{4k^2 - \left(\frac{k_u}{\alpha_n}\right)^2} X_{ik} + \left(\frac{k_u}{\alpha_n}\right) Y_{ik}}, \tag{5.3.1}$$

where indexes i and n denote the ith pixel of the nth moving target. Function A_n is the two-way antenna radiation pattern for the nth moving target given by (5.2.1).

The mission parameters for the MSTAR data are presented in Table 5.5. Table

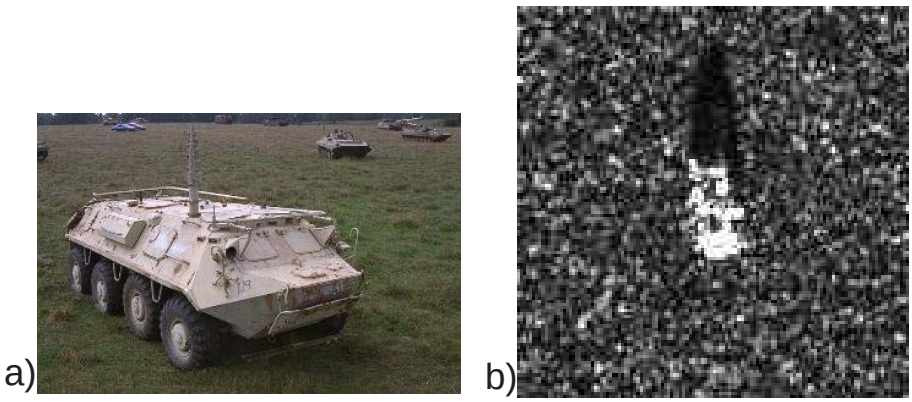

Figure 5.7: BTR-60 Transport vehicle a) optical; b) X-band.

Table 5.5: Real data mission parameters.

Parameter	Value
Carrier frequency	9.6 GHz
Chirp bandwidth	250MHz
Altitude	12Km
Velocity	637Km/h
Look angle	15^0
Antenna radiation pattern	Raised Cosine
Oversampling factor	2

Table 5.6: BTR-60 Transport vehicle trajectory parameters.

Target	x_0 [m]	y_0 [m]	v_x [km/h]	v_y [km/h]	$\frac{\lvert v_x \rvert}{v_{max}}$
1	75	220	29.85	36	6
2	180	122	59.69	7.2	12

Table 5.7: Slant-range velocity estimation results (SCR=$23dB$).

Target	$v_x[km/h]$	$\hat{v}_x[km/h]$	error
1	29.85	29.05	2.7%
2	59.69	61.24	2.6%

5.6 details the moving targets velocities and coordinates. The SCR is roughly set to 23 dB. Notice that the slant-range velocities of both targets induce Doppler-shifts corresponding to 6 and 12 times the maximum unambiguous value imposed by the PRF. The resulting data was focused using the wavefront reconstruction algorithm with static ground parameters. The obtained image is presented in Fig. 5.8, where the moving objects appear defocused and misplaced as expected.

Each moving object signature was digitally spotlighted in the spatial domain and resynthesized back to the (k_u, k) frequency domain as proposed in [54]. The resulting resynthesized signature in the (k_u, k) domain is presented in Fig. 5.9 for illustration purposes only.

The maximum magnitude of correlation (5.2.6) is shown in Fig. 5.10b). It varies linearly with the fast-time frequency as predicted, although exhibiting local correlation due to the interaction between the large number of scatterers that compose the BTR-60 vehicle. Nevertheless, the resulting velocity estimates are still very accurate (see Table 5.7).

As we did in the previous subsection, we used both estimates of μ and α to retrieve the full velocity vector. Table 5.8 shows the obtained results. The accuracy

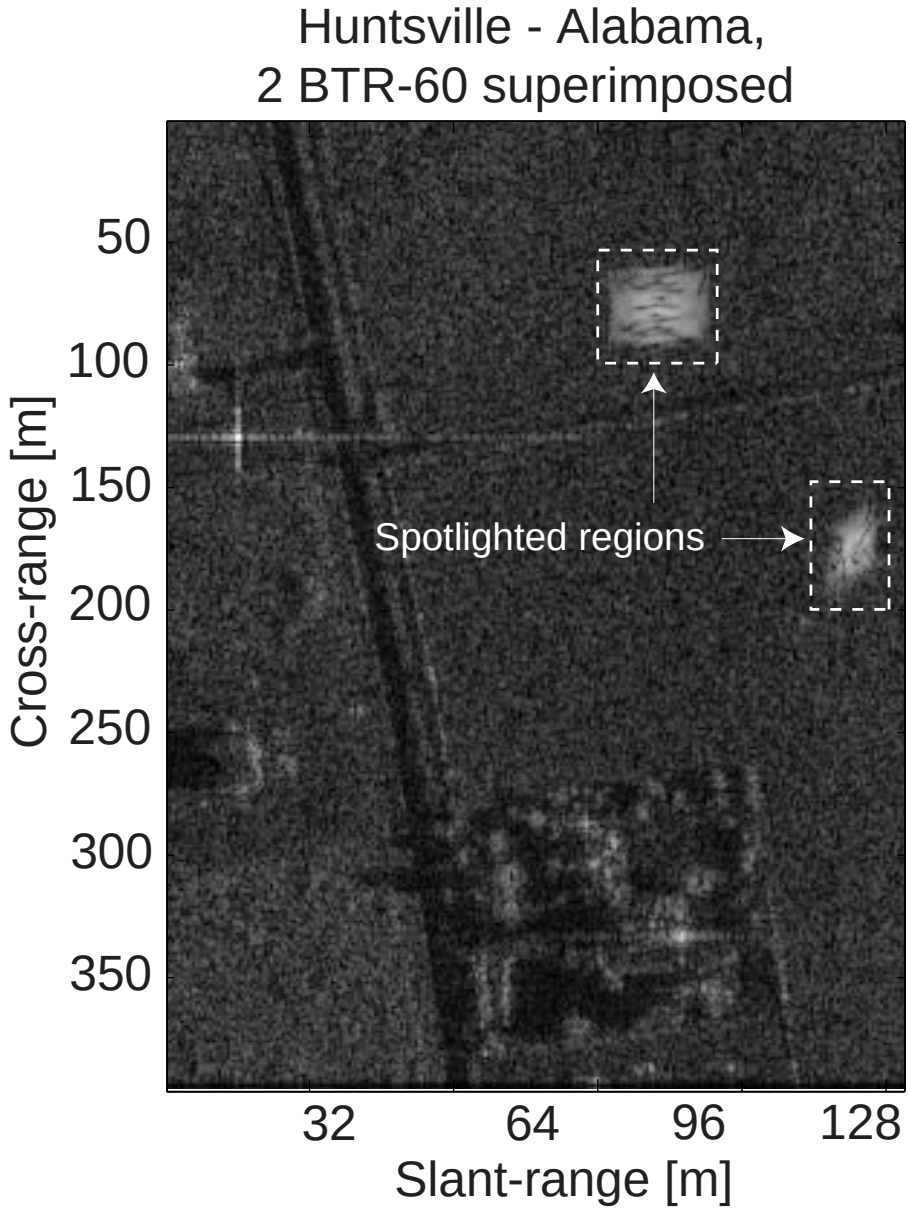

Figure 5.8: Scene from Hunstville - Alabama, where two moving BTR-60 transport vehicles are superimposed. The slant-range velocity of the vehicle on the left exceeds the Nyquist limit by 6 times, whereas the vehicle on the right exceeds that velocity by 12 times. They appear defocused and misplaced as expected.

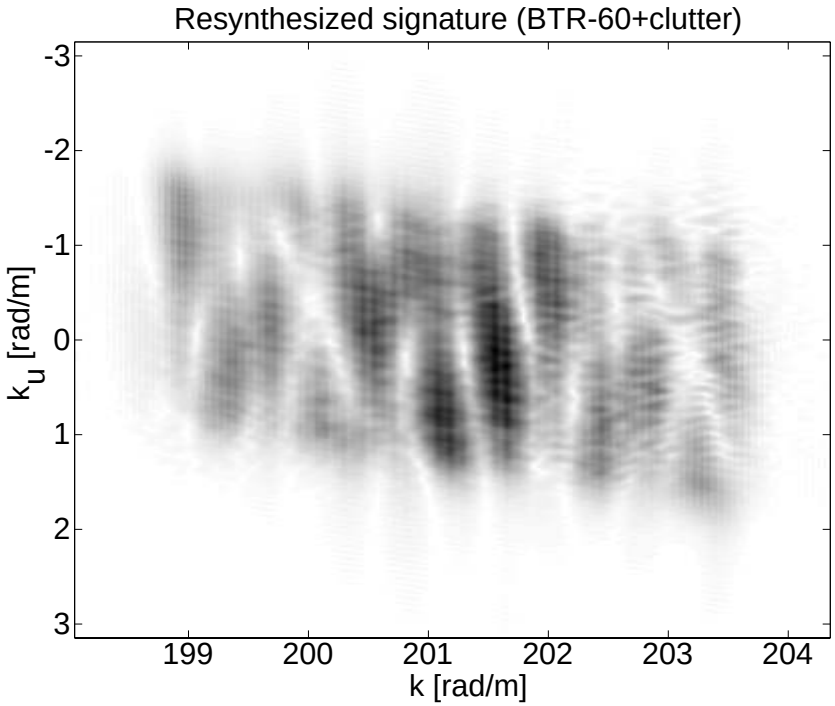

Figure 5.9: Resynthesized signature of the BTR-60 plus clutter.

Table 5.8: Complete velocity vector estimation (SCR=23dB).

Target	$(v_x, v_y)[km/h]$	$(\hat{v}_x, \hat{v}_y)[km/h]$
1	(29.85,36)	(29.05,38.91)
2	(59.69,7.2)	(61.24,8.21)

with respect to the estimation of the velocity vector norm is better than 4%.

5.3.3 Monte Carlo results

Figure 5.11 plots the standard deviation of μ obtained by Monte-Carlo (MC) estimation (64 runs) and the Cramer-Rao lower bound (CRLB) given by the right hand side of (C.1.14), versus the normalized cross-range velocity v_x/v_{max}. The digitally spotlighted region size is 5×5 [m], the number of independent samples is $M = 5$, and the SCR is 20 dB. The mission parameters are listed in Table 5.1.

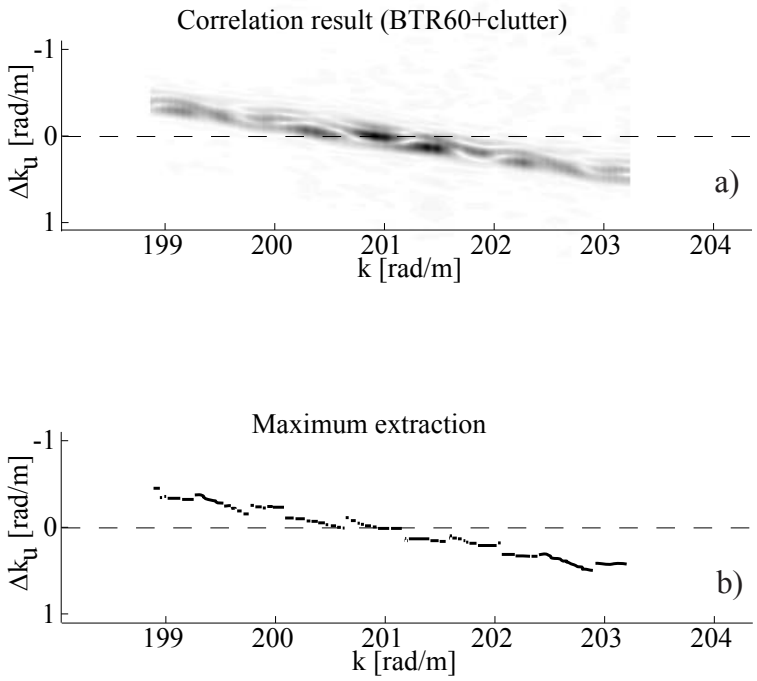

Figure 5.10: a) Result of the proposed correlation for the BTR-60 vehicle moving with slant-range velocity of 12 times the maximum imposed by the mission PRF; b) Ordinates where the maximum values of the previous correlation occur. The true slant-range velocity is retrieved with an error of 2.6%.

The CRLB exhibits a periodic type pattern due to the overlapping of the moving object spectrum on the clutter spectrum when v_x/v_{max} is even. When the ratio v_x/v_{max} is odd, the overlapping is minimum and we can expect better estimation results. As it can be seen, the presented strategy performs quite well, although it does not reach the CRLB. Notice that the MC results do not present the periodic shape of the CRLB curve. This is due to the fact that the proposed estimator, which is based on a correlation, does not include any information about the clutter statistics. If we had used the clutter covariance matrix in the derivation of the estimator, we should have had the periodic behaviour present on the CRLB curve and a smaller offset between the CRLB curve and the MC results. However, the estimator would be more complex and less robust, as it would depend on the antenna radiation pattern which, usually, is not precisely known.

Figure 5.12 plots MC results, for a fixed $v_x/v_{max} = 10$, as function of the SCR. The dashed curve considers a spotlight region with dimensions of $5 \times 5\,[\mathrm{m}]$ and the solid curve refers to a spotlight region with dimensions of $10 \times 10\,[\mathrm{m}]$. For SCR below 6dB, the estimator gives useless results, since the estimation errors are much larger than the Nyquist limit given by $\mu_{max} = v_{max}/V = \lambda_0 PRF/(4V) = 0.0083$. For SCR between 6dB and 25dB, the estimator accuracy increases with the SCR. If we define as minimum requirement that the standard deviation of μ must be smaller than the Nyquist limit, i.e., $\sigma_\mu < 0.0083$, then we can see that the estimator gives effective results for SCR$>$ 14dB for the dashed curve and SCR$>$ 20dB for the solid curve. For SCR above 25dB the estimator accuracy is almost constant and close to the CRLB.

Concerning the larger spotlight region, and for 6dB$\leq$SCR$\leq$25dB, we can read a degradation of approximately 6dB for the minimum requirement. This degradation

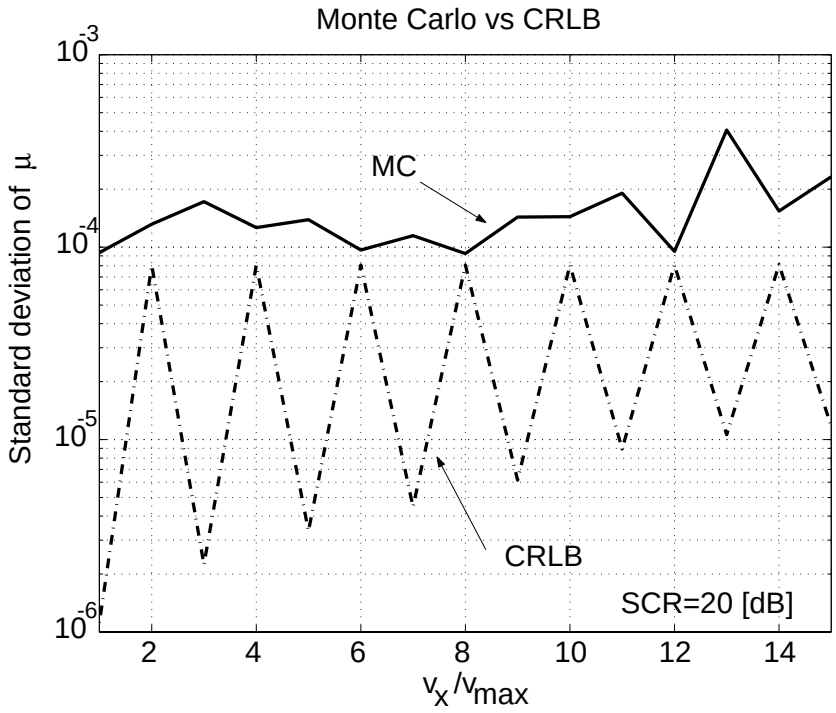

Figure 5.11: Monte Carlo results (64 runs) versus Cramer-Rao Bound.

was to expect, because the second digitally spotlighted region has 4 times the area of the first region and the estimator does not use any information about the clutter statistics. As a rule of thumb, for each quadrupling of the spotlight area, we can expect a degradation of, approximately, 6dB on the minimum SCR required.

5.3.4 Violation of assumptions

The proposed methodology to obtain the slant-range velocity of the moving targets relies on the following assumptions:

i) The reflectivity of moving targets are independent of the aspect angle;

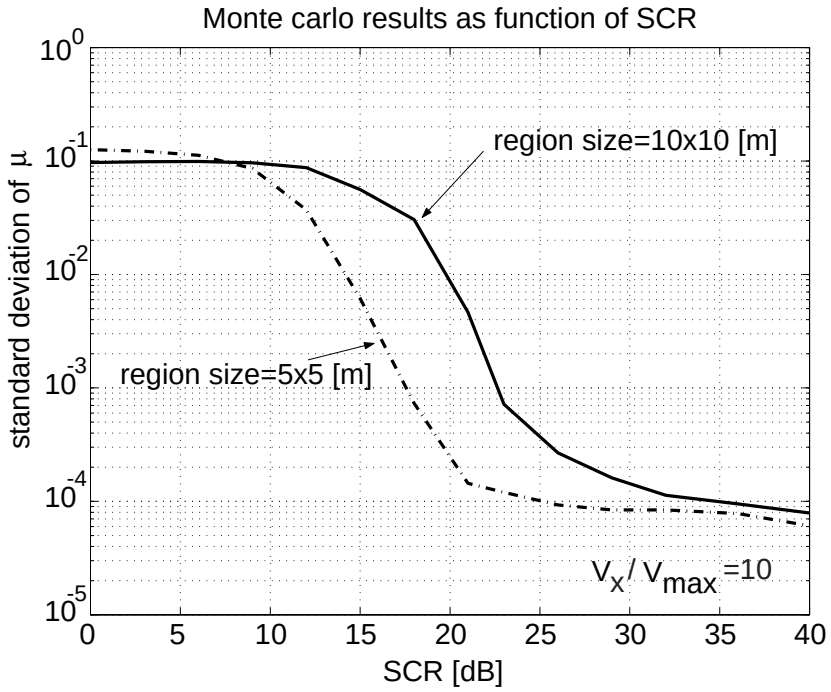

Figure 5.12: Monte Carlo results (64 runs) as function of the SCR.

ii) The moving targets are point-like or they contain predominant scatterers, thus exhibiting near point-like behaviour;

iii) The moving targets are separable from each other in the spatial domain;

iv) The clutter that remains after the digital spotlight operation exhibits small correlation in the frequency domain.

The first assumption greatly simplifies the problem formulation and yet leads to good results. The second assumption is reasonable, as most man-made targets can be considered to be a set of individual point-like scatterers [12]. In this subsection we will illustrate what happens when the assumptions iii) and iv) are violated. We start with the analysis of a scenario where two moving targets appear overlapped in the unfocused image. In this situation the digital spotlight operation cannot isolate one target from the other. The resynthesized signature of the spotlighted region can thus be written as

$$\hat{S}_m(k_u, k) = S_{m1}(k_u, k) + S_{m2}(k_u, k) + S_{0R}(k_u, k), \tag{5.3.2}$$

where S_{m1} and S_{m2} are the signatures of the two moving targets and S_{0R} is the remaining noise after the digital spotlight operation.

The correlation $R_{\hat{S}\hat{S}}$ between $\hat{S}_m(k_u, k_0)$ and $\hat{S}_m(k_u, k)$ is

$$\begin{aligned} R_{\hat{S}\hat{S}}(\Delta k_u, k_0, k) &= R_{S1S1}(\Delta k_u, k_0, k) + R_{S2S2}(\Delta k_u, k_0, k) \\ &+ R_{S1S2}(\Delta k_u, k_0, k) + R_{S2S1}(\Delta k_u, k_0, k) + R_0(\Delta k_u, k_0, k) \end{aligned} \tag{5.3.3}$$

where

$$\begin{aligned} R_0(\Delta k_u, k_0, k) &= R_{S1N}(\Delta k_u, k_0, k) + R_{S2N}(\Delta k_u, k_0, k) \\ &+ R_{NS1}(\Delta k_u, k_0, k) + R_{NS2}(\Delta k_u, k_0, k) + R_{NN}(\Delta k_u, k_0, k) \end{aligned} \tag{5.3.4}$$

Terms R_{S1S1} and R_{S2S2} denote the autocorrelation of each moving target signature. Terms R_{S1S2} and R_{S2S1} denote their crosscorrelations. Term R_0 contains the crosscorrelations between each moving target signature and the remaining clutter. Term R_{NN} is the autocorrelation of the remaining clutter.

As shown in (5.2.6), each R_{SiSi} originate maxima with slope depending on the respective moving target relative slant-range velocity. Terms contained in R_0 are expected to have negligible values, when compared with the autocorrelation of each of the moving targets. We will now focus on the remaining two terms corresponding to the crosscorrelations between the moving targets. Following a procedure similar to that used to derive (5.2.6), we obtain

$$R_{SiSj}(\Delta k_u, k_1, k_1 + \Delta k) \propto \int_{-\infty}^{+\infty} A_i(k_u, k_1) A_j^*(k_u - 2\Delta k \mu_j - \Delta k_u, k_1) e^{j\phi_j} dk_u, \tag{5.3.5}$$

where $i, j = 1, 2\,(i \neq j)$ indexes terms corresponding to the respective moving target, and

$$\phi_j \approx \frac{2k_u \Delta k_u}{4(k_1 + \Delta k)\alpha_j^2} X_j + \frac{k_u^2}{4k_1}\left(\frac{X_i}{\alpha_i^2} - \frac{X_j}{\alpha_j^2}\right) + k_u\left(\frac{Y_i}{\alpha_i} - \frac{Y_j}{\alpha_j}\right). \tag{5.3.6}$$

When compared with (5.2.7), phase ϕ_j depends also on the differences between the moving targets motion transformed coordinates. The most important term of (5.3.6) is $k_u(Y_i/\alpha_i - Y_j/\alpha_j) \approx k_u(Y_i - Y_j)$. Roughly, if $|Y_i - Y_j| > \pi/B_u$, we can expect (5.3.5) to have insignificant values when compared with the autocorrelation of each of the moving targets. For the mission parameters given in Table 5.1 this implies that differences larger than, approximately, 1[m], are sufficient to make the crosscorrelation terms negligible. Therefore, if the digitally spotlighted region contains two moving

targets with different velocities, it can be expected that the proposed correlation will produce two lines, resulting from the autocorrelation terms R_{S1S1} and R_{S2S2}, with slopes corresponding to each moving target slant-range velocity.

The previous analysis is now illustrated using simulated data. We start with a scenario containing two point-like moving targets with velocity vectors of targets 1 and 3 listed in Table 5.2. Their slant-range velocities are 10 times greater than v_{max}, but they travel in opposite directions. Both targets were simulated to appear overlapped in the unfocused image and the difference $|Y_i - Y_j|$ is 7[m]. One of the targets has reflectivity 3 dB greater than the other. In this case the digital spotlight operation cannot isolate one target from the other. Both signatures will thus be used simultaneously in the computation of the correlation (5.2.6). The correlation result is shown in Fig. 5.13, where two lines with different intensities and symmetric slopes are clearly distinguishable. Each line corresponds to one moving target. The intensities are distinct due to the different reflectivity of each moving target.

In the next example the assumption of small correlation for the clutter is violated. To accomplish this, we superimpose a moving target on a man-made structure after focusing the target area with static ground parameters. The considered man-made structure is positioned at coordinates (131,39) (see Fig. 5.8). The digital spotlight operation is not able to separate the two objects, and the signature of the static structure will be used in the correlation. Conceptually, this structure can be though of as a moving target with zero velocity. Therefore, we may expect an horizontal line due to it. The correlation result is presented in Fig. 5.14, where two lines with different slopes are clearly visible. As predicted, the horizontal line is due to the static man-made structure. The line with non-zero slope is originated by the moving

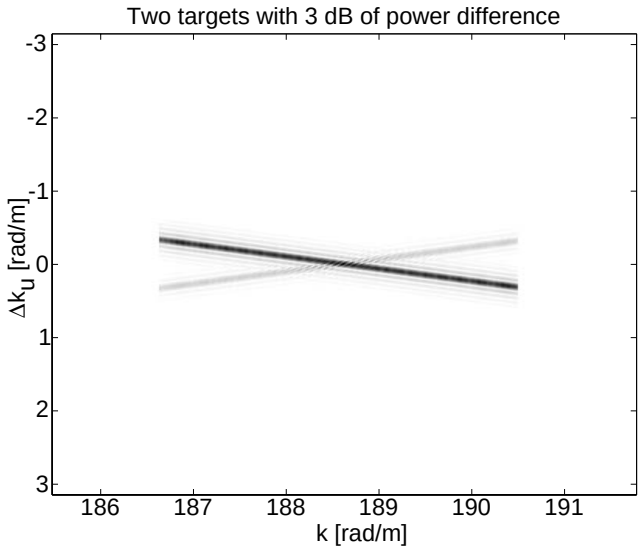

Figure 5.13: Result of the proposed correlation in a scenario where two moving objects with different reflectivities and opposite slant-range speeds are present. As expected, the result are two lines with distinct intensities and symmetric slopes.

target.

From the previous examples we see that we cannot simply apply the last step of the proposed algorithm, which consists on a linear regression on the correlation maxima. A more sophisticated scheme is thus necessary. We will address these scenarios in the near future.

5.4 Conclusions

This paper presents a novel methodology to retrieve unaliased estimates of the slant-range velocity of moving targets inducing Doppler-shifts beyond the Nyquist limit

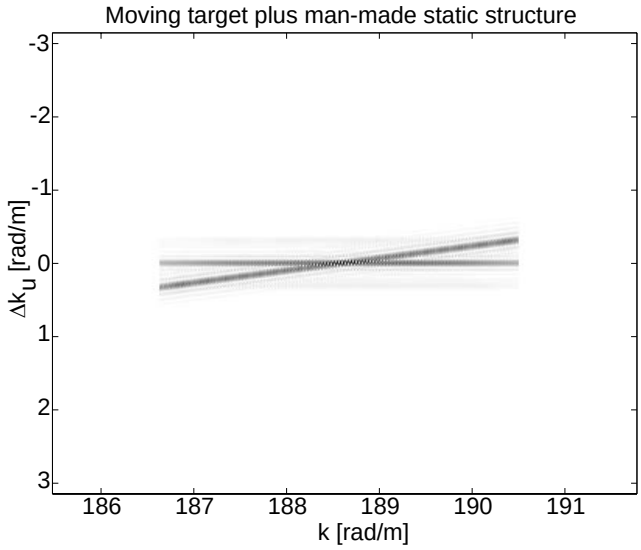

Figure 5.14: Result of the proposed correlation in a scenario where the digital spotlight operation is not able to separate the moving object from a man made static structure. The resulting horizontal line is due to the static structure. The off-horizontal line is due to the moving object.

imposed by the mission PRF. The methodology exploits the linear dependency of the Doppler-shift with the slant-range velocity for each fast-time frequency. That is, the echo from a moving object, in the two-dimensional frequency domain, exhibits a skew not subject to PRF limitations. An estimator of the spectrum skew is proposed and its usefulness using real and synthetic data is illustrated. The accuracy is shown to depend on the transmitted pulse bandwidth. Basically, this is due to the fact that by using a larger bandwidth we have a larger number of independent samples to feed the estimator and, therefore, we have lower variance on the resulting velocity estimates. The method gives effective results even when the returned echoes of the moving targets and the static ground overlap completely, provided that the moving targets signatures are digitally spotlighted and the SCR is greater than 14dB.

By combining the methodology herein proposed with an existing algorithm to retrieve the velocity vector magnitude, the full velocity vector is estimated with high accuracy using aliased data from a single SAR sensor.

The major limitations of the proposed approach are the following assumptions:

i) The reflectivity of moving targets are independent of the aspect angle;

ii) The moving targets are point-like or they contain predominant scatterers, thus exhibiting near point-like behaviour;

iii) The moving targets are separable from each other in the spatial domain;

iv) The clutter that remains after the digital spotlight operation exhibits small correlation in the frequency domain.

The first assumption greatly simplifies the problem formulation and yet leads to good results. The second assumption is reasonable as most man-made targets can be considered to be a set of individual point-like scatterers [12]. We then consider

the problems that arise when the last two assumptions are violated. We derive theoretically the correlation structure when two moving targets are not separable in the spatial domain. In this scenario, the correlation will result in two maxima with slopes depending on each moving target relative slant-range velocity.

The last assumption was also theoretically addressed, in the situation where the digitally spotlighted region contains a moving target and a man-made structure. In this situation, the correlation shows two maxima, one of them occurring for $\mu = 0$ (an horizontal line). The horizontal line is due to the man-made structure and the off-horizontal line is due to the moving target. These theoretically derived results are confirmed by simulations.

Chapter 6

Conclusion

The main goal of this work was to develop novel methodologies to deal with moving targets using data recorded from a single SAR sensor. The solution to the problems herein addressed require, typically, two or more sensors. The reduction of the number of SAR sensors required to accomplish a predetermined goal is a very serious issue since it leads directly to the reduction of the mission costs and to proportionally smaller amounts of data to process. The main contributions of this thesis will now be summarized and suggestions of future research directions will be given.

6.1 Contributions

Chapter 1 presented some of the difficulties that arise when the goal is to process echoes from moving targets by using data recorded with a single sensor. One of the difficulties is the detection of the so-called endoclutter targets, that is, targets whose echoes overlap, in the slow-time frequency domain, those from the static ground. Another issue is the blind angle ambiguity. Put simply, this ambiguity refers to the fact that the value of the Doppler-shift alone is not sufficient to evaluate the azimuth

position of the target with respect to the fixed ground.

Chapter 2 derived the analytical expression for the antenna radiation pattern in the two-dimensional frequency domain. That expression showed that the echoed signal from a moving target is, in the slow-time frequency domain, a scaled and shifted version of the antenna radiation pattern in the spatial domain. Because each of the effects is due to an orthogonal component of the velocity vector this lead us to the conclusion that if one is able to estimate the scale and the shift, then the full velocity vector can be determined and the blind angle ambiguity can be solved using data from a single SAR sensor. We then computed the Fisher information matrix for the velocity parameters and concluded that the results could be, at least theoreticaly, accurate enough for most applications. Other conclusions that arose from the analysis of the Fisher information matrix where:

i) Higher range velocities lead to better estimates due to larger displacements between $A(k_u, \theta_0)$ and $A(k_u, \theta)$;

ii) The slant-range velocity estimation will be more accurate than the cross-range velocity estimation;

ii) The antenna radiation pattern should exhibit high derivatives at its band extremes.

Chapter 3 and Chapter 4 presented and evaluated two different methodologies that take advantage of the results made available in Chapter 2. The aim is to extract all the moving target kinematics parameters using data gathered by a single SAR sensor, therefore solving the blind angle ambiguity. Both of the strategies use the antenna radiation pattern knowledge. They differ however on the means adopted to tackle the problem. Each of the methodologies and their results will now be summarized.

The approach presented in Chapter 3 uses a step that compresses moving target

signatures along the slow-time Doppler domain for a given fast-time. Besides compressing moving targets signatures, that step yields, for each moving target candidate, the slant-range motion transformed estimate and an approximate estimate of the relative speed. A generalized likelihood ratio test approach was then adopted to detect moving targets and derive their trajectory parameters. Determining the maximum likelihood estimate necessary to compute the generalized likelihood ratio test would amount to a multidimensional nonlinear optimization of the unknown parameters, with unbearable computational burden. Instead of computing the exact maximum likelihood estimate, a suboptimal approach was adopted that iteratively maximizes the likelihood function on given subsets of the search space. The detection threshold was set according to the Neyman-Pearson criterion. Is was found that in the ideal case of perfect knowledge of density parameters (clairvoyant detector), the detector performance depends only on optimal signal to clutter plus noise ratio (SCNR_{opt}) obtained with the matched filter (filter matched to the signal signature immersed in clutter plus system noise).

The effectiveness of the proposed method was illustrated with synthetic and real data. In the former case, an S-band image with 8 point moving targets and an extended target with a predominant scatterer was simulated. For $\mathrm{SCR} = 20\,\mathrm{dB}$ and $\mathrm{CNR} = 20\,\mathrm{dB}$ the obtained estimates of the relative slant-range and cross-range velocities had an error of, approximately, 0.01% and of 0.4%, respectively. The initial position coordinates displayed errors less than the slant-range and cross-range resolutions. These values only degrade slightly for $\mathrm{SCR} = 14\,\mathrm{dB}$ and $\mathrm{CNR} = 20\,\mathrm{dB}$.

Real data results were obtained from X-Band images of the MSTAR public data collection collected by Sandia National Laboratory using STARLOS sensor. The

ground clutter and moving target signatures (transport vehicles BTR 60) were obtained by resynthesizing the respective reflectivities using an inverse wavefront reconstruction algorithm. The SCR of all moving targets, measured with respect to the strongest moving scatter was less than 20dB. With the exception of the initial cross-range position, all estimates were very accurate. The errors of the initial position x_0 and of the motion transformed coordinates X and Y were less than 1 m; the error of the slant-range velocity μ and of the cross-range velocity estimates were less than 0.4% and 1%, respectively. Concerning the initial cross-range positions, the obtained errors were smaller than 2 m for those targets exhibiting a clearly predominant scatterer. For two of the targets that was not the case, They had two predominant scatterers with similar reflectivity at the same cross-range motion transformed coordinate. For those targets the error on the initial cross-range position was larger, as expected.

Chapter 4 presented another approach to solve the blind angle ambiguity. The proposed strategy works in the spatial domain and instead of trying to straighten the moving target signature it collects the data along the signature curvature that is dependent of the moving target kinematics. To achieve efficiency and simplicity the ML estimator of the velocity parameters was derived by considering the clutter behaving as white noise. That assumption lead us to a matched filter solution. The suggested methodology was shown to permit the estimation of both the full velocity vector of a moving target and its initial coordinates. Using this information we were able to focus the moving objects and reposition them on their approximate true coordinates. This strategy was tested with targets inducing Doppler-shifts beyond the Nyquist limit imposed by the mission PRF. In all experiments the targets had

velocities ranging from 3 to 12 times the Nyquist limit. This limitation was overcome due to the fact that the velocity information is extracted in the 2D spatial domain instead of the Doppler-domain as is done by most techniques published in recent literature. A limitation inherent to the fact that the data was recorded by single SAR sensor was also readily apparent: although the proposed scheme enables the repositioning of the moving objects, in some situations their defocused versions cannot be removed from the original data. Such a case occurs when the moving objects spectra completely overlaps the clutter spectra.

The methodology was tested using a combination of simulated and real data. The simulated targets were of three distinct types: point-like, extended homogeneous and extended targets with a predominant target. Using the point-like target we started by carrying out Monte-Carlo simulations that showed that the methodology attains good estimation results for the velocity and repositioning, when SCR$\geq$ 10dB. In the case of SCR= 20dB the algorithm is able to solve the azimuth ambiguity with an error smaller than half the resolution in the cross-range. When the target is extended with homogeneous reflectivity, the results where not so good. This was already expected because the model used to develop the methodology corresponds to a point-like target. In this situation the relative slant-range velocity was estimated with accuracy of 3.7% and the relative cross-range velocity had an error of 2.2%. The repositioning had also a large error of 28.3m. However, when the moving target is extended but it exhibits a predominant scatterer, the results are completely different. The slant-range velocity was estimated with accuracy of 0.5% and the cross-range velocity was estimated with an error of 3.6%. The repositioning had an error of 1.6m which is accurate enough for many applications. The methodology was also tested

using real data from the MSTAR data set. In this situation, although the slant-range velocity was accurately estimated with an error of 0.03%, the cross-range velocity had a larger error of 2.2m/s. This larger error corresponds to 1.3% in the relative cross-range velocity estimate. The repositioning had an error of 5m. A degradation using the data from the MSTAR data set was already expected because none of the hypothesis taken when the methodology was developed is now verified: the clutter is not white noise and the target is not point-like.

To improve the estimation results one could perform more than one iteration of the algorithm, where the coordinate pair $(\hat{x}', \hat{y}')$ should be corrected using the results from the previous iteration. However, the computational efficiency now achieved, when compared with the methodology presented on Chapter 3, would be compromised.

Chapter 5 dealed with the problem of the estimation of the Doppler-shift induced by moving targets exhibiting slant-range velocities well beyond the Nyquist limit imposed by the mission PRF. The tackling of this problem is very important since it can provide the algorithms developed in the two previous chapters with a starting point, thus confining the search interval length only to a region of interest. The proposed methodology exploited the linear dependency of the Doppler-shift with the slant-range velocity for each fast-time frequency. Put simply, the echo from a moving object, in the two-dimensional frequency domain, exhibits a skew not subject to PRF limitations. An estimator of the spectrum skew was proposed and its usefulness was illustrated using a combination of real and synthetic data. The accuracy was shown to depend on the emitted pulse bandwidth. Basically, this is due to the fact that by using a larger bandwidth, more independent samples are available to feed the estimator and, therefore, the resulting velocity estimates show smaller variance.

The method was tested with synthetic and real data. The synthetic data set included six point-like targets and an extended target. The target velocities ranged from 2.5 to 10 times the maximum imposed by the mission PRF. All the slant-range velocities where estimated with accuracy ranging from 0.3% to 0.9%.

The methodology herein presented was also combined with a strategy proposed elsewhere to estimate the velocity vector magnitude. The purpose was to show that the full velocity vector could be estimated with little computational effort. The accuracy with respect to the velocity vector norm was better than 2%.

The tests with real data that included two BTR-60 vehicles with simulated motion over a scene from Huntsville-Alabama. The targets slant-range velocity exceeded 6 and 12 times the maximum imposed by the mission PRF. The velocity estimation was done with accuracy of 2.5%. The joint methodology previously proposed was able to estimate the complete velocity vector with accuracy of approximately 4%.

6.2 Future research directions

The methodologies presented in this thesis share some limitations that will now be mentioned. Suggestions to overcome them will be given.

All the techniques herein presented assume that the moving target reflectivity is independent of the aspect angle. Although this assumption does not correspond to the reality, it simplifies the problem formulation and yet leads to good results. This problem is of more concern in widebeam situations. In that scenario the reflectivity could be modeled as changing in the aperture domain. The model may also be used to perform target recognition since the amplitude changes in the slow-time domain is different for each type of target in the illuminated scene.

The moving targets were always considered as point-like targets or as containing few predominant scatterers. According to [10] and [12], this is reasonable as most man-made targets can be considered to be a set of individual point-like scatterers. When this is not the case, the extended targets could be modeled as arrays of discrete point targets, each one with a given reflectivity and distance to a reference point.

The moving targets were also considered as having constant velocity in the illumination interval. Although this can be considered true in most strip-map SAR scenarios, that is not the case in most of the ISAR configurations. In that case the targets often will be maneuvering. A different approach than the one that is presented in this thesis is thus necessary. A research direction include the study of the possibility to adapt the methodologies herein presented in such a way that they are able to accommodate trajectory variations. A promising approach includes the use of time-frequency transforms since they were developed for the purpose of characterizing the time-varying frequency content of a signal [10].

Concerning technique presented in Chapter 5, it relies on the assumption that the digitally spotligthed region contains a single moving target. When this assumption is not true it was shown that the proposed correlation produces more than a single line. Each of the lines has slope depending on each of the targets slant-range velocity. Therefore, the last step of the algorithm, consisting on a linear regression, cannot be simply applied. A more sophisticated scheme is thus necessary. The application of the Hough transform in the last step of the methodology will be investigated. This transform is used in a variety of related methods for shape detection. In particular, the Hough transform is able to provide information about the number of lines and their slope.

Appendix A

Slow-time Fourier transform of an AM-PM signal

A.1 Static targets

This appendix will compute the Fourier transform of

$$s(\omega, u) = a(x_n, y_n - u, \omega) e^{-j2k\sqrt{x_n^2 + (y_n - u)^2}} \tag{A.1.1}$$

with respect to the slow-time domain u.

The Fourier transform of (A.1.1) with respect u is, by definition,

$$S(\omega, k_u) = \int_u \underbrace{a(x_n, y_n - u, \omega)}_{\text{AM signal}} \underbrace{e^{-j2k\sqrt{x_n^2 + (y_n - u)^2}} e^{-jk_u u}}_{\text{PM signal}} du. \tag{A.1.2}$$

Admitting that the fluctuations of the AM component are slower than the PM component, the integral can be approximated to the integrand at the point where the instantaneous frequency of the PM signal is zero in the u domain (the phase center).

Let us find the phase center of

$$\psi = -2k\sqrt{x_n^2 + (y_n - u)^2} - k_u, \tag{A.1.3}$$

by computing $d\psi/du = 0$:

$$-\frac{2k(y_n - u)}{\sqrt{x_n^2 + (y_n - u)^2}} - k_u = 0 \Leftrightarrow k_u = \frac{2k(y_n - u)}{\sqrt{x_n^2 + (y_n - u)^2}}. \tag{A.1.4}$$

The next step consists in re-writing the phase in (A.1.4) without the dependency on u. From (A.1.4) we have

$$k_u^2 = \frac{4k^2(y_n - u)^2}{x_n^2 + (y_n - u)^2} \Leftrightarrow x_n^2 + (y_n - u)^2 = \frac{4k^2 x_n^2}{4k^2 - k_u^2} \tag{A.1.5}$$

From (A.1.4) one can also write

$$u = y_n - k_u \frac{\sqrt{x_n^2 + (y_n - u)^2}}{2k}. \tag{A.1.6}$$

Inserting (A.1.6) into (A.1.3), phase ψ becomes

$$\begin{aligned} \psi &= -2k\sqrt{x_n^2 + (y_n - u)^2} - k_u \left(y_n - \frac{k_u}{2k}\sqrt{x_n^2 + (y_n - u)^2} \right) \\ &= -\left(2k + \frac{k_u^2}{2k} \right) \sqrt{x_n^2 + (y_n - u)^2} - k_u y_n. \end{aligned} \tag{A.1.7}$$

Inserting (A.1.5) into the previous expression,

$$\psi = -\left(2k + \frac{k_u^2}{2k} \right) \sqrt{\frac{4k^2 x_n^2}{4k^2 - k_u^2}} - k_u y_n, \tag{A.1.8}$$

that is,

$$\psi = -\sqrt{4k^2 - k_u^2}\, x_n - k_u y_n. \tag{A.1.9}$$

The Fourier transform of (A.1.1), with respect to u is thus given by

$$S_u(\omega, k_u) = A \left(\frac{2k(y_n - u)}{\sqrt{x_n^2 + (y_n - u)^2}} \right) e^{-j\sqrt{4k^2 - k_u^2}\, x_n} e^{-jk_u y_n}. \tag{A.1.10}$$

Noting that

$$\frac{y_n - u}{\sqrt{x_n^2 + (y_n - u)^2}} = \sin\theta_n(u), \tag{A.1.11}$$

expression (A.1.10) can finally be written as

$$S_u(\omega, k_u) = A(2k\sin\theta_n(u))e^{-j\sqrt{4k^2 - k_u^2}x_n}e^{-jk_u y_n}. \tag{A.1.12}$$

A.2 Moving targets

In this section the Fourier transform of the signal

$$s_m(\omega, u) = a(y_0 - \nu u)P(\omega)e^{-j2k\sqrt{X^2 + (Y - \alpha u)^2}}, \tag{A.2.1}$$

with respect to u will be computed. Considering that $a(y_0 - \nu u)$ is a smooth function of u when compared with $\exp\{-j2k\sqrt{X^2 + (Y - \alpha)^2}\}$, the stationary phase method can be used. Under these circumstances we get

$$S(\omega, k_u) = A(\omega, k_u)P(\omega)e^{-j\psi(\omega, k_u)}, \tag{A.2.2}$$

where

$$A(\omega, k_u) \propto a(y_0 - \nu u), \tag{A.2.3}$$

$$\psi(\omega, k_u) = 2k\sqrt{X^2 + (Y - \alpha u)^2} + k_u u, \tag{A.2.4}$$

both (A.2.3) and (A.2.4) computed at $u = u(k_u)$ such that $\frac{d\psi}{du} = 0$, leading to

$$k_u = -2k\frac{d\psi}{du} = \frac{2k(Y - \alpha u)\alpha}{\sqrt{X^2 + (Y - \alpha u)^2}}. \tag{A.2.5}$$

By solving (A.2.5) with respect to u, as in the previous section, we get

$$\psi(\omega, k_u) = \sqrt{4k^2 - \left(\frac{k_u}{\alpha}\right)^2}X + \left(\frac{k_u}{\alpha}\right)Y, \tag{A.2.6}$$

Expression (A.2.2) can finally be written as

$$S(\omega, k_u) = A(k_u) e^{\sqrt{4k^2 - \left(\frac{k_u}{\alpha}\right)^2} X + \left(\frac{k_u}{\alpha}\right) Y}, \tag{A.2.7}$$

where k_u is given by (A.2.5); expression (A.2.7) is valid for $k_u/\alpha \in [-2k, 2k]$.

Appendix B

Clutter Statistics

B.1 Clutter statistics in the (k_u, t) domain

This section will compute the covariance of the clutter $\omega(k_u, t)$ for a fixed time t,

$$C_\omega(k_{u1}, k_{u2}) \equiv E[s_c(k_{u1}, t)s^*(k_{u2}, t)]$$

Let us recall that, according to (3.2.6) and(3.3.1), the static ground term w is

$$w(t, k_u) = \mathcal{F}^{-1}_{(\omega)} \left[S_0(k_u, \omega) P^*(\omega) e^{\psi'(k_u, \omega)} \right], \tag{B.1.1}$$

where phase $\psi'(\omega, k_u)$ is given by (A.2.6), i.e.,

$$\psi'(\omega, k_u) = \sqrt{4k^2 - \left(\frac{k_u}{\alpha}\right)^2} X + \frac{k_u}{\alpha} Y, \tag{B.1.2}$$

and

$$S_0(\omega, k_u) = P(\omega) A(k_u) \sum_n f_n e^{-j\psi_n(\omega, k_u)} \tag{B.1.3}$$

denotes the returns from all the scatterers that compose the static ground.

Inserting $S_0(k_u, \omega)$ into (B.1.1) yields

$$\begin{aligned} w(t, k_u) &= \\ &= \mathcal{F}^{-1}_{(\omega)} \left[|P(\omega)|^2 A_0(k_u) \sum_n f_n e^{-j\xi_n(k_u,\omega)} e^{-jk_u Y_n} \right], \end{aligned} \tag{B.1.4}$$

with

$$\xi_n(\omega, k_u) = 2k \left[\sqrt{1 - \left(\frac{k_u}{2k}\right)^2} X_n - \sqrt{1 - \left(\frac{k_u}{2\alpha' k}\right)^2} X' \right]. \tag{B.1.5}$$

Proceeding as in Appendix A, we conclude that

$$w(t, k_u) = A_0(k_u) \sum_n f_n R_p[t - t_n(k_u)] e^{-j\eta_n(k_u)},$$

where

$$t_n(k_u) \equiv \frac{2(X_n - X')}{c} + \frac{1}{c} \left(\frac{k_u}{2k_0}\right)^2 \left(X_n - \frac{X'}{\alpha'^2}\right) \tag{B.1.6}$$

$$\eta_n(k_u) \equiv -\frac{k_u^2}{4k_0} \left(X_n - \frac{X'}{\alpha'^2}\right) + k_u Y_n + \varphi. \tag{B.1.7}$$

1.5cm

Let us assume that the number of scatterers per resolution cell is large, none is predominant, the echo amplitudes f_n, $n = 0, 1, \cdots, N-1$ are mutually independent and have phase uniformly distributed in a 2π interval. Under these conditions $w(t, k_u)$ has complex Gaussian density [33], and the random complex amplitude f_n has mean value and variance

$$E[f_n] = E[|\rho_n|] \underbrace{E[e^{j\phi}]}_{=0} = 0 \tag{B.1.8}$$

$$E[f_n f_m^*] = \delta_{mn} \sigma_n^\circ, \tag{B.1.9}$$

where δ_{mn} is the Kronecker symbol, and σ_n° is the nth scatterer radar cross-section. These statistics implies that $E[w(t,k_u)] = 0$ and that the covariance $C_w(k_{u_1},k_{u_2}) \equiv E[t, w(k_{u_1})w^*(t,k_{u_2})]$ be given by

$$C_w(k_{u_1},k_{u_2}) = A_0(k_{u_1},k_{u_2}) \sum_n P\sigma_n^\circ R_n e^{-j[\eta_n(k_{u_1})-\eta_n(k_{u_2})]}, \tag{B.1.10}$$

where

$$A_0(k_{u_1},k_{u_2}) \equiv A_0(k_{u_1})A_0^*(k_{u_2}), \tag{B.1.11}$$

$$R_n \equiv R_p[t-t_n(k_{u_1})]R_p^*[t-t_n(k_{u_2})]. \tag{B.1.12}$$

According to expression (B.1.7) it follows that

$$\begin{aligned} \eta_n(k_{u_1}) - \eta_n(k_{u_2}) &= \\ &= X_n \underbrace{\frac{k_{u_2}^2 - k_{u_1}^2}{4k_0}}_{k_a} + Y_n \underbrace{(k_{u_1} - k_{u_2})}_{k_b} \\ &+ \underbrace{\frac{X'}{\alpha'^2}\frac{k_{u_1}^2 - k_{u_2}^2}{4k_0}}_{\xi} \qquad \text{(B.1.13)} \\ &= X_n k_a + Y_n k_b + \xi. \qquad \text{(B.1.14)} \end{aligned}$$

Thus,

$$C_w(k_{u_1},k_{u_2}) = A_0(k_{u_1},k_{u_2})e^{-j\xi} \times \sum_n \sigma_n^\circ R_n e^{-jk_aX_n} e^{-jk_bY_n}. \tag{B.1.15}$$

Function $R_p[t-t_n(k_u)]$ has its energy highly concentrated about $t_n(k_u) = t$, or, according to (B.1.6), about

$$X_n = X' \frac{ct + 2 + \left(\frac{k_u}{2\alpha' k_0}\right)^2}{2 + \left(\frac{k_u}{2k_0}\right)^2}.$$

Assuming that $|k_u/(2\alpha' k_0)|^2 \ll 1$, then $R(X_n, k_{u_1}, k_{u_2}) \equiv R_n$ has its energy clustered about $X_n = X' + (c/2)t$.

Having in mind that the backscattering coefficient $\sigma^\circ(X,Y)$ at (X,Y) is given by

$$\sigma^\circ(X,Y) \equiv \Delta^{-1} \sum_{\{n:(X_n,Y_n)\in\Delta(X,Y)\}} \sigma_n^\circ,$$

where $\Delta(X,Y)$ is a small rectangle of area Δ centered at (X,Y), then expression (B.1.15) can be approximated by the integral

$$\begin{aligned} C_w(k_{u_1}, k_{u_2}) = & \\ & A(k_{u_1}, k_{u_2}, \theta_0) e^{-j\xi} \int_{-\infty}^{\infty} \int_{Y_1}^{Y_2} R(X, k_{u_1}, k_{u_2}) \\ & \times \sigma^\circ(X,Y) e^{-jk_a X} e^{-jk_b Y} dX\, dY \end{aligned} \tag{B.1.16}$$

The high resolution of $R(X, k_{u_1}, k_{u_2})$, with respect to X, allows writing

$$\begin{aligned} C_w(k_{u_1}, k_{u_2}) &= A_0(k_{u_1}, k_{u_2}) e^{-j\xi} \\ &\times \underbrace{\int_{-\infty}^{\infty} R(X, k_{u_1}, k_{u_2}) e^{-jk_a X}\, dX}_{S(k_{u_1}, k_{u_2})} \underbrace{\int_{Y_1}^{Y_2} \sigma^\circ(X'', Y) e^{-jk_b Y} dY}_{\sigma^\circ(X'', k_b)}, \end{aligned}$$

with $X'' \equiv X' + (c/2)t$.

Function $S(k_{u_1}, k_{u_2})$ is the Fourier transform of $R(X, k_{u_1}, k_{u_2})$ with respect to X computed at $k_a = (k_{u_2}^2 - k_{u_1}^2)/(4k_0)$ and $\sigma^\circ(X, k_b)$ is the Fourier transform of of $\sigma^\circ(X,Y) I_{[Y_1,Y_2]}(Y)$ with respect to Y, where $I_{[Y_1,Y_2]}(Y)$ is the indicator function of set $[Y_1, Y_2]$.

Assuming that $\sigma^\circ(X,Y)$ is constant with respect to $Y \in [Y_1, Y_2]$, i.e., $\sigma^\circ(X,Y) = \sigma^\circ(X)$ for $Y \in [Y_1, Y_2]$, then $\sigma^\circ(X'', k_b) = e^{-k_b \overline{Y}} L \sigma^\circ(X'')\, \mathrm{Sa}\,(k_b L/2)$, with $\overline{Y} = (Y_1 + Y_2)/2$, $L = Y_2 - Y_1$, and $\mathrm{Sa}\,(x) \equiv \sin(x)/x$. Moreover, if $k_b = k_{u_2} - k_{u_1} = 2l\pi/L$, with

$l \in \mathcal{Z}$, then

$$C_w(k_{u_1}, k_{u_2}) = \sigma^\circ L E_{R_p} |A_0(k_u)|^2 \delta_l \tag{B.1.17}$$

where $\sigma^\circ \equiv \sigma^\circ(X)$, $E_{R_p} \equiv S(k_u, k_u)$ denotes the energy of $|R_p[cX/2]|^2$, and δ_l denotes the unitary impulse.

If $\sigma^\circ(X, Y)$ is not constant with respect to Y, then function $\sigma^\circ(X, k_{u_1} - k_{u_2})$ becomes more broaden. However, since $|k_a| \ll 1$, it is still reasonable to assume in most situations that $S(k_{u_1}, k_{u_2})$ is much more smooth than $\sigma^\circ(X, k_{u_1} - k_{u_2})$. In this case we have

$$C_w(k_{u_1}, k_{u_2}) = e^{-j\xi} E_{R_p} A_0(k_{u_1}, k_{u_2}) \sigma^\circ(X'', k_{u_2} - k_{u_1}). \tag{B.1.18}$$

B.2 Clutter statistics in the (k, ω) domain

In this section we show that the covariance of the echoes returned from the static ground in the slow-time and fast-time frequency domains decays very quickly, if we consider the clutter to be homogeneous with a large number of scatterers per resolution cell.

The returned echo from the static ground can be written as [55], [16], [45]

$$S(k_u, k) = |P(\omega)|^2 A(k_u, \theta_0) \sum_n f_n e^{-j\xi_n(k_u, k)}, \tag{B.2.1}$$

where f_n is the reflectivity of the nth static scatterer with coordinates (x_n, y_n), symbol $\theta_0 \equiv (\mu_0, \nu_0) = (0, 1)$, and

$$\xi_n(k_u, k) \equiv \sqrt{4k^2 - k_u^2}\, x_n + k_u y_n. \tag{B.2.2}$$

The covariance of S, $C_S(k_{u_1}, k_{u_2}, k_1, k_2) \equiv E\left[S(k_{u_1}, k_1)S^*(k_{u_2}, k_2)\right]$, is therefore

$$\begin{aligned} C_S(k_{u_1}, k_{u_2}, k_1, k_2) = & \\ = & \; E\left[|P(\omega_1)|^2|P(\omega_2)|^2 A(k_{u_1}, \theta_0)A^*(k_{u_2}, \theta_0)\right. \\ \times & \; \left.\sum_n f_n e^{-j\xi_n(k_{u_1}, k_1)} \sum_m f_m^* e^{j\xi_m(k_{u_2}, k_2)}\right]. \end{aligned} \tag{B.2.3}$$

If the scatterers are mutually independent, and each one has a phase independent of its amplitude and uniformly distributed in a 2π, interval , then $E[f_n f_m^*] = 0$ if $n \neq m$, and $E[f_n f_m^*] \equiv \sigma_n$ if $n = m$. The covariance is therefore written as

$$\begin{aligned} C_S(k_{u_1}, k_{u_2}, k_1, k_2) = & \\ = & \; \underbrace{|P(\omega_1)^2||P(\omega_2)^2|A(k_{u_1}, \theta_0)A^*(k_{u_2}, \theta_0)}_{\Gamma(k_{u_1}, k_{u_2}, k_1, k_2)} \\ \times & \; \sum_n \sigma_n e^{-j\left[\xi_n(k_{u_1}, k_1) - \xi_n(k_{u_2}, k_2)\right].} \end{aligned} \tag{B.2.4}$$

Using the approximation $\sqrt{4k^2 - k_u^2} \approx 2k - \frac{k_u^2}{4k}$, valid for $k \gg k_u$, we get

$$\begin{aligned} C_S(k_{u_1}, k_{u_2}, k_1, k_2) \approx & \; \Gamma(k_{u_1}, k_{u_2}, k_1, k_2) \\ \times & \sum_n \sigma_n e^{-2j(k_1 - k_2 - \frac{k_{u_1}^2}{8k_1} + \frac{k_{u_2}^2}{8k_2})x_n} e^{-j(k_{u_1} - k_{u_2})y_n}. \end{aligned} \tag{B.2.5}$$

Let us consider an homogeneous scene with constant backscattering coefficient given by

$$\sigma_0 = \frac{1}{\Delta} \sum_{n:(x_n, x_n)\epsilon\Delta(x', y')} \sigma_n, \tag{B.2.6}$$

where $\Delta(x', y')$ is a small rectangle of area Δ centered at (x', y'). Expression (B.2.5) can thus be approximated by

$$\begin{aligned} C_S(k_{u_1}, k_{u_2}, k_1, k_2) \approx & \; \Gamma(k_1, k_2, k_{u_1}, k_{u_2})\sigma_0 \\ \times & \int_{-L_x/2}^{L_x/2} \int_{-L_y/2}^{L_y/2} e^{-j2(k_1 - \frac{k_{u_1}^2}{8k_1} - k_2 + \frac{k_{u_2}^2}{8k_2})x} e^{j(k_{u_1} - k_{u_2})y} dxdy, \end{aligned} \tag{B.2.7}$$

where L_x and L_y are the target area lengths in slant-range and cross-range directions, respectively. After some algebraic transformation we are lead to

$$\begin{aligned} C_S(k_{u_1}, k_{u_2}, k_1, k_2) \approx \Gamma(k_{u_1}, k_{u_2}, k_1, k_2)\sigma_0 L_x L_y \\ \times \quad \text{sinc}\left[\frac{k_{u_1} - k_{u_2}}{2\pi} L_y\right] \\ \times \quad \text{sinc}\left[\frac{\left((k_1 - \frac{k_{u_1}^2}{8k_1}) - (k_2 - \frac{k_{u_2}^2}{8k_2})\right)}{\pi} L_x\right]. \end{aligned} \tag{B.2.8}$$

Larger values of L_x and L_y lead to more localized main-lobes of the sinc functions. In the slow-time frequency axis the covariance C_s is null for

$$|k_{u_1} - k_{u_2}| = \frac{2\pi}{L_y}, \tag{B.2.9}$$

and in the fast-time frequency axis the covariance is zero for

$$|k_1 - k_2| = \frac{\pi}{L_x}. \tag{B.2.10}$$

Under the large number of scatterers per resolution cell assumption, $S(k_u, k)$ is Gaussian (see Appendix II). Therefore, samples of $S(k_u, k)$ are independent if they are taken with spacing given by (B.2.9) and (B.2.10).

Appendix C

C.1 Cramer-Rao lower bound of the velocity components

In this section we compute the Cramer-Rao lower bound (CRLB) for the velocity components of moving targets.

As we saw previously, the returned echo from the static ground after pulse compression is

$$S_0(k_u, \omega) = |P(\omega)|^2 A(k_u, \theta_0) \sum_n f_n e^{-\xi_n(k_u, \omega)}, \tag{C.1.1}$$

where

$$\xi_n(k_u, \omega) = \sqrt{4k^2 - k_u^2} x_n + k_u y_n, \tag{C.1.2}$$

and $\theta_0 = (\mu_0, \nu_0) = (0, 1)$ denotes the velocity vector parameters for the static ground. For a point-like moving target with motion transformed coordinates (X, Y) and complex reflectivity f_m, the echoed signal is [55], [16]

$$S_m(k_u, \omega) = |P(\omega)|^2 A(k_u, \theta) f_m e^{-\xi_m(k_u, \omega, \alpha)}, \tag{C.1.3}$$

where $\alpha = \sqrt{\mu^2 + \nu^2}$ and $\theta = (\mu, \nu)$ and

$$\xi_m(k_u, \omega, \alpha) = \sqrt{4k^2 - (k_u/\alpha)^2}X + (k_u/\alpha)Y. \tag{C.1.4}$$

The total echo returned due to the static ground and the moving target is thus

$$S(k_u, \omega) = S_0(k_u, \omega) + S_m(k_u, \omega). \tag{C.1.5}$$

Let us define the vector

$$\mathbf{S} \equiv [S_{-N} \cdots S_0 \cdots S_N]^T, \tag{C.1.6}$$

for a fixed fast-time frequency ω_c, where, $S_i \equiv S(k_{u_i}, \omega_c)$, $k_{u_i} = \frac{i}{2N}\Delta K$ for $i = -N, \cdots, N$, and symbol ΔK denotes the spatial sampling frequency. In order to have independent samples, the sampling frequency ΔK is selected according to expression (B.2.10). Define also $\mathbf{A}(\theta) \equiv [A_{-N}(\theta) \cdots\ A_0(\theta) \cdots A_N(\theta)]^T$, where $A_i(\theta) \equiv A(k_{u_i}, \theta)$.

Let us assume that the number of static scatterers per resolution cell is large, none is predominant, the echo amplitudes f_n are mutually independent and each one has phase independent of its amplitude and uniformly distributed in a 2π interval. Then, the vector $\mathbf{S}$ is complex circular zero-mean and Gaussian [34]. The density of vector $\mathbf{S}$ conditioned to θ and the target reflectivity can thus be written as

$$p(\mathbf{S}|f_m, \theta) = \frac{1}{2\pi^N |\mathbf{C}_s|} e^{-(\mathbf{S}-\mathbf{m}_s)^H \mathbf{C}_s^{-1} (\mathbf{S}-\mathbf{m}_s)}, \tag{C.1.7}$$

where the mean $\mathbf{m}_s$ is given by

$$\mathbf{m}_s \equiv f_m |P(\omega_c)|^2 \mathbf{A}(\theta)\mathbf{Q}, \tag{C.1.8}$$

and $\mathbf{Q} \equiv \text{diag}[e^{-j\xi_m(k_{u_i}, \omega_c, \alpha)}, i = -N, ..., N]$.

As already shown in the previous appendix, the inverse of the covariance matrix $\mathbf{C}_s$ is given by

$$\mathbf{C}_s^{-1} = \frac{1}{|P(\omega_c)|^4 \sigma_0 L_x L_y} \text{diag}\left[|A(k_{ui}, \theta_0)|^{-2}, i = -N, ..., N\right]. \tag{C.1.9}$$

The elements of the Fisher information matrix for a circular complex Gaussian process are given by [34]

$$\begin{aligned}
[I(\theta)]_{ij} &= \text{tr}\left[\mathbf{C}_s^{-1}(\theta)\frac{\delta \mathbf{C}_s(\theta)}{\delta \theta_i}\mathbf{C}_s^{-1}(\theta)\frac{\delta \mathbf{C}_s(\theta)}{\delta \theta_j}\right] \\
&+ 2\text{Re}\left[\frac{\delta \mathbf{m}_s{}^H(\theta)}{\delta \theta_i} C_s^{-1}(\theta)\frac{\delta \mathbf{m}_s(\theta)}{\delta \theta_j}\right], \\
&\quad i, j = 1, 2.
\end{aligned} \tag{C.1.10}$$

The first term in equation (C.1.10) is null because the noise covariance matrix is independent of the moving target parameters. After some lengthy algebraic transformation we achieve the following expressions for the Fisher matrix elements:

$$\begin{aligned}
I_{11}(\theta) = \frac{2|f_m|^2}{\sigma_0 L_x L_y} &\left[\sum_i \frac{|A_i(\theta)|^2}{|A_i(\theta_0)|^2} k_{ui}^2 \mu^2 \right. \\
\times &\left. \left(\frac{k_{ui} X}{\alpha^2 \sqrt{4k^2 - (k_{ui}/\alpha)^2}} - \frac{Y}{\alpha^3}\right)^2 + \frac{k^2}{\nu^2} \sum_i \frac{|\dot{A}_i(\theta)|^2}{|A_i(\theta_0)|^2}\right]
\end{aligned} \tag{C.1.11}$$

$$\begin{aligned}
I_{12}(\theta) &= I_{21}(\theta) = \frac{|f_m|^2}{\sigma_0 L_x L_y} \left[2\mu\nu \sum_i \frac{|A_i(\theta)|^2}{|A_i(\theta_0)|^2} k_{ui}^2 \right. \\
&\times \left. \left(\frac{k_{ui} X}{\alpha^2 \sqrt{4k^2 - (k_{ui}/\alpha)^2}} - \frac{Y}{\alpha^3}\right)^2 \right. \\
&+ \left. \frac{k}{\nu^3} \sum_i (k_{ui} - 2k\mu) \frac{|\dot{A}_i(\theta)|^2}{|A_i(\theta_0)|^2}\right]
\end{aligned} \tag{C.1.12}$$

$$
\begin{aligned}
I_{22}(\theta) &= \frac{|f_m|^2}{2\sigma_0 L_x L_y}\left[4\nu^2\sum_i \frac{|A_i(\theta)|^2}{|A_i(\theta_0)|^2}k_{ui}^2\right. \\
&\times \left(\frac{k_{ui}X}{\alpha^2\sqrt{4k^2-(k_{ui}/\alpha)^2}}-\frac{Y}{\alpha^3}\right)^2 \\
&+ \left.\frac{(k_{ui}-2k\mu)^2}{\nu^4}\sum_i (k_{ui}-2k\mu)\frac{|\dot{A}_i(\theta)|^2}{|A_i(\theta_0)|^2}\right].
\end{aligned}
\tag{C.1.13}
$$

The Cramer-Rao Bounds for μ and ν are given by the inverse of the Fisher Information matrix (principal diagonal elements), that is, $\mathrm{CRLB}(\mu) = [I^{-1}(\theta)]_{11}$ and $\mathrm{CRLB}(\nu) = [I^{-1}(\theta)]_{22}$.

The proposed estimator uses several measurements on the available pulse bandwidth. If we consider that the measurements are independent and the CRLB has small variation on the frequency interval $k \in]-\pi B/c + k_0, k_0 + \pi B/c]$, we have then

$$\sigma_\mu^2 \leq \frac{1}{M}[I^{-1}(\theta)]_{11}, \tag{C.1.14}$$

where M is the number of independent measurements taken in the available pulse bandwidth. On the other hand, the estimator proposed in this paper is based on the linear regression of the correlation maxima occurring at $k_{u_i} = 2\mu(k_i - k_0) + \varepsilon_i$, where ε_i is a random variable with variance, say, σ_ε^2. A simple but lengthy algebraic computation leads to the conclusion that,

$$\sigma_\mu^2 \approx \frac{3}{M}\frac{\sigma_\varepsilon^2}{K^2}, \tag{C.1.15}$$

with $K = 2\pi B/c$.

This result states that the accuracy of the slant-range velocity estimates increases by augmenting the number of independent observations and by enlarging the transmitted pulse bandwidth. In Section 5.3 of the main text we plot CRLB curves and

compare these with the results obtained via Monte Carlo simulations.

Bibliography

[1] J. H. G. Ender A. R. Brenner, *First experimental results achieved with the new very wideband sar system pamir*, Proc. of the 4th European Conference on Synthetic Aperture Radar, EUSAR 2002, 2002, pp. 81–86.

[2] R. Bambler, *A comparison of range-doppler and wave number domain SAR focusing algorithms*, IEEE Transactions on Geoscience and Remote Sensing **30** (1992), 706–713.

[3] R. Bamler and H. Runge, *Prf-ambiguity resolving by wavelength diversity*, IEEE Transactions on Geoscience and Remote Sensing **29** (1991), 997–1003.

[4] S. Barbarossa, *Detection and imaging of moving objects with synthetic aperture radar: Part1*, IEE Proceedings-F **139** (1992), no. 1, 79–88.

[5] ———, *Detection and imaging of moving objects with synthetic aperture radar: Part2*, IEE Proceedings-F **139** (1992), no. 1, 89–97.

[6] S. Barbarossa and A. Farina, *Space-time-frequency processing of synthetic aperture radar signals*, IEEE Transactions on Aerospace and Electronic Systems **30** (1994), 341–358.

[7] D. Blacknell, *Target detection in correlated sar clutter*, IEEE Proceedings on Radar, Sonar and Navigation **147** (2000), 9–16.

[8] L. E. Brennan and I. S. Reed, *Theory of adaptive radar*, IEEE Transactions on Aerospace and Electronic Systems **9** (1973), 237–252.

[9] C. Cafforio, C. Prati, and F. Rocca, *SAR data focusing using sysmic migration techniques*, IEEE Transactions on Aerospace and Electronic Systems **27** (1991), no. 2, 194–206.

[10] V. Chen and H. Lin, *Time-frequency transforms for radar imaging and signal analysis*, Artech House, 2002.

[11] V. C. Chen, *Joint time-frequency transform for radar range-doppler imaging*, IEEE Tansactions on Aerospace and Electronic Systems **34** (1998), 486–499.

[12] V. C. Chen and Hao Ling, *Joint time-frequency analysis for radar signal and image processing*, IEEE Signal Processing Magazine **16** (1999), 81–93.

[13] Victor C. Chen, *Detection of ground moving targets in clutter with rotational wigner-radon transforms*, Proc. of the EUSAR'02, 2002, pp. 229–232.

[14] Robert E. Collin, *Antennas and radiowave propagation*, McGraw Hill, 1987.

[15] Jr. David C. Munson and Robert L. Visentin, *A signal processing view of strip-mapping synthetic aperture radar*, IEEE Transactions on Acoustics, Speech, and Signal Processing **37** (1989), no. 12, 2131–2147.

[16] J. Dias and P. Marques, *Moving targets detection and trajectory parameters estimation using a single sar sensor*, IEEE Tansactions on Aerospace and Electronic Systems **(submitted)** (2002).

[17] F. R. Dickey and M. M. Santa, *Final report on anti-clutter techniques*, Technical report no. r65emh37, General Electric Co.

[18] O. et al. Eckart, *traffic monitoring using along track airborne interferometric sar systems*, Proc. of the 7th World Congress on Intelligent Transport Systems, 2000.

[19] J. Ender, *Subspace transformation techniques applied to multi-channel SAR/MTI*, Proceedings of the 1999 International Geoscience and Remote Sensing Symposium-IGARSS'99, 1999, pp. 38–40.

[20] J. H. G. Ender, *The airborne experimental multi-channel SAR-system AER-II*, Proceedings of the EUSAR'96, 1996, pp. 49–52.

[21] ———, *Spacebased sar/mti using multistatic satellite configurations*, Proc. of the 4th European Conference on Synthetic Aperture Radar, EUSAR 2002, 2002, pp. 337–340.

[22] Joachim H. G. Ender, *Detection and estimation of moving target signals by multi-channel sar*, Proc. of the 1st European Conference on Synthetic Aperture Radar, EUSAR'96, 1996, pp. 411–417.

[23] J. R. Fienup, *Detecting moving targets in sar imagery by focusing*, IEEE Tansactions on Aerospace and Electronic Systems **37** (2001), 794–809.

[24] A. Freeeman and A. Currie, *Synthetic aperture radar (sar) images of moving targets*, GEC Journal of Research **5** (1987), no. 2, 106–115.

[25] B. Friedlander and B. Porat, *Vsar: A high resolution radar system for detection of moving targets*, IEE Proc. Radar, Sonar and Navigation **144** (1997), 205–218.

[26] ———, *Vsar: A high resolution radar system for ocean imaging*, IEEE Transactions on Aerospace and Electronic Systems **34** (1998), 755–776.

[27] J. Gazdag and P. Sguazzero, *Migration of seismic data*, Proceedings of the IEEE **1** (1984), 23–48.

[28] P. Gough and D. Hawkins, *Imaging algorithms for a strip-map synthetic aperture sonar: Minimizing the effects of aperture errors and aperture undersampling*, IEEE Journal of Oceanic Engineering **22** (1997), no. 1, 27–39.

[29] S. Haykin, *Communication systems*, John Wiley & Sons, New York, 2001.

[30] Romeiser R. Hirsch, O., *Accurate measurement of ocean surface currents by airborne along-track interferometric sar*, Proc. of the 3rd European Conference on Synthetic Aperture Radar, May 2000, pp. 127–130.

[31] G. Dong J. Chong, M. Zhu, *Ship target segmentation of high-resolution sar images*, Proc. of the 4th European Conference on Synthetic Aperture Radar, EUSAR 2002, 2002, pp. 693–696.

[32] J. Schmid J. M. Hilberg, B. Bickert, *Flight test results of a multi-channel sar/mti real-time system*, Proc. of the 4th European Conference on Synthetic Aperture Radar, EUSAR 2002, 2002, pp. 209–212.

[33] C. Jakowatz, D. Wahl, P. Eichel, D. Ghiglia, and P. Thompson, *Spotlight-mode synthetic aperture radar: A signal processing approach*, Kluwer Academic Publishers, Boston, 1996.

[34] S. Kay, *Fundamentals of statistical signal processing. estimation theory*, Prentice-Hall, Englewood Cliffs, NJ, 1993.

[35] ———, *Fundamentals of statistical signal processing. Detection theory*, Prentice-Hall, Englewood Cliffs, NJ, 1998.

[36] M. Kirsht, *Detection and imaging of arbitrarily moving targets with single-channel SAR*, Proceedings of the RADAR 2002 (Edinburg, UK), Oct. 2002, pp. 280–285.

[37] Martin Kirsht, *Detection, velocity estimation and imaging of moving targets with single-channel sar*, Proc. of the EUSAR'98, 1998, pp. 587–590.

[38] R. Klemm, *Introduction to space-time adaptive processing*, IEE Electronics & Communication Engineering Journal **911** (1999), no. 1, 5–12.

[39] ———, *Principles of space-time adaptive processing*, IEE, 2002.

[40] H. Baeggli L. Brule, *Radarsat-2 program update*, Proc. of the 4th European Conference on Synthetic Aperture Radar, EUSAR 2002, 2002, pp. 25–28.

[41] J. A. Legg, A. G. Bolton, and D. A. Gray, *Sar moving target detection using non-uniform pri*, Proc. of the 1st European Conference on Synthetic Aperture Radar EUSAR'96, 1996, pp. 423–426.

[42] et al. L.M.H. Ulander, *Ramcar-98. carabas vhf-band sar. final report*, Tech. report.

[43] R. P. Wishner M. T. Fennell, *Battlefield awareness via synergistic sar and mti exploitation*, IEEE AES Magazine **13** (1998).

[44] et al. M. Zink, *The advanced sar system on envisat: Mission staturs*, Proc. of the 4th European Conference on Synthetic Aperture Radar, EUSAR 2002, 2002, p. 38.

[45] P. Marques and J. Dias, *Moving targets in synthetic aperture images: A bayesian approach*, Proc. of the International Conference on Image Processing, ICIP 2000, 2000.

[46] ———, *Optimal detection and imaging of moving objects with unknown velocity*, Proc. of the 3rd European Conference on Synthetic Aperture Radar, EUSAR 2000, 2000, pp. 561–564.

[47] ———, *Antenna radiation pattern design for moving targets velocity estimation on sar imagery*, Proc. of the 3 Conferncia de Telecomunicaes, CONFTELE 2001, 2001.

[48] Richard P. Perry, Robert C DiPietro, and Ronald L. Fante, *Sar detection and imaging of moving targets*, Proc. of the EUSAR'98, 1998, pp. 579–582.

[49] R. Bamler I. Cumming R. Raney, H. Runge and F. Wong, *Precision SAR processing using chirp scaling*, IEEE Transactions on Geoscience and Remote Sensing **32** (1994), no. 4, 786–799.

[50] A. W. Rihaczec, *Principles of high-resolution radar*, Artech House, 1996.

[51] F. Rocca, C. Cafforio, and C. Prati, *Synthetic aperture radar: a new application for wave equation techniques*, Geophysical Prospecting **39** (1989), 809–830.

[52] M. Soumekh, *A system model an inversion for synthetic aperture radar imaging*, IEEE Transactions Image Processing **1** (1992), no. 1, 64–76.

[53] Mehrdad Soumekh, *Fourier array imaging*, Prentice Hall, 1994.

[54] ———, *Reconnaissance with ultra wideband uhf synthetic aperture radar*, IEEE Signal Processing Magazine (1995), 21–40.

[55] ———, *Synthetic aperture radar signal processing with matlab algorithms*, WILEY-INTERSCIENCE, 1999.

[56] H. Stolt, *Migration by Fourier transform*, Geophysics **1** (1978), 23–48.

[57] V. Velten J. Mossing T. Ross, S. Worrell and M. Bryant, *Standard sar atr evaluation experiments using the mstar public release data set*, SPIE Proceedings: Algorithms for Synthetic Aperture Radar Imagery V, 1998, pp. 566–573.

[58] G. Wang, X. Xia, V. Chen, and R. Fiedler, *Detection, location and imaging of fast moving targets using multi-frequency antenna array sar (mf-sar)*, Proc. of the 3rd European Conference on Synthetic Aperture Radar, EUSAR 2000, 2000, pp. 557–560.

[59] Genyuan Wang and Xiang-Gen Xia, *Dual-speed sar imaging of moving targets*, Proc. of the IEEE Radar Conference, 1999, pp. 227–232.

[60] Genyuan Wang, Xiang-Gen Xia, Victor C. Chen, and Ralph L. Fiedler., *Detection, location and imaging of fast moving targets using multi-frequency antenna array sar (mf-sar)*, Proc. of the 3rd European Conference on Synthetic Aperture Radar, EUSAR 2000, 2000, pp. 557–560.

[61] J. Ward, *Space-time adaptive processing for airborne radar*, Technical report 1015, Lincoln Laboratory, MIT, Dec. 1994.

[62] Xiang-Gen Xia, *On estimation of multiple frequencies in undersampled complex valued waveforms*, IEEE Transactions on Signal Processing **47** (1999), 3417–3419.